ULTRAFAST STRUCTURE AND DYNAMICS OF IONIC LIQUIDS REVEALED BY TWO-DIMENSIONAL INFRARED SPECTROSCOPY

by

Zhe Ren

B.S. Chemistry, Beijing Normal University, 2010

Submitted to the Graduate Faculty of

the Kenneth P. Dietrich School of Arts and Sciences in partial fulfillment

of the requirements for the degree of

Doctor of Philosophy

University of Pittsburgh

2018

UNIVERSITY OF PITTSBURGH

THE KENNETH P. DIETRICH SCHOOL OF ARTS AND SCIENCES

This dissertation was presented

by

Zhe Ren

It was defended on

December 21, 2017

and approved by

Sean Garrett-Roe, Assistant Professor, Chemistry

David Waldeck, Professor, Chemistry

Rob Coalson, Professor, Chemistry

Hyung J. Kim, Professor, Department of Chemistry, Carnegie Mellon University

Dissertation Director: Sean Garrett-Roe, Assistant Professor, Chemistry

ULTRAFAST STRUCTURE AND DYNAMICS OF IONIC LIQUIDS REVEALED BY TWO-DIMENSIONAL INFRARED SPECTROSCOPY

Zhe Ren, PhD

University of Pittsburgh, 2018

Two-dimensional infrared spectroscopy (2D-IR) is a non-linear spectroscopy that is capable of resolving molecular dynamics with picosecond time resolution and molecular-level spatial resolution. 2D-IR has been successfully implemented in a myriad of solution systems to study the local solute and solvent dynamics. Ionic liquids are a unique type of liquid with each formula unit a pair of cation and anion. The structure grants it unique properties that are suitable for many potential applications, and the chemical structure can be modified to be "task-specific".

In this thesis, I describe our implementation of 2D-IR to understand different aspects of the solvation dynamics of ionic liquids, including solvent dynamics, ultrafast structures and dynamics of small solutes, and the dynamics of ionic liquids under confinement. A direct correlation between the microscopic solvent dynamics and the macroscopic viscosity has been observed, indicating the molecular origin of viscosity in ionic liquids is possibly the ion-cage lifetime. Some small inorganic salts form ion-pairs in the ionic liquids, and have a Gibbs free energy of $\sim$8 kJ/mol. Some uncharged small molecules can cluster in ionic liquids, like water clusters with thiocyanate anion. The detailed structural and reorientation dynamics of ionic liquid-surfactant complexes imply a random cluster picture, rather than previously-believed reverse micelle picture; the shape of the dynamic correlation function also indicates a non-isotropic local orientation distribution that could originate from the ion-exchange between anionic surfacants and ionic liquids.

Keywords: ionic liquids, thiocyanate, 2D-IR, solvation dynamics.

TABLE OF CONTENTS

LIST OF TABLES

LIST OF FIGURES

PREFACE

It has been a long journey for me, from accepting the generous offer issued by the University of Pittsburgh, to completing my dissertation. It is a long journey in both distance and time. Pursuing a doctorate degree in a different country that is thousands of miles from home, with a language that is not as familiar as my mother tongue, with no family members nearby, is almost an impossible mission for anyone to face alone. Fortunately for me, many people generously offered their help, so that I did not have to fight alone. It is unfortunate that I cannot write the full list here since there are so many names, but I do want to express my gratitude to those who helped me the most.

Firstly, I would like to thank my advisor, Prof. Sean Garrett-Roe. Under his guidance, I have developed a comprehensive understanding of both theoretical and practical aspects of non-linear spectroscopy, and elevated my logic reasoning and scientific thinking skills. Not only his knowledge, but also his exemplary patience, optimism, and scientific passion have greatly inspired me, and serve as models to emulate in my future life and work. In daily life, he also has given me valuable suggestions on specific decisions, my career and life.

Secondly, I would like to express my special thanks to all the members of Garrett-Roe research group. This is a group of talented people with team spirit and brilliant minds. Dr. Thomas Brinzer provided me insights on my research via fruitful discussions, and offered me great assistance with optics. Dr. Samrat Dutta often shared his thoughts with me on my research projects, which inspired many new ideas. Mr. Prasad Gunathilaka and Mr. Jordan Kelly conducted NMR experiments and sample preparations for the colloidal dispersion work, and their passion, patience and carefulness influenced me. Mr. Clinton

Johnson, Ms. Sunayana Mitra, Ms. Carli Kelsheimer and Mr. Kai Gronborg also kindly helped with my experiments, as well as with scientific writing.

Thirdly, there are many other people both in and out of the University to whom I would like to extend a special thanks. Prof. Rob Coalson taught my quantum chemistry course, and helped me to solve many theoretical and mathematical problems. When my colloidal dispersion project encountered difficulty, Dr. Joel Gillespie and Dr. Damodaran Achary at the University, Prof. Michael Bockstaller and Dr. Ilhem Hakem from Carneige Mellon University generously offered their time, knowledge and ideas.

Finally, I would thank my family and friends. Without their support, I would never have finished this journey. Whenever I felt discouraged in my progress, I could always contact my parents. Through the screen, though thousand miles apart, their cheerful words and smiling faces always made me feel home. Dr. Ali Sinan Saglam and Dr. Ran Chen are my close friends, and classmates at the same time. They helped me to come out of frustrations at different stages of this journey.

1.0 GENERAL INTRODUCTION TO 2D-IR AND IONIC LIQUIDS

Ionic liquids are a unique type of liquid that are different from molecular liquids. Though their microscopic dynamics may be different, the scientific methods that have been employed in molecular solvents could still be applied. Two-dimensional infrared spectroscopy (2D-IR) has proved to be a useful tool for understanding the ultrafast solvent and solute dynamics in a wide variety of systems, and is expected to be a promising technique when applied to ionic liquids.

1.1 TWO-DIMENSIONAL INFRARED SPECTROSCOPY

2D-IR spectroscopy is a third-order non-linear spectroscopy technique with sub-picosecond time resolution[1]. It involves successive interactions of a set of vibrational transitions with three infrared pulses separated by small time intervals. The first pulse excites the system to a "coherent state", which is a superposition of the ground vibrational state and first excited vibrational state. After time t_1, which will be Fourier transformed into the initial frequency of the 2D-IR spectrum, the second pulse comes in and brings the system to either ground vibrational state or first excited vibrational state, and is also called "population state". Before the third IR pulse, there is a population time (or waiting time) t_2 during which the system can reorganize. The final infrared pulse brings the system once again to a coherent state and generates the third-order signal.

When the dynamics of the chromophore are slower than the experimental time resolution, the 2D-IR spectra are mathematically a two-point frequency correlation map. It indicates, for an ensemble of chromophores, the average probability of finding a molecule vibrating at certain initial frequency in the beginning of the pulse sequence, and at certain final frequency at the end of the pulse sequence, separated by population time. 2D-IR has two major kinds of information, namely spectral diffusion and cross peaks. The former is the correlation loss within the same vibrational peak and is a direct measure of the microscopic dynamics. The latter shows the correlation between different vibrational peaks, which indicates the microscopic structures and conformations of the chromophore.

The unique combination of high temporal resolution and high spatial resolution makes 2D-IR a suitable technique for solvation dynamics. In 2D-IR, the timescale can be measured from hundreds of femtoseconds, which is determined by the duration of the laser pulse and the pure dephasing time, up to hundreds of picoseconds, depending on the vibrational relaxation lifetime of the chromophore. The fact that the 2D-IR chromphores are well-defined chemical groups provides a sub-molecular spatial resolution. The dynamics of solvent or solute molecules with their immediate environment are typically an important aspect of the solvation dynamics, such as hydrogen-bonding dynamics and ion-pair formation, but are difficult to measure with normal techniques. Here, the spatial resolution means that the chromophores of 2D-IR are well-defined chemical groups that are generally sensitive to the microscopic environment, rather than a specific length scale.

Previously, 2D-IR has been applied to different molecular solvent systems, and provided insights into the dynamics. The dynamics of bulk water and water under confinement have been studied by the 2D-IR. It can also measure the dynamics of ion-pairing and solvent-solute complexation processes. 2D-IR is a suitable tool to understand the solvent and solute dynamics of different solution systems, and can provide new insight into ionic liquids.

1.1.1 Physical interpretation of 2D-IR spectra

Qualitatively, the 2D-IR spectrum describes the correlation of initial vibrational frequencies and final frequencies of the chromophore. The shape of the spectrum determines the amount of correlation between the initial state and final state of the molecule. A detailed mathematical derivation of the physical meaning of 2D-IR spectra can be found in chapter 4.

The 2D-IR spectrum of a single vibrational mode has two lobes of opposite signs (Figure 1, C). There is a negative lobe (often labeled blue) located on the diagonal axis, which is correlated with stimulated emission and ground-state bleach (the $\nu = 0$ to 1 transition). The positive lobe (often labeled red) comes from excited state absorption (the $\nu = 1$ to 2 transition), and is shifted below the diagonal line. The shift originates from the fact that each vibrational mode is not harmonic, and the harmonicity decreases the energy difference between higher excited states.

The diagonal and antidiagonal width of each lobe are determined by the properties of the solution system. Different local environments can change the vibrational frequency of the probe molecules, and together they create a distribution of frequencies, which forms the diagonal width (inhomogeneous width). The motions that are much faster than the time required to observe the corresponding frequency splitting, such as librational motions, cause the antidiagonal width (homogeneous width).

The change in local environment of the probe molecules can change the shape of the 2D-IR spectra (Figure 1, B). When the local environment changes, the frequency of the vibrational mode changes, which causes the loss of frequency correlation and the change in shape of the spectra. For early waiting times, the surrounding environment has very little time to evolve, and the correlation between the initial and final frequencies is high. As a result, the spectra are elongated along the diagonal direction. Given more time, the local environment gradually evolves and loses the memory of its original configuration, which causes the spectra to have a rounder shape. Given sufficiently long time, the correlation completely vanishes, and the spectra become round and no longer elongate along the diagonal

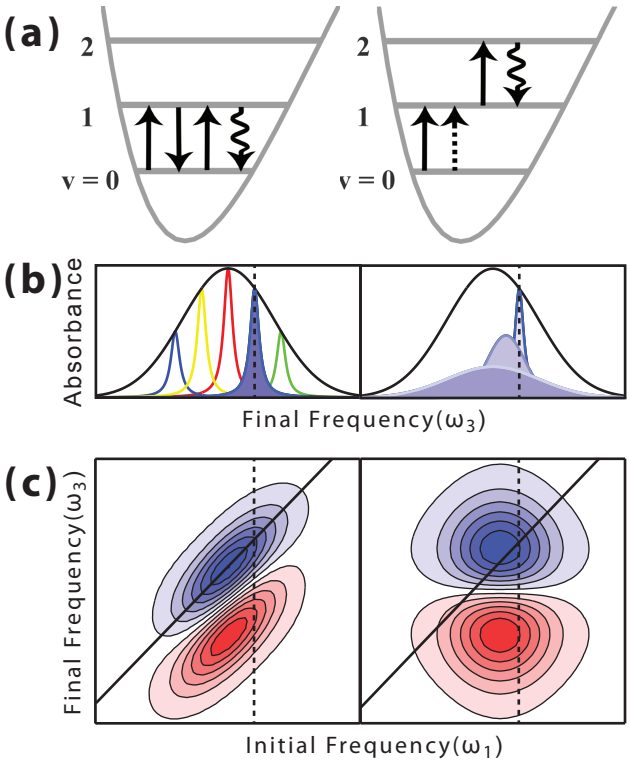

Figure 1: (a) Wave mixing diagram of ground state bleaching and stimulated emission (left), as well as excited state absorption (right). (b) Each subensemble of molecules generates a homogeneous linewidth, while the distribution of environments causes an inhomogeneous linewidth (left). As a molecule's environment reorganizes, its frequency randomizes, called spectral diffusion (right). (c) 2D-IR spectra record this spectral diffusion as a change in the shape (elongation) as a function of time. The spectra begin as stretched along the diagonal (left) and become round as an oscillator loses memory of its initial conditions (right).

axis. This process, which is called "spectral diffusion", can be quantified by the two-point frequency fluctuation correlation function (FFCF).

Another way to understand the physical origin of the shape change of the 2D-IR spectra is to consider the interference pattern generated by the pump pulses in the frequency domain[2,3]. The pump pulses, separated in time by a delay t_1, form a spectral frequency comb with a spacing $1/t_1$ (Figure 2). When incident on the sample, this frequency comb excites a spectral pattern of vibrational modes within the absorption line. The changes during the waiting time cause the spectral diffusion that gradually destroys the fringe pattern. After the waiting time, the probe pulse excites the system. The signal field that contains the final frequency distribution is then generated, and is measured by an array detector. Data is collected with different t_1 time points of the same waiting time, and Fourier transform is performed on the t_1 axis to generate the frequency correlation map.

1.1.2 2D-IR information content

2D-IR provides two major pieces of spectroscopic information, spectral diffusion and cross peaks. Spectral diffusion is the shape change of the 2D-IR peak as a function of time, which reflects the local dynamics of the system. The cross peaks are peaks located on the anti-diagonal of the 2D spectrum, and depending on the situation, they can give insights into the detailed structure of the molecule.

For a single 2D-IR peak, the shape change indicates the microscopic dynamics of the vibrational probe. The chromophores in the solvent can have different microscopic environments, and therefore have different vibrational frequencies. Molecules of different frequencies together form an ensemble of molecules that generate a two-dimensional Gaussian-shaped peak on the 2D-IR spectra. The tilt of the Gaussian peak along the diagonal axis indicates the degree of correlation between the initial and final state of the molecule after a certain population time. For early population times, the probed molecules have very little time to change, and the spectra are more elongated and tilted along the diagonal axis. Given more time, the molecules are more likely to change their environments and this correlation

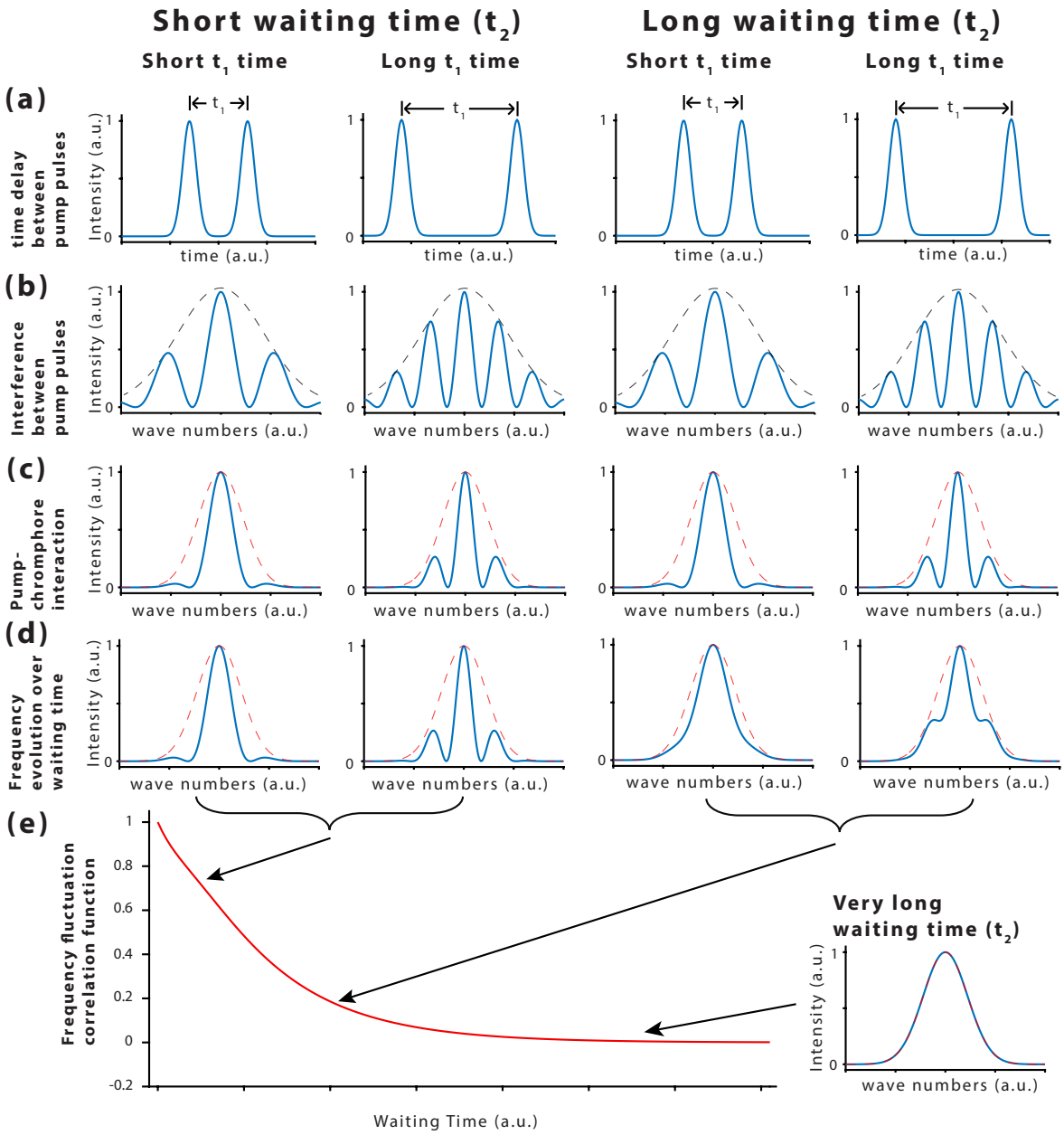

Figure 2: **(a)** The two pump pulses are separated by a time delay t_1. **(b)** Time delay makes the two pump pulses interfere with each other, and modify their frequency profile; the black dashed line indicates the original frequency profile. **(c)**The interference pattern when interacting with the sample, will only cause a subset of chromophores with correct frequencies to excite; the red dashed line represents the original lineshape of the peak. **(d)** Waiting time allows the excited molecules to change their frequencies, and gradually causes the frequency profile to evolve toward the original lineshape.

vanishes, which leads to a rounder shape of the spectrum. This process is called "spectral diffusion", and is directly correlated with the structural and reorientation dynamics of the chromophore. By quantifying with a frequency fluctuation correlation function (FFCF), the dynamic timescales can be resolved.

The cross peaks indicate the detailed structural information of the system. The cross peaks could occur between different chromophores, or between one chromophore of different configurations.

When two chromophores of slightly different frequencies are spatially close to each other, their vibrational modes could be coupled with each other. When coupled, during the waiting time, one vibrationally excited mode could transfer its excitation energy to the other mode to make it excited. On the 2D spectrum, this phenomenon will show up as a peak with initial frequency equal to one of the modes, and the final frequency equal to the other mode, and thus appears on the anti-diagonal direction of the spectrum. The energy transfer process can only happen when the two vibrational modes are sufficiently spatially close to each other, typically within a nanometer. Therefore, the appearance of energy transfer is useful to detect the clustering behavior of solutes in the solution[4–6], and has also been used to determine the spatial folding of proteins and residues[7–10].

The molecular configuration can greatly affect the frequency of the chromophore, and show up as multiple peaks of different frequencies. For example, the O-H stretch of phenol dissolved in benzene has two peaks, one from the free phenol and the other from a phenol-benzene complex[11]. During the experimental waiting time, if the configuration of the phenol molecule is changed from one to the other, a cross peak will form between the two peaks. In this case, the cross peak directly reports the conversion of molecules between different configurations in equilibrium, and the intensity of the cross peak as a function of time can indicate the rate of the conversion.

Resolving the ultrafast dynamics of ionic liquids from 2D-IR spectra is central to the research presented in the thesis (chapter 3, 4, 6). Once the dynamics are resolved, molecular simulations can be performed, and empirical laws can be established. For ion-pairs, the

existence of cross peaks between the ion-pair and free ion indicates the kinetic equilibrium of ion-pair dissociation process (chapter 5).

1.1.3 2D-IR chromophores

Typically, two parameters are crucial to determine the utility of a chromophore for 2D-IR experiments, the extinction coefficient and the vibrational lifetime. The extinction coefficient is a measure of the ability to absorb light, and is determined by the strength of the transition dipole. Given the same concentration, the vibrational modes of higher extinction coefficient yield more intense the 2D-IR spectra, since the signal intensity is proportional to the fourth power of the transition dipole moment. A chromophore with a higher extinction coefficient is very helpful when measuring in the low millimolar regime[12]. It is also of great help when measuring in a spectrally congested region, since the higher extinction coefficients can have better contrast in 2D-IR. For example, it is possible to resolve natural-abundance ^{13}CN peak in 2D-IR which consists only 1% of the total abundance of carbon atom[13]. The vibrational lifetime is the characteristic average time for the chromophore to stay in the same population state during the population time. The shorter the lifetime, the faster the 2D signal decays as a function of the population time. Since the solvation dynamics can be happening on vastly different timescales, a long-lifetime chromophore has more chance to fully resolve the dynamics of a system.

The infrared vibrational modes are abundant in most of the systems of study, and many of them can be directly used as the vibrational probe. This provides an opportunity to conduct "label-free" experiments where the chromophore is part of the experimental subject. Water, for example, has two vibrational modes that absorb strongly around 3500 cm^{-1}. This vibrational probe can be directly used when conducting experiments with the water being the research subject[14–16]. A good example is water under confinement[17–19], where water is the solute in the organic solvents.

Isotope-labelling is a widely used technique in the FTIR spectroscopy, and can be applied to 2D-IR as well[10,20–22]. The vibrational frequency is correlated with the reduced mass, and

by changing the atomic mass of the atoms, the frequency can be shifted. On the other hand, the chemical structure and dynamics are not affected by isotope labelling. This technique should be employed when the original region has strong background absorptions. One typical scenario is when measuring the bulk dynamics of solvents. In H_2O, for example, the O-H stretching modes near 3500 cm^{-1} have high absorption that will typically deplete the incident laser light, yielding no signal on the detector. To mitigate this problem, HOD can be doped in the H_2O as the chromophore, the O-D stretch is shifted to a spectroscopically isolated region at 2700 cm^{-1} [2,22]. In proteins, the amide I band is typically used to interrogate the dynamics of proteins in 2D-IR. To acquire residue-specific dynamics, the amide I band of the desired amino acid residue can be isotopically labelled by ^{13}C and ^{18}O [10,20,21,23].

There are many chemicals that do not intrinsically have an IR-active vibrational mode, or the mode is too weak to detect. Chemical modification is a potential solution to this problem. Strong vibrational chromophores such as SCN or CN can be chemically substituted onto the original compound, thus providing an IR-active probe on the chemical. Unnatural amino acids can be introduced to proteins for 2D-IR experiments to resolve site-specific information [10,24]. The imidazolium cation has been modified by SeCN to understand the cation dynamics in ionic liquids [25]. It is worth noting that the chemical modification can potentially change the properties of the compound, and the resolved dynamics may not perfectly resemble the dynamics of the original compound.

In most of my thesis works, thiocyanate has been employed as the vibrational probe. This chromophore absorbs in a spectrally-isolated region at $\sim$2050 cm^{-1}, and has a strong extinction coefficient of $\sim$830 $cm^{-1}M^{-1}$. The size of this anion is similar to the size of the ions in ionic liquids, and it therefore can provide local dynamics of the ionic liquid at a solvent molecule level (chapter 3). In fact, the thiocyanate ion is also widely used as the anion in ionic liquids, especially with the imidazolium-based cations. It provides an excellent contrast when studying the solute ion-pairing in ionic liquids (chapter 4). It is also used as the chromophore in label-free 2D-IR experiments of ionic liquids under confinement (chapter 6).

1.1.4 2D-IR measures the solute and solvent dynamics

2D-IR has been employed to study solvent and solute dynamics of molecular liquids. A similar approach can be applied to ionic liquids as well. 2D-IR is capable of capturing the hydrogen bonding dynamics in water, and thus we would expect it to reveal the hydrogen bonding dynamics in the ionic liquids with 2D-IR. The formation of cross peaks between the ion-pair and the free ion in 2D-IR provides a direct way to analyze the kinetics of ion-pair formation, which can be applied to study the ion-pair dynamics in ionic liquids as well. Ionic liquids can form colloidal dispersions in organic solvents, and are often referred as reverse micelles. Water-based reverse micelles have been well studied by 2D-IR, and can be used as a comparison to study the ionic liquid under confinement.

The bulk water dynamics have been well studied with 2D-IR. The hydroxyl stretch is an excellent IR chromophore and is sensitive to the number and strength of the molecular hydrogen bonds. A number of 2D-IR experiments have quantified the correlation decay of bulk water at various conditions. Ambient condition water has a characteristic exponential correlation loss at 50 fs[26,27], while the isotope slows the dynamics to 800 fs $\sim$ 1.4 ps in HOD / H_2O mixtures[28,29], and 900 fs $\sim$ 1.2 ps in HOD / D_2O mixtures[2,30,31]. There are also studies about the temperature-dependence of water dynamics[14], supercritical conditions[32], and supercooled conditions[15]. The frequency fluctuation correlation is highly dependent on the temperature. 3D-IR spectroscopy also found indications of inhomogeneity in the local water structure[33].

Since 2D-IR has helped illuminate the structure and dynamics of complex fluids such as water, it might be helpful to understand the dynamics of ionic liquids. The unique structure of an ionic liquid is expected to greatly affect the dynamics. The current understanding of molecular liquids can not be directly applied to ionic liquids. 2D-IR provides a technique to directly understand the bulk ultrafast structure and dynamics of the ionic liquids (chapter 3).

Due to its high-spatial resolution, and the sensitivity to the local structure and changes in dynamics, 2D-IR has been used to study solute structure and dynamics. The vibrational

frequency of the solute probe is sensitive to the change of micro-environments, and dynamic exchange between different species can be directly measured. The dynamics of solvent-solute complex formation of phenol dissolved in benzene has been observed by 2D-IR [11]. The dynamics of ion-pair formation is studied in aqueous solutions [4,34] and organic solutions [6,35–37], and the ion-exchange timescales between the ion-pair and free ion are measured in these systems. It is also possible to directly measure the acid-base equilibrium with 2D-IR [38].

There have been arguments about the existence of solvent ion-pairs [39] in ionic liquids, and computational experiments have shown that certain inorganic salts form ion-pairs in the ionic liquids [40]. It should be possible to use 2D-IR to capture the dynamics of these ion-pair species (chapter 4).

Water under confinement, specifically water-based reverse micelles, have been a difficult system to study due to its small size. Reverse micelles are water droplets dispersed in organic solvents with the aid of surfactants. They can be as small as a nanometer in diameter, containing only a couple thousands of water molecules. 2D-IR has been adopted to study the ultrafast structure and dynamics of the system. Water under confinement has much slower structural and reorientation dynamics than the bulk water dynamics, especially for the water molecules that are directly interacting with the surfactants (shell water). Further analysis found that the water dynamics within the reverse micelles are not highly dependent on the choice of solvents [17–19]. The follow up research found that the two sub-ensembles of water are weakly coupled, and the hydrogen-bonding network in the reverse micelles are more stable than the bulk [22]. Computer simulation has adopted to layerwise decompose the water dynamics in the reverse micelles [41].

The ionic liquids have been found to form microscopic structures with surfactants in organic solvents, and have shown interesting properties and potential applications. The high spatial resolution that has been demonstrated in the water-based reverse micelles can be adopted to the ionic liquid case (chapter 6).

1.2 IONIC LIQUIDS

Ionic liquids (ILs) are a special type of liquid in which each formula unit is a cation and anion pair. Room-temperature ILs should have a melting temperature below 100 °C[42]. They are also called room-temperature molten salts. The unique special structure offers different promising applications ranging from CO_2 capture[43–46] and chemical separations[47,48] to catalysis[49,50] and lubricants[51]. One major downfall to using ILs is that the physical and chemical behaviors of ILs significantly deviate from ideal fluid behavior, limiting the application of previous knowledge on molecular liquids[52]. To fully benefit from the potential of ILs, it is then critical to acquire in-depth microscopic understanding of these innovative fluids.

Different applications make use of different properties of ionic liquids, and therefore require understanding of different aspects. If the ionic liquid flows during an application, then a detailed understanding of the viscosity is required. If ionic liquids are used as reaction media, then an understanding of the microscopic solvation process of the solute is critical. Confinement could greatly change the dynamics of ionic liquids. In order to utilize an ionic liquid-surfactant nano-reactor, a detailed understanding of the microscopic structure of ionic liquids under confinement is important. The need for understanding each of these aspects of ionic liquids has motivated my work on the relation of hydrogen bonding to viscosity (chapter 3), solute ion-pair stability and dynamics (chapter 4 and 5), and ionic liquid-surfactant colloidal dispersions (chapter 6).

1.2.1 The microscopic origin of viscosity

Viscosity, in particular the dynamic viscosity, is a quantity that describes the resistance to internal deformation by sheer or tensile forces. In liquids, the viscosity is a result of different molecular interactions, including collisions, hydrogen bonding, van der Waals interactions and electrostatic forces. From the point of view of industrial applications, the viscosity is central to a great majority of processes and equippments, including mixing, separation, heat exchange and pipelines[53,54]. For most industrial processes, a lower viscosity is desired since

it reduces the cost for transferring and mixing the liquids.

The viscosity of ionic liquids are in general too high to be ideal for industrial applications[55]. Typical ionic liquids can have viscosity of ∼100 cP, some may even be as high as 1000 cP. Even for those low-viscosity ionic liquids, the viscosity is rarely below 20 cP, which is still more than 20 times higher than water[56]. This undesirable property is currently a major obstacle for successful applications of ionic liquids.

The viscosity of ionic liquids is sensitive to the chemical structures[57]. Changing the cation and the anion can greatly change the viscosity. For example, upon changing the counter-ion of 1-butyl-3-methylimidazolium from tetrafluoroborate to imide, the viscosity is reduced from 112 cP to 58 cP[58]. Therefore, synthesizing new ionic liquids is a viable way to lower the obstacle of viscosity. Recently, there have been reports on the synthesis of low-viscosity ionic liquids based on the tetramethylguanidinum cation[59] which can reduce the viscosity to ∼14 cP at room temperature; the tricyanomethanide-based ionic liquid also shows signs of low viscosity[60]. Theoretically, molecular dynamic simulations[61] and quantitative structure-activity relationship methods[62] have been employed in finding low-viscosity ionic liquid candidates.

Though progress has been made in finding lower viscosity ionic liquids, a systematic approach is greatly hindered by a lack of understanding about the microscopic origin of viscosity of the ionic liquids. The strong structure-viscosity correlation indicates that there is possibly a microscopic factor that is the origin of the macroscopic viscosity. If such microscopic origin of viscosity is on a molecular length scale, then 2D-IR could be a perfect tool to directly measure it. In chapter 3, we are going to use 2D-IR spectroscopy to study the molecular origin of viscosity of ionic liquids.

1.2.2 The solute dynamics of ionic liquids

Ionic liquids are a promising reaction medium. The unique structure grants a chemical environment for ionic liquids that cannot be found in molecular solvents. It has been found

that the ionic liquids can accelerate certain chemical reactions and maintain the biological activities of some proteins. Ionic liquids also have the advantage of being "green" solvent replacements for organic solvents. Ionic liquids have negligible vapor pressure, which means that they do not create air pollution[63]. Ordinary ionic liquids have low flammability, even at elevated temperatures[64]. For these reasons, ionic liquids are considered great candidates to replace the currently used organic solvents.

Ionic liquids have been used as reaction media in different realms of chemistry. One of the most promising directions is biomass processing, which deconstructs cellulose[65,66]. For organic synthesis, studies have found that the structure of ionic liquids could modify the reactivity of the nuclear substitution reactions, and in certain cases the reactivity can be significantly enhanced[67–69]. Some Bronsted acidic ionic liquids are found to be acidic catalysts that can accelerate reactions such as Aldol condensation[70], Pechmann reaction[71], oxidation reactions[72] and so on. Basic task-specific ionic liquids are also found useful in catalyzing a variety of reactions including Michael addition[73], Markovnikov addition[74] and so on. Many proteins have been found soluble in ionic liquids[75–77]. Some of the enzymes can retain the biological activity in ionic liquids or aqueous mixtures of ionic liquids[78,79]. Recently, surfactants were found to stabilize proteins in ionic liquids[80].

In spite of the promising application as reaction media, the research on solvation process of the solutes in ionic liquids is far from conclusive. The solute dynamics are not revealed and some minor changes to the composition of the ionic liquid system could greatly change the observed phenomena. For example, some of the inorganic salts are not very soluble in ionic liquids[81], which is surprising because the ionic liquids should have similar structure and microscopic forces as inorganic salts and "like dissolves like". Another example is that a small amount of water can potentially change the properties of ionic liquids drastically[82].

To fully utilize the advantange of ionic liquids as a solvent, the solute structure and dynamics are important to study. In this thesis, we will study the solute dynamics of inorganic salts in ionic liquids, and the ion-pair stability of the inorganic salts. We will also look at the thiocyanate dynamics in water-saturated ionic liquids (chapter 4 and 5).

1.2.3 Ionic liquid under confinement

Due to the difference in their physical and chemical properties, ionic liquids rarely dissolve in organic solvents. It has been found, however, that the surfactant can form microscopic structures with ionic liquids in organic solvents, thus dissolve them. This tertiary system is industrially interesting because it contains two distinct microscopic environments, separated on the nanometer length scale. Indeed, experiments have found that such systems can be useful as nano-reactors, since some reactions can be accelerated[83,84]. Some proteins have higher activity when entrapped inside those colloidal dispersions[85]. There are also discussions about using the clusters to synthesize nanoparticles[86,87].

The system is not well understood, however, due to a lack of in-depth structure and dynamics study. The system is typically referred as reverse micelles, but other than a positive correlation between the size and the ionic liquid-to-surfactant ratio, there is no other evidence to prove this. The ionic liquid dynamics are also not studied, so the reason for their catalytic behavior is not known. In chapter 6, we will use 2D-IR to directly probe the dynamics of ionic liquids under confinement, and try to answer these questions.

1.3 SUMMARY

2D-IR is a non-linear spectroscopy that can resolve ultrafast structure and dynamics of solvents and solutes. 2D-IR has been successfully applied to molecular liquids to study the hydrogen bonding dynamics, solute ion-pairing and water dynamics under confinement. Ionic liquids are room-temperature molten salts in which each formula unit is a pair of cation and anion. Their special structure grants special properties and many potential applications, but at the same time complicates the microscopic structure and dynamics. In this thesis, I will employ 2D-IR to answer three questions about the dynamics of ionic liquids: (1) the solvent dynamics of ionic liquids, and the molecular origin of viscosity; (2) the dynamics of small solutes in ionic liquids, especially the ion-pair made of inorganic salts; (3) the structure

of the ionic liquid-surfactant microscopic structures and the dynamics of ionic liquids under confinement.

2.0 THE EXPERIMENTAL SETUP OF TWO-DIMENSIONAL INFRARED SPECTROSCOPY

This Chapter will be focusing on the experimental aspect of 2D-IR. The experiment starts with a commercial femtosecond pulsed light source with central frequency at 800 nm. The optical parametric amplifier converts the near-IR pulse into the desired mid-IR pulse of desired wavelength. A 2D-setup in pump-probe geometry splits the mid-IR pulse into the correct pulse sequence and sends them through the sample to generate signal. The signal is diffracted on a grating and measured by an array detector. The acquired data is processed to generate the 2D-IR spectra, and fitted with ellipticity to resolve frequency-fluctuation correlation function.

2.1 FEMTOSECOND MID-IR PULSE GENERATION

The 2D-IR experiments require femtosecond laser pulses in the mid-IR region. An optical parametric amplifier (OPA)[88] is often used to convert visible or near-IR pulses from commercial laser source to the desired frequency.

A Coherent Vitesse oscillator pumped by a Coherent Verdi Nd:YVO_4 laser (532 nm) generates modelocked, sub-100fs pulses at 80MHz repetition rate (∼800nm, 300mW). This laser pulse is then used as a seed pulse for Coherent Legend Elite chirped pulse amplifier to generate 803 nm laser pulses at a 5 kHz rate with a total power of ∼4 W. Approximately

1 W of the 803 nm laser pulse is sent into a home-built OPA to generate mid-IR pulses of tunable frequency.

The OPA contains three major steps to convert the 803 nm light into mid-IR femtosecond pulses. The first step is to generate a supercontinuum white light that is used as the seed (signal) pulse. The second step is the optical parametric amplification process that amplifies the signal frequency with the 803 nm pump and generates an idler light which is the difference frequency between the pump light and the signal light. The final step is to generate the desired mid-IR pulse which is the difference frequency of the signal and idler pulses.

2.1.1 White light generation

The signal beam for the optical parametric amplification process is generated by white-light generation. If a high-intensity pulse is focused into a transparent non-linear material, the output will be a broad-band supercontinuum white light, regardless of its original frequency. This spectral broadening process is mainly driven by self-phase modulation (SPM), which leads to the generation of broad range of frequencies and self-focusing effect, which gives high peak intensities. The result of white light generation is a broad-band, femtosecond pulse that covers the entire seed pulse frequency range for the optical parametric amplification process.

The white light generation process in the OPA occurs in a Sapphire crystal. Approximately 3% of 803 nm input light is sampled by a beam sampler (BS-1). The light, which is originally horizontally polarized, is changed to vertical polarization after propagating through a set of half waveplate and wire-grid polarizer (WL). The beam passes through an iris (IR-1), and is then focused onto a Sapphire crystal to generate the white light. The white light is then re-collimated to 1/3 of the original 803 nm beam size. The beam passes through a longpass filter (FL-1) to filter out the visible region intensity, leaving only the frequencies in the IR region. The energy per pulse after the filtration is typically 0.3 μJ.

The beam profile of the output white light depends highly on the total input energy: when the energy is lower than a critical energy density, no supercontinuum is generated;

when the energy is too high, the beam will break up into filaments and randomly modulate in spatial intensity. Therefore, to obtain a proper Gaussian shaped white light, an iris is placed in front of the focusing optics. The aperture size controls the energy density at the focus in the Sapphire crystal. Empirically, proper generated signal pulses should be white in color, and have smooth Gaussian shape with a uniform red-colored ring on the edge.

2.1.2 Optical parametric amplification

The optical parametric amplification process converts the energy of a higher-frequency pulse (the pump) into a lower-frequency pulse (the probe) while generating an idler pulse of which the energy is the difference between the photon energies of pump and signal wave.

Phase-matching between the pump and signal beam is required for this process. When the two pulses are phase matched, their relative phase does not change during their propagation in the media. This is possible in non-centrosymmetric crystals such as Type II B Barium borate (BBO) crystal, where the index of refraction is a function of polarization. If the light propagates with its polarization aligned to the ordinary axis of the crystal, it has highest velocity; if the light propagates aligned to the extraordinary axis, it has lowest velocity. By tuning the angle of the crystal, the velocity of the light could be anywhere between the highest and lowest velocity. By tuning the non-linear crystal, the signal of desired frequency could be phase-matched with the pump beam, triggering the OPA process.

In our setup, we use Type-II phase matching. The idler light will have the same polarization as the pump light, while the signal light has its polarization perpendicular to the pump and idler. We use a two-stage amplification setup, meaning that the OPA process is triggered two times in the system with two pump beams.

The generated white light in the previous step is sent into the BBO crystal as the signal beam after passing through a dichroic mirror (DCM-I). The remainder 97% of the 803 nm light from the BS-1 is the pump beam. The pump beam first reflects back from the mirrors on a translation stage (RR-1 and RR-2), and then is split into two pumps by a 10/90 beam

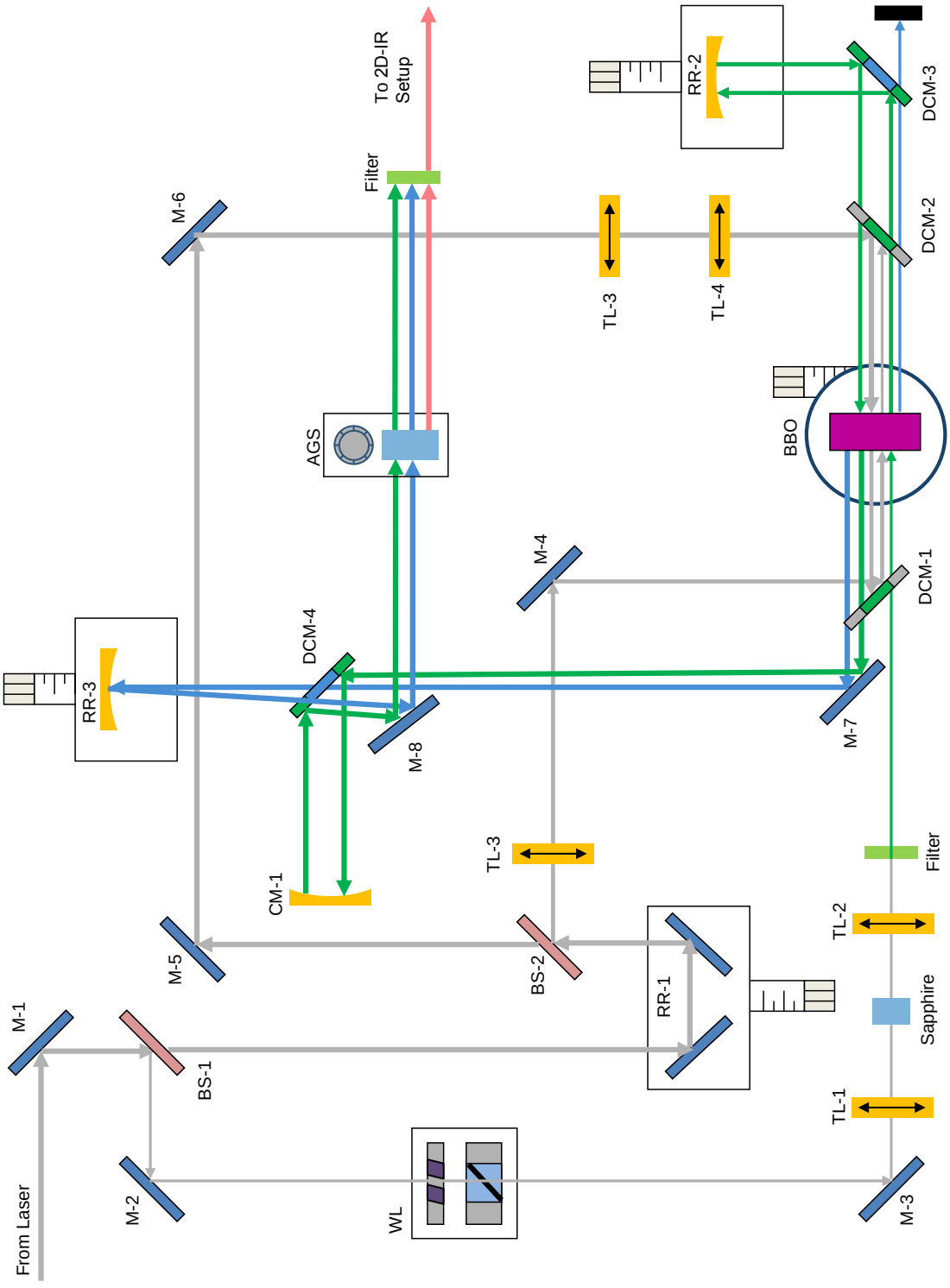

Figure 3: The schematic drawing of the optical parametric amplifier. The arrows indicate the path and the direction that lights propagate. The gray arrows represent the 803 nm laser light; the green arrows represent the signal pulse; the blue arrows represent the idler light; the red arrows represent the generated mid-IR pulse.

splitter (BS-2). The reflected 10% beam is the pump-I, which is then focused onto the BBO crystal after reflecting from the DCM-1. The pump-I and signal beams are spatially and temporally overlapped in the BBO crystal and converted into signal (1.4 μm) and idler (1.94 μm) via Type II phase matching process.

The output from the BBO is a mixture of the pump-I, signal and reference, while only the signal is required for the 2nd-stage OPA. The mixture the passes through another dichroic mirror (DCM-2), where the pump beam is reflected and blocked. A second dichroic mirror (DCM-3) reflects the desired signal beam while transmits the idler beam. A convex mirror placed on a translation stage (RR-3) reflects and collimates the signal beam , sending the signal beam through the vertically displaced path back to the BBO.

The pump-II, after transmitting from BS-2, is shrunk to 1/5 of its original size after passing through a telescope. The pump-II is spatially and temporally overlapped with the signal beam after reflecting from the DCM-2. The pump-II is then converted into signal and idler beams of the same frequencies as the 1st-stage OPA process.

The outcome of the OPA process is a pair of signal and idler beam that travel along the same direction. The signal beam has a center frequency of 1.4 μm, and is vertically polarized. The idler beam centers at 1.94 μm, and is horizontally polarized. The total energy of the two beam is typically 50 μJ per pair of pulses.

The OPA process requires the pump beam and the signal beam are overlapping both in space and time. The dichroic mirrors selectively reflect one beam while transmitting another, and the beams can be collinear after the mirrors. The translation stages are used to control the time-delay between different pulses. The first translation stage (RR-1) controls the timing between the white light and both pump pulses, while the second translation stage (RR-2) manipulates the overlapping between pump-II and the reflected signal beam in the second stage of OPA process.

2.1.3 Difference frequency generation

The final step of the OPA apparatus is to generate the mid-IR light of desired frequency from the signal and idler pulses. The energy of the mid-IR pulse is the difference between the energy of the signal pulse and the idler pulse, and this process is called difference frequency generation (DFG).

Similar to OPA process, DFG also requires a birefringence crystal to phase-match the signal and idler. The difference lies in that DFG is Type-I phase matching, where the generated mid-IR beam has the same polarization as the lower-energy pulse (the idler).

The mixture of signal and idler beam from the BBO is reflected off of a gold mirror into a interferometer. The dichroic mirror (DCM-4) serves as a beam splitter to separate the signal and idler beam into different paths. The signal is reflected on a focusing mirror, while in the idler path, a same focusing mirror is placed on a translation stage (RR-3). The two beams are recombined and sent into a silver gallium sulfide (AGS) crystal to generate the mid-IR pulse. A longpass filter blocks the signal and idler beam, leaving only the mid-IR beam. The IR pulse is collimated with concave gold mirror and is sent into 2D-setup.

The output of the DFG is parallel polarized femtosecond mid-IR pulse of desired frequency. Typically the energy of each pulse is 2 μJ, with approximately 200 cm^{-1} bandwidth.

Because the frequencies of the signal and reference beams are different, they have different indices of refraction. When travelling through optical parts, they are gradually separated in space and time. The Michelson interferometer has enough degrees of freedom to overlap them in the AGS crystal.

The interferometer in the setup looks like a Michelson interferometer, but it is actually slightly modified. Since the two beams are not of the same frequency, a dichroic mirror is used to separate them into different paths, rather than a beam splitter. Consequently, when the beams are recombined at the dichroic mirror after reflected, the only direction of propagation will be the opposite of the incoming direction. In this case, the two reflecting concave mirrors are placed so that the beams are reflected at a slight angle. After trespassing

the dichroic mirror, the beam is spatially separated from the incoming beam. Finally a gold mirror is used to direct the beam to the AGS crystal.

2.2 2D-SETUP

To perform a 2D-IR experiment, a 2D-IR setup[89] is implemented after the OPA to generate the correct pulse sequence: two pump pulses, one probe pulse and one reference pulse. The time ordering of the pulses are controlled by two translation stages, and the experiments are performed in pump-probe geometry with self-heterodyne detection. In the setup, a He-Ne laser beam is also used to accurately determine the distance of the translation stage.

2.2.1 Generating probe and reference beam

Upon entering the 2D-IR setup, the mid-IR beam is sent through a wedged CaF_2 window (CF) to generate the probe pulse and reference pulse. The front surface and back surface of the window reflect approximately 5% and 3% of the total energy, and become the probe and reference beam respectively. The two surfaces have a dihedral angle of 1.5 degrees, which can separate the probe and reference in the vertical direction as they propagate. The two beams travel freely until they are separated by approximately 2 cm. A pair of stacked square gold mirrors (SM-1) are each placed in the probe and reference beam path to make the two beams travel parallel to each other. The collimated beams are then sent to the sample area with a pair of 2-inch flat gold mirrors.

2.2.2 The interferometer controls the timing of the two pump pulses

There is a Mach-Zehnder interferometer to control the timing profile of the two pump beams. This interferometer contains two levels. In the lower level the mid-IR beam is split into two

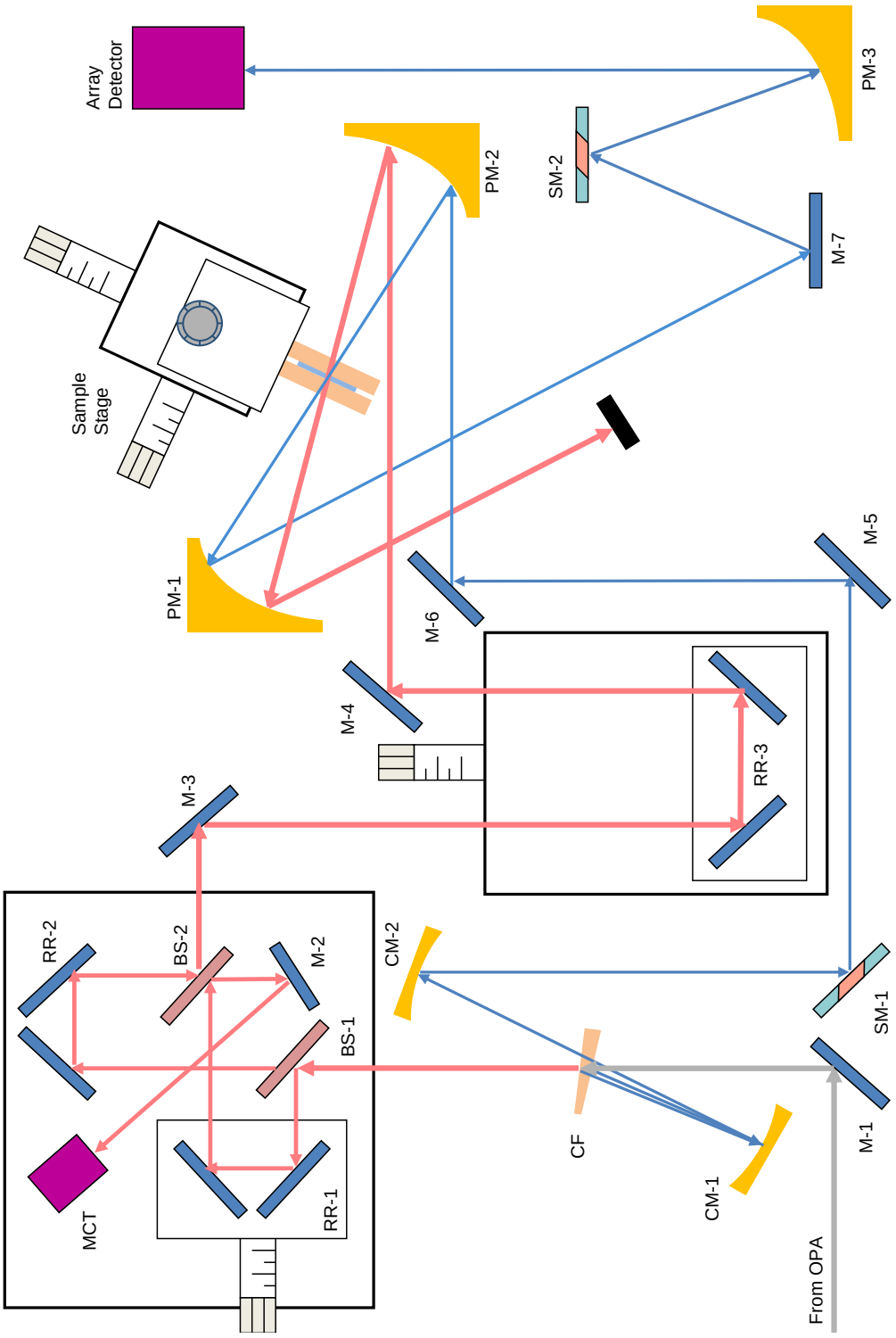

Figure 4: The schematic drawing of the 2D-IR setup. The arrows indicate the direction that lights propagate. The red arrows represent the pump, while the blue arrows represent the signal and reference beam.

pumps that travel at the collinearly. In the upper level, a He-Ne beam travels parallel to the mid-IR, and is responsible for accurately determination of the timing of the two pump pulses.

After the CaF_2 window, the remainder beam, which contains over 90% the total energy, is sent into the lower level of a Mach-Zehnder interferometer. In the interferometer, the beam is first split by a 50/50 beam splitter (BS-1) into two beams, each travelling a different path, namely stationary and mobile path. Each path has a pair of gold mirrors that are aligned 90 degrees to each other to reflect the beam back. In the mobile path, there is a translation stage (coherent stage, controls the t_1 time) to modify the timing between the two pump pulses. Two paths reflect the beams into another 50/50 beam splitter to further split the two beams each into two components. The two sets of pulses are replica of each other except for travelling in different directions. In each direction, the two components are travelling collinearly. One set of the component is used as the two pumps of the 2D-IR experiment. The other set is guided into a single channel Mercury-Cadmium-Telluride (MCT) detector to determine the interferogram of the two pump beams. The interferogram is used in the 2D-IR experiment to obtain the origin of the timing of the two pump beams.

To unambiguously determine the distance that the coherent stage has traveled, we use quadrature fringe counting, therefore a continuous wave He-Ne laser beam is introduced in the upper level of the interferometer. The He-Ne beam enters the 2D-setups right after the CaF_2 wedged window, parallel to the pump beam, and propagates approximately 2 cm on top of the pump beam. The He-Ne passes through the interferometer, and in the stationary path, the beam is rotated into a circularly-polarized light via a quarter wave plate. The beams of the stationary and mobile path recombined after the interferometer, and is polarization-selected by a broadband polarizing beamsplitter cube into parallel and perpendicular polarizations. The split beams of different polarizations are each detected by a photo-diode.

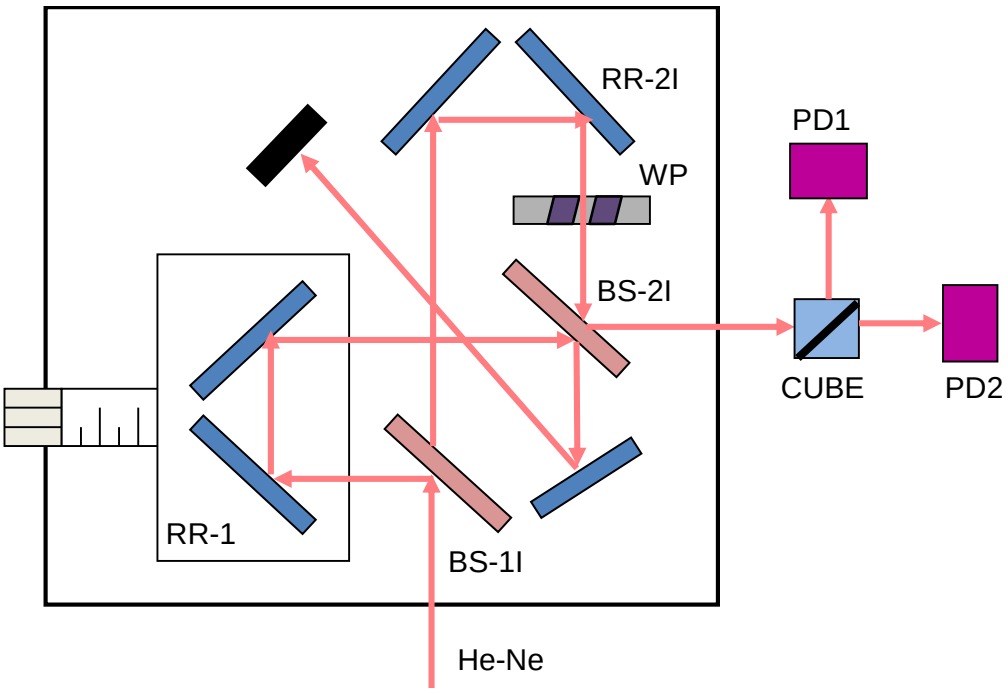

Figure 5: The schematic drawing of the He-Ne beam travelling above the mid-IR beam.

2.2.3 Controlling the population time

Before the pumps are sent into the sample, they are reflected back from another translation stage (population stage, controls the t_2 time) to control the time delay between the pump pulses and the probe pulse. The translation stage is capable of travelling from -50 to 250 ps, and the t_2 time is direct read out from the stage.

The beam after reflection is controlled by a gold mirror to travel parallel to the probe and reference to the sample area.

2.2.4 The sample area

The sample area is composed of two off-axis parabolic mirrors and one 3-axis translation stage. The off-axis parabolic mirrors form a telescope, and is used to focus the beams onto

the sample. The translation stage has a sample holder attached to it, and is used to control the position of the sample.

The four beams are focused onto the sample via an off-axis parabolic mirror at different angles. The two pump pulses and the probe pulse are focusing on the same point inside the sample, while the reference beam is tuned to be focusing at a different spot. After the sample, the beams are re-collimated with another off-axis parabolic mirror. The pump pulses are blocked after the sample area, leaving only probe pulse and reference beams travel into the detector.

The experiment is conducted in a pump-probe geometry, and due to the wave-mixing property of 2D-IR, the generated 3rd order signal propagates at the same direction as the probe pulse.

2.2.5 The 2D-IR signal detection with array detector

The probe and reference pulses hit a pair of stack mirror before the detector. Their purpose is to fine tune the pointing of the two beams. The stack mirrors send the two beams into another off-axis parabolic mirror, which focuses the two beams into two focal points that are vertically aligned at the entrance of the detector.

Once entering the detector, the two beams are dispersed on a 50 line/mm grating into monochromatic lights. The dispersed light are detected by two vertically aligned arrays of detectors. Each array has 32 different channels, and detects the wavenumber ranging from 1950cm^{-1} to 2150cm^{-1}. The readings from the two arrays will be used to construct the final frequency axis in the 2D-IR spectra.

3.0 ULTRAFAST STRUCTURE AND DYNAMICS IN IONIC LIQUIDS: 2D-IR SPECTROSCOPY PROBES THE MOLECULAR ORIGIN OF VISCOSITY

The text in this chapter has been adapted from Ren, Z.; Ivanova, A. S.; Ren, Z.; Couchot-Vore, D.; Garrett-Roe, S. *J. Phys. Chem. Lett.* **2014**, *5(9)*, 1541-1546. The author's contribution to the work included choosing the systems of study, conducting the FTIR and 2D-IR experiments, and writing the text of the manuscript.

3.1 CHAPTER SUMMARY

The viscosity of imidazolium ionic liquids increases dramatically when the strongest hydrogen bonding location is methylated. In this work, ultrafast two-dimensional vibrational spectroscopy (2D-IR) of dilute thiocyanate ion ($[SCN]^-$) in 1-butyl-3-methylimidazolium bis-(trifluoromethylsulfonyl)imide ($[C_4C_1im][NTf_2]$) and 1-butyl-2,3-dimethylimidazolium bis-(trifluoromethylsulfonyl)imide ($[C_4C_1C_1^2im][NTf_2]$) shows that the structural reorganization occurs on a 26 ± 3 ps timescale and on a 47 ± 15 ps timescale, respectively. The results suggest that the breakup of local ion cages is the fundamental event which activates molecular diffusion and determines the viscosity of the fluids.

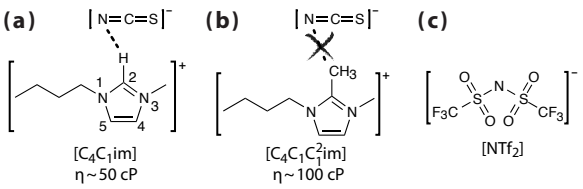

Figure 6: Blocking the strongest hydrogen bonding site of the imidazolium ring causes a substantial increase in viscosity. **a)** The hydrogen bonding between the $[C_4C_1im]^+$ cation and the SCN^- anion occurs at the 2-position; **b)** methylating the 2-position in the $[C_4C_1C_1^2im]^+$ cation blocks the hydrogen bond; and **c)** the $[NTf_2]^-$ anion. Numbering of the ring-positions are indicated.

3.2 MAIN TEXT

Viscosity is a critical property to optimize for applications of ionic liquids in advanced separations (*e.g.* carbon capture)[90], energy storage[91], solar energy[92], and tribology[93]. The molecular causes of viscosity in these fluids, however, can be counterintuitive. For example, all other properties being equal, a *decrease* in hydrogen bonding in imidazolium ionic liquids can lead to a dramatic *increase* in viscosity[94] (Figure 6). Here, we directly measure the dynamics of structural reorganization in two archetypal ionic liquids, 1-butyl-3-methylimidazolium bis-(trifluoromethylsulfonyl)imide ($[C_4C_1im][NTf_2]$) and 1-butyl-2,3-dimethylimidazolium bis-(trifluoromethylsulfonyl)imide ($[C_4C_1C_1^2im][NTf_2]$) on the femtosecond to 200 picosecond timescale using two-dimensional ultrafast vibrational spectroscopy (2D-IR). An Arrhenius analysis shows that the relative barriers to reorganization in these two ionic liquids are different by ~ 1.5 kJ/mol. The data suggest that the lifetimes of ion-cages dictate the viscosity difference in these ionic liquids.

The difficulty of understanding the molecular origin of viscosity in ionic liquids derives from the same features that make ionic liquids promising 'green solvents'[95,96]. Ionic liquids are molten salts, usually composed of organic cations and anions, which have a melting

temperature at or below roughly 100 °C[95,96]. The strong electrostatic interactions lead to high cohesive energies[97] (approaching 60% of NaCl) and extremely low vapor pressures. In addition, dispersion forces are essential for reducing melting points[97], and hydrogen bonding can have a major impact on the liquid properties[90,94,98–101]. The interplay of these forces can generate structural and dynamical complexity – both heterogeneous structure[102–104] and heterogeneous dynamics[103,105].

The competition between these interactions is an important part of why hydrogen bonding might cause such variation in viscosity. One hypothesis is that strong and directional hydrogen bonding disrupts an ordered array of charges, which fluidizes the liquid[98]. A different view is that the methyl group at the 2-position of the imidazolium ring blocks a number of low energy configurations; this reduced configurational space leads to a reduced entropy, more ordered fluid, and, hence, a higher viscosity[106]. A third proposal is dynamical, rather than thermodynamic. The 2-position methyl group can increase the free-energy barrier for the anion to move relative to the imidazolium cation[107]. Gas-phase calculations show that the barriers for important modes of structural relaxation are increased by as much as 20 kJ/mol, shutting off this relaxation channel and increasing the viscosity.

Ultrafast vibrational spectroscopy has time-resolution fast enough to capture intermolecular motions which are often too fast for standard spectroscopies like NMR or dielectric relaxation[108]. 2D-IR spectroscopy is often a more local probe of dynamics than other optical and vibrational spectroscopies. With the suitable choice of vibrational probe molecule, the 2D-IR measurement is sensitive to the immediate surroundings of a molecule. In contrast, solvation dynamics experiments on large dyes in solution[108–114] often represent the average over many intermolecular interactions. Similarly, Kerr effect based spectroscopies, such as optically heterodyne-detected Raman induced Kerr effect spectroscopy (OHD-RIKES), report on the low-frequency vibrational modes of the liquid averaged over all components of the liquid weighted by the Raman polarizability[111,115–117]. This weighting and its collective nature makes it sometimes hard to separate individual intermolecular components of the Raman response. Optical[108–114] and Raman[111,115–117] spectroscopies have revealed a great deal about the hierarchy of timescales of structural relaxation in these fluids, but the details

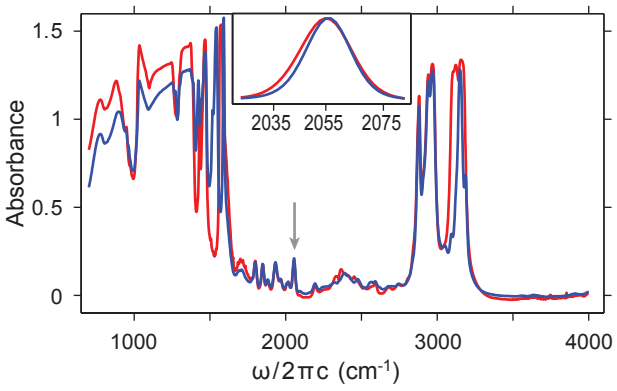

Figure 7: FT-IR spectroscopy of SCN^- in $[C_4C_1im][NTf_2]$ (red) and $[C_4C_1C_1^2im][NTf_2]$ (blue). (inset) The nitrile stretching mode of SCN^- which serves as a marker mode for structural relaxation.

of structural rearrangement around particular ions, however, have remained elusive.

We chose thiocyanate, SCN^-, as the vibrational probe molecule because it is a typical ionic liquid anion, it has a high extinction coefficient, nitrile stretching frequencies are known to be sensitive to the ionic liquid environment[118], and it has a sufficiently long vibrational relaxation time to allow us to measure the important dynamics[119]. To eliminate the possibility of energy transfer between thiocyanates we dissolve ~30 mM $[C_4C_1im][SCN]$ in $[C_4C_1im][NTf_2]$ and ~30 mM $[C_4C_1im][SCN]$ in $[C_4C_1C_1^2im][NTf_2]$. In both systems the C=N absorbs near 2050 cm^{-1} (Figure 7), with an extinction coefficient of 840 $M^{-1}cm^{-1}$ assuming a constant density of 1.44 g/mL[120]. The full width at half maximum (FWHM) of the vibrational absorption varies from 20.2 cm^{-1} in $[C_4C_1C_1^2im][NTf_2]$ to 23.2 cm^{-1} in $[C_4C_1im][NTf_2]$ in agreement with Owrutsky *et al.*[119]. Stronger hydrogen bonds are often associated with red-shifted vibrations, indicating that methylation does cause a less hydrogen-bonded environment for the $[SCN]^-$. It also shows that, in $[C_4C_1im]][NTf_2]$, the $[SCN]^-$ can effectively compete against the larger, less basic $[NTf_2]^-$ for hydrogen bonding sites[121].

The FTIR data give a hint of different structures, but the larger linewidth could come

from either faster dynamics or increased disorder. Ultrafast 2D-IR, on the other hand, can distinguish disorder and dynamics. The 2D-IR experiment is a coherent vibrational-echo spectroscopy analogous to the spin-echo spectroscopies of NMR[1]. If the vibrational frequency of a molecule depends on the local structure, then, as the local environment flucutates, so does the frequency. In general terms, the 2D spectrum is a correlation plot of initial frequencies, ω_1, and final frequencies, ω_3, given a time separation, t_2. The loss of correlation can be read off the spectra in terms of the change of the shape of the 2D-IR peaks.

The 2D-IR spectra of SCN^- in $[C_4C_1im][NTf_2]$ and $[C_4C_1C_1^2im][NTf_2]$(Figure 8a,b) each have two peaks. The first peak (blue), located on the ω_1-ω_3 diagonal, originates from stimulated emission and ground state bleach at the $v = 0 \rightarrow v = 1$ energy. The second peak (red), located below the ω_1-ω_3 diagonal, comes from vibrational excited state absorption at the anharmonically shifted $v = 1 \rightarrow v = 2$ energy.

When a system has little time to evolve, *e.g.* the 0.2 ps spectrum of SCN^- in $[C_4C_1im][NTf_2]$ (Figure 8a, left), the two features are stretched along the frequency diagonal indicating that different local environments give rise to different local vibrational frequencies. The inhomogeneous (diagonal) linewidth of the lobes is 18.8 ± 0.2 cm^{-1}, while the homogeneous (antidiagonal) linewidth is 7.6 ± 0.1 cm^{-1}. With a large ratio of $\sigma_d/\sigma_a = 2.47 \pm 0.04$, the system is inhomogeneously broadened and can be considered within the inhomogeneous limit. The two lobes are separated by an anharmonicity of 27.4 ± 0.2 cm^{-1}.

As the system is given more time to evolve, *e.g.* 100 ps, the local structures interconvert, which in turn causes the vibrational frequencies to change. Molecular diffusion causes spectral diffusion, and the spectra become round (Figure 8a,right). At 100 ps, the diagonal width and antidiagonal width each equal 14.5 ± 0.2 cm^{-1} and 14.3 ± 0.2 cm^{-1}, respectively. Since σ_d/σ_a decreased to 1.01 ± 0.02, the system has lost most of the correlation, though some residual correlation can be observed in the small tilt of the nodal line between the 0 to 1 and 1 to 2 transition peaks. The loss of correlation is complete by $\sim$ 200 ps (Supplemental Information).

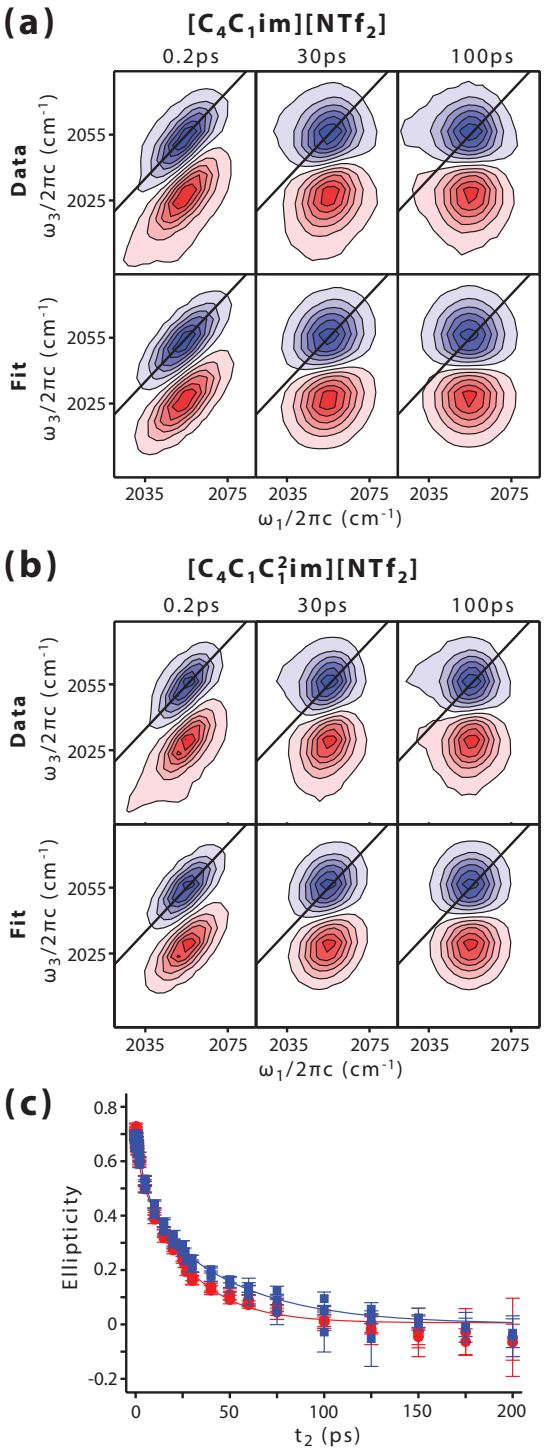

Figure 8: 2D-IR spectroscopy of a) 30 mM SCN^- in $[C_4C_1im][NTf_2]$ and b) 30 mM SCN^- in $[C_4C_1C_1^2im][NTf_2]$. c) The change in ellipticity as a function of time shows that dynamics of structural reorganization in $[C_4C_1C_1^2im][NTf_2]$ (blue) are slower than in $[C_4C_1im][NTf_2]$ (red).

Similarly, the 0.2 ps spectrum of 30 mM SCN^- in $[C_4C_1C_1^2im][NTf_2]$ (Figure 8b, left) has a diagonal width of 16.3 ± 0.2 cm^{-1}, and an antidiagonal width of 6.8 ± 0.2 cm^{-1}, which gives a $\sigma_d/\sigma_a = 2.65 \pm 0.10$. The two lobes are separated by an anharmonicity of 27.0 ± 0.2 cm^{-1}. The peak-shape changes on a similar but slower timescale than $[C_4C_1im][NTf_2]$. At 100 ps, the spectrum is rounder but, nevertheless, is more tilted than $[C_4C_1im][NTf_2]$. The diagonal width and antidiagonal width equal 12.6 ± 0.2 cm^{-1} and 12.0 ± 0.2 cm^{-1}. The σ_d/σ_a is now equal to 1.05 ± 0.03, which is greater than $[C_4C_1im][NTf_2]$, showing that the dynamics are slower.

The rate of structural change can be quantified by a variety of methods[122,123] to extract a frequency fluctuation time-correlation function. We fit the spectra to two two-dimensional Gaussian peaks (Figure 8a,b bottom) and analyze the change in their ellipticity as a function of time[122] (Figure 8c). The ellipticities of both systems change in a biexponential fashion,

$$C(t) = A_1 \exp(-t/\tau_1) + A_2 \exp(-t/\tau_2). \tag{3.1}$$

The ellipticities start at $\sim$0.7 ($t_2 \approx 0$) due to fast fluctuations that are in the motional narrowing limit, probably due to librations. For both $[C_4C_1im][NTf_2]$ and $[C_4C_1C_1^2im][NTf_2]$, the first timescale is roughly a few picoseconds ($\tau_1 = 1.4 \pm 0.5$ ps and 6.4 ± 2.2 ps, repectively), and the amplitudes are relatively small ($A_1 = 0.13 \pm 0.03$ and 0.24 ± 0.07, repectively). The second timescale is $\tau_2 = 26 \pm 3$ ps in $[C_4C_1im][NTf_2]$ and nearly a factor of two slower, 47 ± 15 ps, in $[C_4C_1C_1^2im][NTf_2]$. In both systems, this timescale is responsible for the majority of the observed spectral diffusion ($A_2 = 0.60 \pm 0.02$ and 0.45 ± 0.05, repectively). The ellipticity eventually goes to 0 within experimental error, indicating that both systems have completely lost the memory of their initial conditions within 200 ps.

MD simulations by both Kirchner and Maginn give the lifetime of ion-pairs and ion-cages on the same range as the second timescale that we measure[100,101,124]. Based on these calculations, we assign the faster motion, *i.e.* the motion on the $\sim$2 ps timescale, to the SCN^- ion rattling inside a local ion cage, without significant reorganization of the environment; this motion causes less spectral diffusion. We assign the slower motion, *i.e.* the motion on the $\sim$30 ps timescale, to the breaking and reforming of the ion complexes; since this

process greatly changes the local environment of the SCN^-, it dominates the observed spectral diffusion.

Though $[C_4C_1C_1^2im][NTf_2]$ has slower dynamics than $[C_4C_1im][NTf_2]$ by a factor of nearly 2, the dynamics of the two ionic liquids are of the same order of magnitude. We can approximately calculate the energy barrier difference by assuming that the dynamics obey Arrhenius behavior,

where superscripts (1) and (2) stand for the different cations, $\tau_2^{(i)}$ is the second timescale from Equation 3.1 for species i (which we have assigned as the reorganization of ion complexes around the SCN^-), $E_a^{(i)}$ is the rate limiting activation energy for structural relaxtion of species i, k_B is the Boltzmann's constant, and T is the temperature. This gives an energy difference of $\sim$1.5 kJ/mol. This energy barrier difference disagrees by an order of magnitude with the prediction of MacFarlane *et al.*[107], who, in gas phase electronic structure calculations, calculated the activation energy for translation of an anion from one side of the imidazolium ring to the other going around the 2-position. On the one hand, our experiment might not be sensitive to direct transitions between these configurations if their frequency fluctuation correlation functions are very similar. On the other hand, our results indicate that facile routes to structural reorganization still exist after methylation at the 2-position without necessitating crossing such a high barrier.

Our results give some support to the entropic hypothesis of Hunt[106]. The SCN^- in $[C_4C_1im][NTf_2]$ shows a broader inhomogeneous linewidth than SCN^- in $[C_4C_1C_1^2im][NTf_2]$. Since the inhomogeneous linewidth is an observable that quantifies the distribution of different environments, this indicates SCN^- has more possible configurations in $[C_4C_1im][NTf_2]$. The FTIR results (Figure 7) agree but are less conclusive because both structure and dynamics can influence the total linewidth.

Our results also suggest a new hypothesis. The ratio of ion-cage lifetimes that we measure ($47/26 = 1.8 \pm 0.2$) is nearly the same as the ratio of the viscosities. Our measurements give a ratio of $100/50 = 1.982 \pm 0.004$; literature values based on a variety of viscometers taken in the aggregate (Supplemental Information) give even closer agreement ($95/52 = 1.8 \pm 0.3$).

There is a large experimental variation in the viscosity measurements in the literature[106], and the errorbar on the τ_2 for $[C_4C_1C_1^2im][NTf_2]$ ($\pm$15 ps), so the agreement may be coincidental. A very simple model of diffusion, however, supports the association of ion-cage lifetime in our measurements and viscosity. In a random walk, assuming Stokes-Einstein behavior, the viscosity scales like $\Delta t/L^2$, where Δt is the average time between steps and L is the average length of a step. This suggests that breaking up of the local ion-cage is the fundamental event for activating translational diffusion and, hence, viscosity.

Just because the dynamics we observe are completed in less than 200 ps does not mean that there are no dynamics on longer timescales. Fluorescence spectroscopies have observed structural reorganization on up to nanosecond timescales[108–114] because the large optical chromophores have long-ranged electrostatic interactions with the surrounding liquid. Similarly, dielectric relaxation and optical kerr effect measurements[111,115–117] are sensitive to slow translational relaxation (sub-α relaxation), which is related to mesoscopic aggregates. Our spectroscopy, on the other hand, is more sensitive to the local environment around the SCN^- vibrational chromophore. The tight relationship of the lengthscale and the timescale of the structural relaxation has been calculated for $[C_4C_1im][NTf_2]$ in, for example, the time and wave-vector dependence of the self-part of the intermediate scattering function[125].

The short-range nature of the vibrational frequency shifts should also be a better measure of local structural properties like ing. The fact that the ellipticity in both samples decays to 0 in less than 200 ps is inconsistent with the proposal of long lasting ion pairs[126,127]. Our experimental results are a stringent constraint on the timescale for ion pairing and offer strong support for molecular models in which the anomalous transport properties are due to correlations between particles rather than long-lasting ion-pairs[103,128].

In this work, 2D-IR spectroscopy has shown that methylation at the 2-position of imidazolium ionic liquids increases the effective barrier to structural relaxation by less than 2 kJ/mol. The data suggest that the breaking up of ion cages is the rate-limiting step to activate translational diffusion. Further temperature-dependent studies will be able to disentangle the roles of transmission coefficients and barrier heights in determining the structural

relaxation mechanism. Ultrafast spectroscopies such as 2D-IR have a great deal of promise for providing detailed experimental results on molecular time- and length-scales which may prove valuable to validate the numerous ionic liquid force fields under development. Molecular modelling will also help refine our answers to questions such as where the SCN^- resides in the fluid and what the molecular causes of frequency fluctuations are. In addition, 2D-IR may reveal structural reorganization as relevant to energy storage (supercapacitors) and the modes of interaction between important solutes (*e.g.* CO_2) with ionic liquids (*e.g.* carbon capture sorbents).

3.3 EXPERIMENTAL METHODS

The ionic liquids were purchased from Ioli-tec. Samples were used as received. All sample storage, mixing, and spectroscopic cell assembly were performed in a nitrogen atmosphere glovebox, with H_2O concentration below 5 ppm. Spectroscopic measurements were performed under a dry N_2g purged environment. Mixtures of 30 mM $[C_4C_1im][SCN]$ in either $[C_4C_1im][NTf_2]$ or $[C_4C_1C_1^2im][NTf_2]$ were prepared and stirred overnight. Spectroscopic cells consisted of 1 μL of ionic liquid held between two 2 mm thick calcium fluoride windows which were separated by a 100 μm O-ring Teflon spacer. Water content was monitored before and after the 2D-IR experiments by FTIR spectroscopy, and water content was estimated to be less than 150 ppm for all samples (Supplemental Information).

For the 2D-IR experiment, $\sim$120 fs pulses of 800 nm wavelength were generated by a commercial Ti:Sapphire chirped pulse amplifier of 1 mJ at a repetition rate of 5 kHz. An optical parametric amplifier (OPA) generated $\sim$2 μJ tunable mid-IR pulses of sub 100 fs duration, centered at 2050 cm^{-1}, with a bandwidth of 250 cm^{-1}. For the 2D measurements we used a Fourier transform 2D-IR setup in the pump-probe geometry as described by Helbing *et al*[89] (essentially identical to that report, except the repetition rate is 5 kHz). The data acquisition was performed with a fast-scanning routine without phase ambiguity. We performed the measurements in the all parallel polarization geometry.

The change of in shape of the 2D-IR spectra over population time was quantified by ellipticities[122,123]. Error bars are estimated by propagation of error in the fits of the two-dimensional Gaussians's parameters.

Viscosity measurements were taken with a RheoSense microVISC viscometer, using the microVISC temperature controller to maintain the system at 25°C. Prior to measuring, samples were kept under vacuum to ensure dryness. Each sample was exposed to air and transferred to a pipet immediately before measuring to minimize water uptake. Water content was measured using a Metrohm 831 KF Coulometer and 860 KF Thermoprep in combination. Prior to measuring, samples were kept under vacuum to ensure dryness. Immediately before measuring, each sample was exposed to air and measured into a glass vial, which was then sealed. The glass vial was placed into the Thermoprep oven at 120°C, and dried air was flowed through the vial headspace at a rate of 50 mL/min before entering the titration vessel. Samples were run in duplicate using approximately 0.5 g of of sample for each measurement. Water content of all samples was in the range of 100 – 300 ppm and the presence of 30 mM $[C_4C_1im][SCN]$ changed the viscosities of $[C_4C_1im][NTf_2]$ and $[C_4C_1C_1^2im][NTf_2]$ by less than 0.5% (Supplemental Information).

4.0 THIOCYANATE AS A LOCAL PROBE OF ULTRAFAST STRUCTURE AND DYNAMICS IN IMIDAZOLIUM-BASED IONIC LIQUIDS: WATER INDUCED HETEROGENEITY AND CATION INDUCED ION-PAIRING

The text in this chapter has been adapted from Ren, Z.; Brinzer, T.; Dutta, S.; and Garrett-Roe, S. *J. Phys. Chem. B* **2015**, *119(13)*, 4699-4712. The author's contribution to this work included choosing the system of study, designing and conducting FTIR and 2D-IR experiments and data analysis, and writing the text of the manuscript.

4.1 CHAPTER SUMMARY

Ultrafast two-dimensional infrared spectroscopy (2D-IR) of thiocyanate ($[SCN]^-$) in 1-butyl-3-methylimidazolium bis(trifluoromethylsulfonyl)imide ($[C_4C_1im][NTf_2]$) and 1-butyl-2,3-dimethylimidazolium bis(trifluoromethylsulfonyl)imide ($[C_4C_1C_1^2im][NTf_2]$) ionic liquids can probe structure and dynamics as a function of the water content, solute counter-ion, and solute concentration. The 2D-IR of the water-saturated ionic liquids resolves two sub-ensembles, one dry and one wet local environment. When the counter-cation is a K^+, long-lived ion-pair formation between K^+ and $[SCN]^-$ is detected by the tilt in shape of long waiting time spectra. The observed dynamics are invariant to $[SCN]^-$ concentration, which indicates that the $[SCN]^-$ does not cluster in ionic liquid solution. Taken together, these results are consistent with a picture of thiocyanate as a local probe that can interrogate ultrafast structure and dynamics at a small spatial scale in ionic liquids.

4.2 INTRODUCTION

Structural and dynamical heterogeniety are hallmark features of the unique properties that ionic liquids can possess. A central hypothesis of our previous ultrafast two-dimensional vibrational spectroscopy (2D-IR) of hydrogen bonding in imidazolium-based ionic liquids[129] was that our vibrational chromophore was mostly sensitive to the local environment. If this concept is correct, vibrational spectroscopy could be an ideal modality to detect and characterize dynamical heterogeneity in ionic liquids. To test this hypothesis, we change three experimental variables which can alter the local environment of our probe molecule, namely the concentration of water, the concentration of our vibrational chromophore, and the charge-density of the counter-cation. We observe the resulting changes in the femtosecond and picosecond structural relaxation and whether or not dynamical heterogeneity results.

Ionic liquids are solvents in which each formula unit of the liquid is a cation-anion pair; they are room temperature molten salts[96,130]. Ionic liquids have many unique properties[131] and have many potential applications including carbon capture[90,132,133], energy storage[91], electrochemistry[134,135], catalysis[136,137] and biomass processing[138,139]. On the other hand, however, ionic liquids are complex, non-ideal fluids in many respects including structure[103,104,140?] , transport properties[141–143] (including non-Gaussian dynamics[105,125,144–146] and Stokes-Einstein-Debye violations[147–149]), and thermodynamics[150].

A good example of the dynamical complexity of ionic liquids is the unexpected increase in viscosities on the reduction of hydrogen bonding for the 1, 3-dialkylimidazolium-based ionic liquids[94,98,106,151]. Recently, we measured the effect of hydrogen bonding on the structural relaxation dynamics as sensed by the thiocyanate ion ($[SCN]^-$)[129]. We observed structural reorganization on a $\sim$ 25 and $\sim$ 50 ps timescale, with and without hydrogen bonding, respectively. We interpreted this difference in timescales as the difference in the time required for the break-up of local ion cages, which could be the activating event for translational diffusion.

Central to our interpretation is the hypothesis that the $[SCN]^-$ is a *local* probe of strucure

and dynamics. In this paper, we explore how general and robust this concept is by varying three experimental parameters – namely the concentration of water, the concentration of thiocyanate, and the identity of the thiocyanates's counter-cations. If these species, at low concentration, affect the dynamics of all $[SCN]^-$ molecules uniformly – in other words, if the dynamics are homogeneous – then the the vibrational frequency is likely sensitive to long range interactions. Contrarily, if these species at low concentration affect different molecules in different ways – in other words, if the dynamics are heterogeneous – then we have strong evidence that the vibrational frequency should be considered a local probe. If changing the concentration of these species causes no change, then we conclude that there is no interaction. This 'null' result can still be an important result in the context of the control experiment in which we vary the $[SCN]^-$ concentration.

The chromophores used in 2D-IR are the vibrational modes of well-defined functional groups. In molecular solvents, these modes are generally sensitive to local interactions such as hydrogen bonding, though electrostatics are clearly important.[152–157] In molecular liquids, the vibrational frequency shifts are due to the interaction of the transition dipole moment of the probe vibrational mode with the dynamic dipole field of the surrounding liquid. In ionic liquids, one might expect that the dominant interactions could be longer ranged because the transition dipole can interact with the charges of the cation and anion. As such, it is important to establish if the vibrational frequency-shifts of an anion in an ionic solution are primarily local or long-ranged.

Other ultrafast spectroscopies are sensitive to longer length-scales. Spectroscopies such as luminescence spectroscopy that employ large dyes normally average out local intermolecular components, probing dynamics on a length scale that is long when compared to intermolecular distances[108–114]. Similarly, Kerr-effect-based spectroscopies, for example, heterodyne-detected Raman-induced Kerr effect spectroscopy (OHD-RIKES), average over all components of the motions of the liquid, weighted by Raman polarizability[111,115–117]. Due to this collective nature, optical[108–114] and Raman[111,115–117] spectroscopies can reveal structural relaxation over a wide range of time-scales, but are not always capable of resolving the molecular details that cause the dynamics.

Far-infrared spectroscopy is another approach to probe the intermolecular potentials of interest. Low-energy intramolecular vibrations, such as torsions and certain skeletal motions, are located in the far infrared region, and bear information about the type and strength of intermolecular interactions such as Coulumbic force, hydrogen bonding and dispersion forces. By systematically varying the molecular structure and isotopic labelling, Ludwig et al use Far Infrared (FIR) Spectroscopy[158,159] to look at the changes in the spectra and resolve the type and strength of forces and their influence on such macroscopic properties as the melting points, viscosity or enthalpy of vaporization. FIR directly probes intermolecular motions, for example, hydrogen bonding strength is encoded in absorption frequency, but the low frequency modes of liquids tend to be collective in nature, burying the desired information in broad, overlapping bands that can be difficult to interpret.

The C≡N stretch is an widely-used chromophore with many advantageous properties for 2D-IR spectroscopy: stretch mode of C≡N bond is a strong absorption in IR region; the vibrational lifetime is known to be long enough for dynamics in the ionic liquids[119,160]. It has been shown with 2D-IR that the C≡N stretch of $[SCN]^-$ ion is capable of investigating the dynamics of ion-pair formation in molecular liquids[4,6], and the C≡N stretch of benzonitrile has proven sensitive to the local environment of ionic liquids[118,157]. Therefore, it is reasonable to expect that $[SCN]^-$ is an appropriate local probe to investigate the dynamics that happening within a limited spatial scale.

In this paper, the primary questions we explore are:

How does water impact the dynamics? Imidazolium-based ionic liquids can absorb water in ambient conditions[161], and the viscosity changes as the water concentration changes[162,163]. In our case, since ionic liquids have strong ability to form hydrogen bonds, water may potentially change the dynamics of $[SCN]^-$ due to the high water-SCN affinity. The effect could be local, if it is dominated by hydrogen-bonding, for example, or long-ranged, if it is dominated by changes in the average viscosity.

How does $[SCN]^-$ concentration impact the dynamics? Our experiment uses $[SCN]^-$ to probe the dynamics of the surrounding ionic liquids. Our working hypotheses are that the

$[SCN]^-$ does not perturb the liquid around it at this concentration (supported by viscosity measurements), and that the $[SCN]^-$ ions do not interact. Nevertheless, some ionic liquid mixtures show pronounced non-ideal mixing[121,164]. Therefore, it is crucial to test the ideality of the mixing by varying the solute concentration. Strong deviation from ideal mixing would cause a significant change of spectral diffusion upon changing the concentration of $[SCN]^-$. Therefore we explore here the concentration range from 10 mM to 60 mM to verify that the observations are reliable reporters of the dynamics of $[C_4C_1C_1^2im][NTf_2]$.

How does the counter-cation impact the dynamics? In our previous work, the vibrational frequency correlation decays to zero within $\sim$ 100 ps, suggesting that the SCN^- is fully dissociated, and there are no long-lived "ion pairs"[103,128]. It is not clear that this need be a general result. The solubility and dissociation constants of different salts are strongly cation dependent[81]. In addition, molecular dynamics simulations show that the dissociation of sodium chloride in $[C_4C_1C_1^2im][NTf_2]$ is very endothermic; the ions, therefore, remain in the form of ion pairs[40,165]. We hypothesized that changing the charge density on the cation would alter the propensity for the anion and counter-cation to remain paired in solution. We changed the counter-cation of the solute from an imidazolium (a typical ionic liquid component) to potassium (a typical inorganic salt). Since the potassium ion is smaller, has a higher charge density, and has a smaller van der Waals radius, we expect the greater electrostatic attraction to the $[SCN]^-$ to cause a higher probability to form ion pairs.

This paper is organized as follows. We begin with a more detailed description of the theory behind the 2D-IR spectroscopy (Section 4.3) and our data analysis and interpretation (Section 4.4). We then describe the experimental results for the effect of water (Section 4.5.1), the effect of counter-ion (Section 4.5.2), and the effect of $[SCN]^-$ concentration (Section 4.5.3). Finally, we discuss the physical picture that emerges (Section 4.6).

4.3 THEORY

2D-IR spectroscopy is a third-order nonlinear infrared spectroscopy in which three successive ultrafast laser pulses that are separated by picosecond timescales interact successively with the system. As a result, the sample emits a signal field which is heterodyne detected to retrieve phase and amplitude information. The first laser pulse drives the system to a coherence between ground and first excited states. After a coherence time, t_1, the second pulse drives the chromophores to a population state – either the ground state or the first excited state. After the second laser pulse, there is a population time, t_2, during which the system can freely reorganize. Then, the third laser pulse drives the system to a coherence state again, which generates the emitted signal field. The signal field is overlapped with a known electric field for phase sensitive detection and then dispersed in a spectrometer, which gives the frequency of the final vibrational coherence, ω_3. The experiment is repeated at many values of t_1, and the resulting interferograms are fourier transformed in the computer to give the frequency of the initial vibrational coherence, ω_1. The two-dimensional spectra, functions of ω_1 and ω_3, are collected as a function of t_2, which allows us to track reorganization of the environment around the vibrational chromophore.

Qualitatively, the 2D-IR spectrum describes the correlation of initial vibrational frequencies (when the first pump field arrives) and final frequencies (the time point when the third arrives) of the probe molecule. The spectrum of a molecule with a single vibrational mode has two lobes with opposite signs. The diagonal lobe comes from stimulated emission and ground-stated bleach (the $\nu = 0$ to 1 transition), while the second lobe comes from excited state absorption (the $\nu = 1$ to 2 transition) and is shifted below the diagonal line by anharmonicity. Different local environments can change the vibrational frequency of the probe molecules, and, together, they create a distribution of frequencies in the form of the diagonal width (inhomogeneous width) of the lobes. The antidiagonal width (homogeneous width) is a result of the motions that are much faster than the time to required to observe the corresponding frequency splitting, such as librational motions.

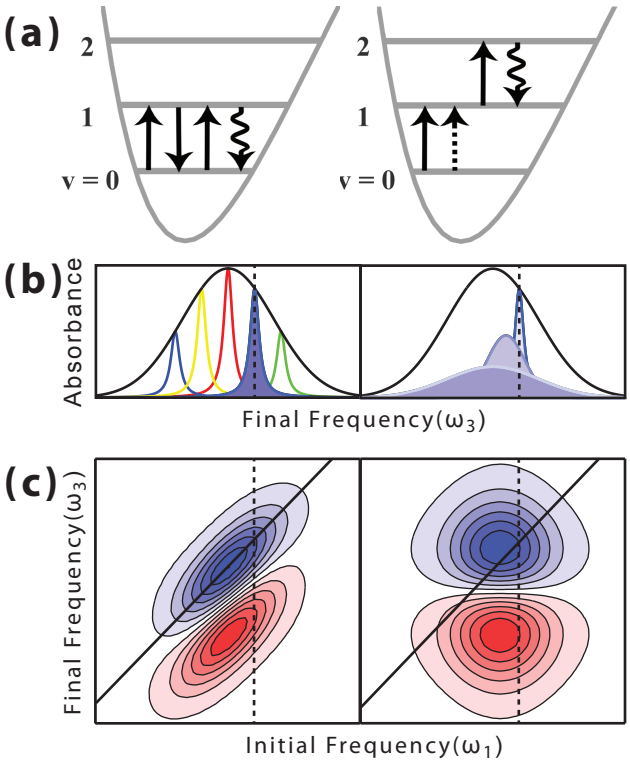

Figure 9: (a) Wave mixing diagram of ground state bleaching and stimulated emission (top), as well as excited state absorption (bottom). (b) Each subensemble of molecules generates a homogeneous linewidth, while the distribution of environments causes an inhomogeneous linewidth (left). As a molecule's environment reorganizes, its frequency randomizes, called spectral diffusion (right). (c) 2D-IR spectra record this spectral diffusion as a change in the shape (elongation) as a function of time. The spectra begin as stretched along the diagonal (left) and become round as an oscillator loses memory of its initial conditions (right).

Structural dynamics cause the 2D-IR spectra to change shape. For early population times, the surrounding environment has very little time to evolve, hence the correlation between the initial and final frequencies is high. As a result, the spectra are elongated along the frequency diagonal. Given more time, the system gradually evolves and loses the memory of its original state, which causes the spectra to have a rounder shape. This process is called "spectral diffusion", and is quantified by the two-point frequency fluctuation correlation function (FFCF), $c_2(t)$

$$c_2(t) = \langle \delta\omega(0)\delta\omega(t) \rangle \tag{4.1}$$

where $\delta\omega(\tau)$ is the fluctuation of the current frequency from the average frequency

$$\delta\omega(\tau) = \omega(\tau) - \langle\omega\rangle.$$

The FFCF, $c_2(t)$, is the key statistical information of the 2D-IR experiment, and it is useful because it can be directly analyzed to extract the timescales of the ultrafast changes of the local solvation environment. In addition, c_2 can be computed directly from molecular dynamics simulations when an appropriate mapping of simulation parameters to vibrational frequencies exists. Finally, this time-correlation function can be compared to other important time-correlation functions, such as velocity and current correlations, which determine macroscopic transport properties such as diffusivity and conductivity.

This qualitative picture is made quantitative through an analysis of the nonlinear response of the system[1]. The third-order macroscopic polarization of the sample is a convolution of the third-order molecular response function ($R^{(3)}$) with the electric fields of the three laser pulses,

$$\begin{aligned} P^{(3)}(t_3, t_2, t_1) \propto \int_0^\infty \mathrm{d}t_3 \int_0^\infty \mathrm{d}t_2 \int_0^\infty \mathrm{d}t_1 \, R^{(3)}(t_3, t_2, t_1) \\ \cdot E_3(t - t_3) \cdot E_2(t - t_3 - t_2) \cdot E_1(t - t_3 - t_2 - t_1), \end{aligned} \tag{4.2}$$

where E_n is the electric field of the n^{th} laser pulse. In the rotating wave approximation (RWA) and considering only the $\nu = 0$ to 1 transition, the $R^{(3)}$ can be simplified into two sets of pathways, namely the rephasing ($R_1^{(3)}$) and non-rephasing ($R_2^{(3)}$) pathways,

$$R_1^{(3)}(t_3, t_2, t_1) \propto \left\langle \exp\left(+i \int_0^{t_1} \delta\omega(\tau) \mathrm{d}\tau \; - i \int_{t_2+t_1}^{t_3+t_2+t_1} \delta\omega(\tau\prime) \mathrm{d}\tau\prime \right) \right\rangle, \tag{4.3}$$

$$R_2^{(3)}(t_3, t_2, t_1) \propto \left\langle \exp\left(-i \int_0^{t_1} \delta\omega(\tau) \mathrm{d}\tau \; - i \int_{t_2+t_1}^{t_3+t_2+t_1} \delta\omega(\tau\prime) \mathrm{d}\tau\prime \right) \right\rangle. \tag{4.4}$$

If the decay of coherence during t_1 and t_3 is relatively fast compared with the correlation time of the frequency fluctuations, then the system is in the so-called inhomogeneous limit. In this limit, the t_1 and t_3 are too short for the frequencies of single molecules to fluctuate, and therefore $\int_0^{t_1} \delta\omega(\tau) \mathrm{d}\tau \approx \delta\omega t_1$. As a result,

$$\begin{aligned} R_1^{(3)}(t_3, t_2, t_1) &\propto \left\langle \exp\Big(+i\delta\omega_1 t_1 - i\delta\omega_3 t_3 \Big) \right\rangle, \\ \equiv \int_{-\infty}^{+\infty} \mathrm{d}\delta\omega_1 \int_{-\infty}^{+\infty} \mathrm{d}\delta\omega_3 \, p(\, \delta\omega_3, t_2 | \delta\omega_1, 0\,) &\exp\Big(+i\delta\omega_1 t_1 - i\delta\omega_3 t_3 \Big), \end{aligned} \tag{4.5}$$

where $p(\, \delta\omega_3, t_2 | \delta\omega_1, 0\,)$ is the joint probability density, *i.e.* the probability of finding a molecule at a frequency of $\delta\omega_3$ at time t_2 *given that* it was initially frequency $\delta\omega_1$ at time 0.

The experiment, after the Fourier cosine transform, yields purely absorptive 2D-IR spectra[166,167] which are proportional to $p(\, \delta\omega_3, t_2 | \delta\omega_1, 0\,)$,

$$\begin{aligned} R^{(3)}(\omega_3, t_2, \omega_1) &\propto \Re\left(\mathscr{F}\big(R_1^{(3)}(t_3, t_2, t_1) + R_2^{(3)}(t_3, t_2, t_1) \big) \right), \\ \propto \int_{-\infty}^{+\infty} \mathrm{d}\delta\omega_1 \int_{-\infty}^{+\infty} \mathrm{d}\delta\omega_3 \, R^{(3)}(t_3, t_2, t_1) &\cos(\delta\omega_1 t_1) \cos(\delta\omega_3 t_3), \\ &\propto p(\, \delta\omega_3, t_2 | \delta\omega_1, 0\,). \end{aligned} \tag{4.6}$$

Note that this relation is exact only in the slow modulation limit.

All quantities that describe the shape of the 2D-IR spectra (ellipticities[122,123], center-line slope[17,168,169], nodal-slope[170] and phase-slope[123]) are based on this picture (Eq. 4.6). As a result, many the quantities are proportional to $c_2(t)$ in the inhomogeneous limit, and all are unable directly to extract information on dynamics which are in the motional narrowing limit,

though of course that can be recaptured from the total linewidth of the transition. Where these methods differ is in their sensitivity to artifacts and numerical errors[17,122,123,168,169].

Kubo lineshape theory gives a framework to go beyond the limit of inhomogeneous broadening and is a more general description of frequency fluctuations and dephasing on an arbitrary timescale. Essentially, the response functions are expanded in terms of their cumulants, which are truncated at second order. For example, for linear spectroscopy,

$$R^{(1)}(t) \propto e^{-g(t)} = \left\langle \exp\left(-i \int_0^t \delta\omega(\tau) \mathrm{d}\tau \right) \right\rangle = \\ 1 - i \int_0^t \langle \delta\omega(\tau) \rangle \mathrm{d}\tau - \frac{1}{2} \int_0^t \mathrm{d}\tau' \int_0^t \langle \delta\omega(\tau') \delta\omega(\tau'') \rangle \mathrm{d}\tau'' + ... \tag{4.7}$$

The zeroth-order term is a constant, and the first term is an time average of frequency fluctuation, which vanishes by construct. Hence, the leading term is the second-order term. For a Gaussian distribution of frequencies, all higher order terms are zero, leaving the second-order term an exact solution. The function $g(t)$, which is itself dependent only on the FFCF, $\langle \delta\omega(\tau') \delta\omega(\tau'') \rangle$, completely determines the lineshape. This analysis generalizes to higher orders of spectroscopy.

This lineshape theory provides an alternate route to characterize 2D-IR spectra. Spectra can be calculated based on an assumed FFCF, and the parameters of the FFCF can be optimized to give the best agreement with the experiment.

In summary, the frequency-domain 2D-IR spectrum is approximately equal to the two-point joint probability distribution function of vibrational frequencies as a function of the population time t_2, which is carries the important information on molecular dynamics. In this report, we use several methods to quantitatively analyze our spectra and extract this correlation function, ellipticity, center-line-slope, and response function calculations, to ensure that the results are robust. The multiple methods are particularly needed in the analysis of the effect of the counter-cation (Section 4.5.2).

4.4 EXPERIMENTAL AND DATA-REDUCTION METHODS

The ionic liquids were purchased from Ioli-tec. Except for the water-containing sample, sample storage, mixing, and spectroscopic cell assembly were performed in a nitrogen atmosphere glovebox, with H_2O concentration below 5 ppm. Spectroscopic measurements were performed under a dry N_2g purged environment.

For dry samples, mixtures of $[C_4C_1im][SCN]$ or KSCN in either $[C_4C_1im][NTf_2]$ or $[C_4C_1C_1^2im][NTf_2]$ were prepared and stirred overnight. Spectroscopic cells consisted of 1 μL of ionic liquid held between two 2 mm thick calcium fluoride windows which were separated by a 100 μm O-ring Teflon spacer. Water content was monitored before and after the 2D-IR experiments by FTIR spectroscopy, and water content was estimated to be less than 150 ppm for all samples. For water-containing samples, the mixing of water and ionic liquid is performed in ambient condition, and stirred overnight. The sample cell is assembled with the same procedure under ambient condition.

For the 2D-IR experiment, $\sim$120 fs pulses of 800 nm wavelength were generated by a commercial Ti:Sapphire chirped pulse amplifier of 1 mJ at a repetition rate of 5 kHz. An optical parametric amplifier (OPA)[88] generated $\sim$2 μJ tunable mid-IR pulses of sub 100 fs duration, centered at 2050 cm^{-1}, with a bandwidth of 250 cm^{-1}. For the 2D measurements we used a Fourier transform 2D-IR setup in the pump-probe geometry as described by Helbing *et al*[89] (essentially identical to that report, except the repetition rate is 5 kHz). The data acquisition was performed with a fast-scanning routine without phase ambiguity. We performed the measurements in the all parallel polarization geometry.

The change in shape of the 2D-IR spectra over population time was quantified by ellipticities[122,123] and center-line slope[17,168,169]. Error bars in ellipticity are estimated by propagation of error in the fits of the two-dimensional Gaussians's parameters through the correlation function fitting. Similarly, error bars in center-line slope are calculated by propagating error through the peak maximum deterimation, the slope fit, and the correlation fitting. Global-fitting of the spectra to an assumed correlation function follows standard nonlinear response

function calculations using the Condon and second-cumlant expansion approximations[1]. Error bars are calculated by bootstrap analysis[171], in which the fitting is repeated on 100 synthetic data sets composed of a random selection of the original data points taken with replacement. The distribution of fitting parameters so obtained provides the error estimate.

4.5 RESULTS

4.5.1 Water Concentration

In order to test the effect of water, we compare 30 mM of $[C_4C_1im][SCN]$ in dry and water-saturated $[C_4C_1C_1^2im][NTf_2]$. The symmetric and antisymmetric modes of water ~ 3560 cm^{-1} and ~ 3640 cm^{-1}, respectively, clearly demonstrate the presence of isolated water molecules in the wet ionic liquid (Figure 10). The separation of symmetric and antisymmetric modes of water indicates that the water molecules are mostly isolated in ionic liquid[172–174]. The broad shoulder around ~ 3450 cm^{-1}, on the other hand, indicates hydrogen-bonded water molecules.

The dissolved water interacts with the $[SCN]^-$ vibrational probe, as the breadth of the C≡N stretch demonstrates. The C≡N stretch occurs at ~ 2050 cm^{-1} in both wet and dry samples. In the dry sample, the fullwidth at half maximum (FWHM) of the C≡N stretch is 20.5 cm^{-1}, while in the wet sample it is 26.1 cm^{-1}. What the FTIR cannot reveal is the nature of the interaction between the water and the $[SCN]^-$.

The 2D-IR spectra of $[SCN]^-$ in $[C_4C_1C_1^2im][NTf_2]$ with different water concentrations, on the other hand, allow us to identify to two subensembles of $[SCN]^-$ molecules, those with water in the first solvation shell and those without. The dry samples give characteristic features of isolated $[SCN]^-$ (Figure 11a). In the $t_2 = 0.2$ ps spectra, the 0 to 1 and 1 to 2 lobes are stretched along the diagonal axis with an inhomogeneous linewidth of 16.3 ± 0.2 cm^{-1} and a homogeneous width of 6.8 ± 0.2 cm^{-1}. The two lobes are separated by an anharmonicity

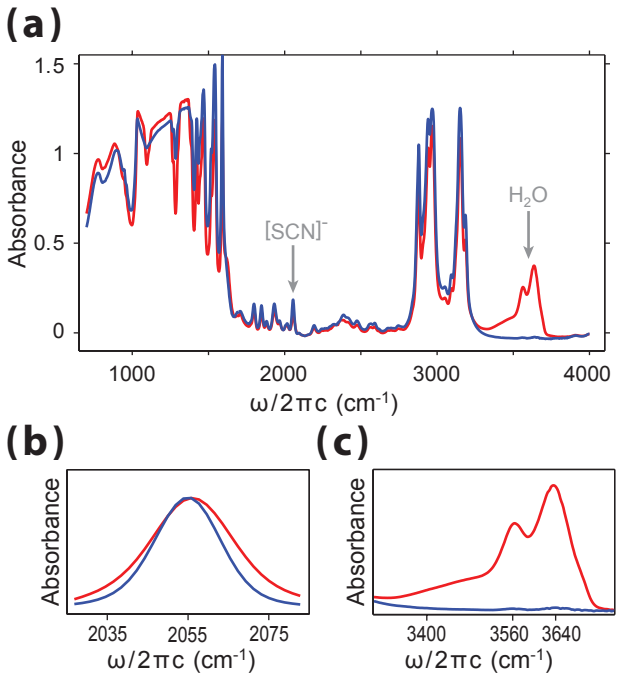

Figure 10: (a) 30 mM $[C_4C_1im][SCN]$ in dry $[C_4C_1C_1^2im][NTf_2]$ (blue) and in water saturated (red); (b) the change of the full-width at half-maximum of the CN stretch indicates that SCN interacts with the water in solution; (c) the OH stretching region shows both free and hydrogen bonded water.

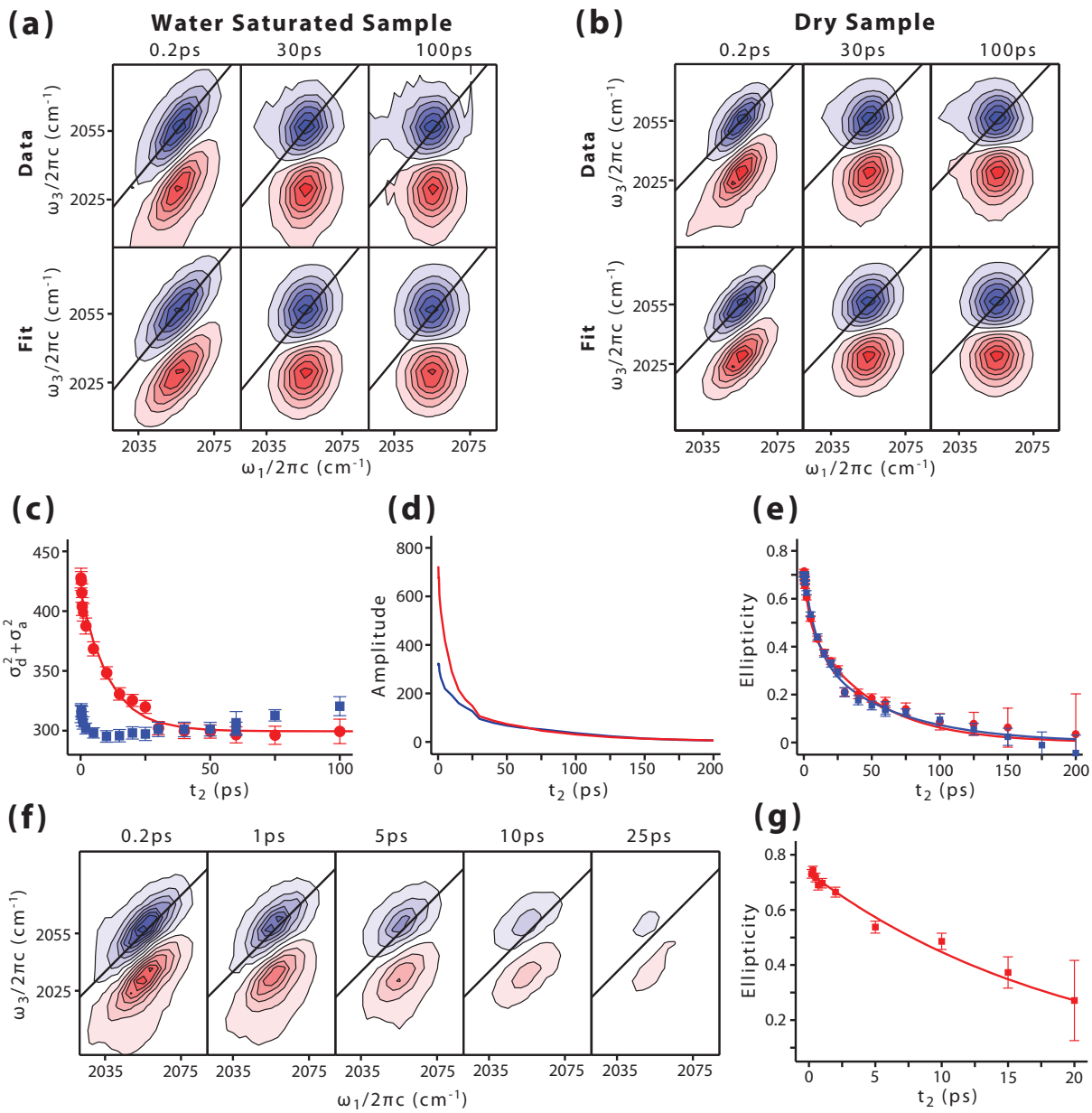

Figure 11: (a) 2D-IR of 30 mM $[C_4C_1im][SCN]$ in dry $[C_4C_1C_1^2im][NTf_2]$; (b) 2D-IR of 30 mM $[C_4C_1im][SCN]$ in water saturated $[C_4C_1C_1^2im][NTf_2]$; (c) the sum of square diagonal and antidiagonal widths is contstant for the dry sample but decreases for the water saturated sample; (d) the amplitude of the 0-1 peak for dry (red) and wet (blue) samples shows the faster signal decay of the wet component; (e) the ellipticity of SCN^- changes similarly over time for both systems of dry sample (red) and water saturated sample (blue); (f) the difference of water saturated and dry 2D-IR spectra give the 2D-IR signal from the subensemble of SCN^{-1} interacting with water; (g) the ellipticity of SCN^- interacting with water changes over time.

of 27.0 ± 0.2 cm^{-1}. Spectra at long waiting times show rounder features due to spectral diffusion. At 100 ps, the diagonal width of the dry sample has decreased to 13.2 ± 0.3 cm^{-1}, and the antidiagonal width has increased to 12.0 ± 0.2 cm$^{-}1$. By 200 ps, the correlation is completely lost. The ellipticities change in a biexponential fashion,

$$c_2(t) = A \exp\left(-\frac{t}{\tau_1}\right) + B \exp\left(-\frac{t}{\tau_2}\right), \tag{4.8}$$

For the dry sample, the dominant structural relaxation occurs on a tens of picoseconds timescale (45 ± 8 ps, $B = 0.47 \pm 0.09$). A smaller component of structural relaxation occurs on a few picosecond timescale (4.0 ± 0.6 ps, $A = 0.20 \pm 0.13$). The ellipticity goes to 0 within our experimentally accessible time window.

The water saturated sample has some features of the dry sample but displays new features in addition. We argue that these new features are due to a subensemble of $[SCN]^-$ molecules that interact with water. This "wet" sub-ensemble has a total linewidth, population relaxation rate, and structural relaxation rate that is different from the dry sub-ensemble. The 2D peaks of the water saturated sample start broader than the dry sample, but at long times are very similar in shape. At early times the widths of the 2D spectra are $\sigma_d = 19.1 \pm 0.2$ cm^{-1} and $\sigma_a = 7.8 \pm 0.2$ cm^{-1}, while at long times the widths are $\sigma_d = 12.7 \pm 0.3$ cm^{-1} and $\sigma_a = 11.7 \pm 0.3$ cm^{-1}. We quantify the change in total linewidth using the sum of squares of diagonal and antidiagonal linewidths $\sigma_{\text{total}} = \sigma_d^2 + \sigma_a^2$. This quantity should be conserved for any simple system, as it is for the dry sample (Figure 11, c). For the wet sample, however, this metric decreases over the first few picoseconds and then remains constant at the same value as the dry sample. Similarly, the total signal amplitude also demonstrates a rapid decrease over the first few picoseconds followed by relaxation over the 100 ps timescale which is identical to the dry sample(Figure 11, d).

Based on these two factors we assign the rapid decay due to fast vibrational relaxation of $[SCN]^-$ molecules with a water in their first solvation shell. The 11 ± 3 ps decay we see is in between these limiting extremes of vibrational relaxation rates of $[SCN]^-$ in dry $[C_4C_1im][NTf_2]$ ($T_1 > 70$ ps for $[C_4C_1C_1^2im][BF_4]$[119]), and $T_1 = 2.8 \sim 3.1$ ps in neat water[160]. Vibrational energy relaxation rates are, in general, very difficult to calculate accurately[175],

but the essential physical picture is that the forces on a molecule couple its vibrations to the environment, allowing energy to leak out[176–178]. The rate of leakage is proportional to the fourier transform of the force autocorrelation function, which can be written as a frequency dependent friction. With this as a qualitative picture, we argue that the strong change in vibrational relaxation rate due to water is likely to be a short ranged effect of water in the first solvation shell and not a long range interaction because water far from the $[SCN]^-$ probe should change neither the instantaneous forces on the $[SCN]^-$ nor the local density of acceptor modes in the 2000 cm^{-1} range noticably.

An alternate hypothesis is that orientational relaxation causes the difference in signal amplitude and lineshape. We argue that, however this is not the case. Our measurements are conducted in the all parallel polarization, so the signal amplitude contains both population and orientational relaxation rates. Note that orientational relaxation in these ionic liquids has been shown to occur on a $\sim$ 100 ps timescale[119], so we expect orientational relaxation is not responsible for the $\sim$ 5 ps signal loss that we observe for the spectra of the wet samples. In addition, though orientational relaxation and frequency relaxation can be correlated, which results in complicated effects on 2D spectra[16,179,180], usually this correlation causes a frequency dependent rotational anisotropy, quite a subtle change. The change in σ_{total} that we observe is much more dramatic than anything assigned to this kind of correlation of frequency- and orientational-relaxation. Based on this reasoning, we assign the change in lineshape to disparate rates of population relaxation of two subensembles rather than differences in orientational relaxation or orientationl-frequency correlation, though we cannot completely rule out that some orientational component is present in our extracted time-constants.

The total ellipticity of the wet and dry samples agree quantitatively (Figure 11,e). After the first picoseconds, it is clear what is happening. The remaining signal is due to the dry subsensemble of $[SCN]^-$ molecules, which is identical to the dry sample. The timescales of the long-lived components of both systems agree with each other within experimental error, indicating that the structural reorganization rates are identical and uninfluenced by the presence of water, at least on the few hundred picoseconds that we can resolve. At longer

times and on longer length-scales, the presence of water, which for example decreases the viscosity. The water concentration is ∼0.3 mol/L, or ∼0.1 mole fraction, which is relatively high and could reasonably be expected to impact the dynamics. Canongia Lopes et al[162] measured the macroscopic viscosity of $[C_4C_1im][NTf_2]$ as a function of water mole fraction, and 37.2 cP was found at a mole fraction of 0.1253, which significantly varies from 50.4 cP for dry samples.

The structure and dynamics of the wet ensemble are different from the dry ensemble. In the wet ensemble the overall linewidth is larger (both inhomogeneous linewidth $\Delta = 20.0 \pm 0.4$ cm^{-1} and homogeneous $1/(\pi T_2) = 7.6 \pm 0.2$ cm^{-1}); the signal amplitude decays faster, most likely because the vibrational relaxation time (T_1) is shorter though we cannot rule out faster orientational relaxation. At the same time, we do not oberserve a quantitative difference in the ellipticity at early population times ($t_2 < 5$ ps), even though the water saturated sample is is a complicated average of wet at dry subensembles.

To try to isolate the spectral diffusion of the wet ensemble, we subtracted the 2D-IR spectra of the dry samples from the 2D-IR of the wet samples. This approach is based on the following assumptions – that the dry ensemble in the water saturated sample has dynamics identical to the dry sample and that interconversion between wet and dry ensembles occurs more slowly than the signal of the dry sample (∼ 100 ps). This assumption is reasonable given the additive nature of the signal amplitude (Figure 11).

The subtracted 2D spectra are then fit to ellipticity to extract the dynamics (Figure 11). Spectral diffusion is observed within 20 ps time window, indicating the timescale of dynamics is comparable to our experimental time window. The ellipticity does not reach 0 before the signal is too weak to detect. A single exponential function gives a reasonable fit to the ellipticity data, yielding a timescale of 20 ± 5 ps. However, it is hard to further interpret this time constant because: (1) the limited time range is not enough for an unambiguous fitting (2) the long waiting time behavior cannot be obtained, which makes it hard to compare with other data we have; (3) the time constant may be an summation of different motions, including both rattling in ion-cage and ion-cage breakage. Nevertheless, the FFCF drops

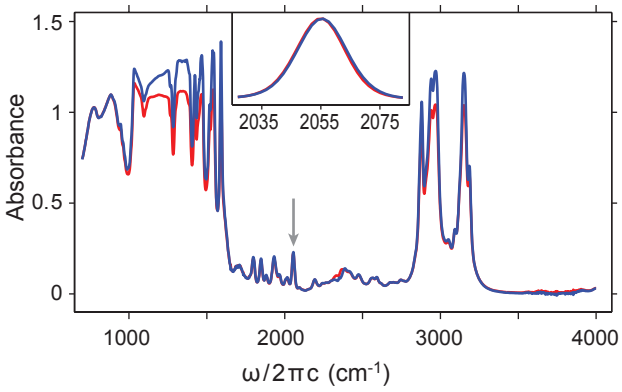

Figure 12: FTIR spectroscopy of 30 mM $[C_4C_1im][SCN]$ in $[C_4C_1C_1^2im][NTf_2]$ (red) and 30 mM KSCN in $[C_4C_1C_1^2im][NTf_2]$ (blue). (inset) the C≡N stretch of SCN^- shows negligible difference.

from ~ 0.75 to ~ 0.25 in first 20 ps, which is similar to the dry subensemble.

In summary, 2D-IR experiments with C≡N stretch of $[SCN]^-$ in water-saturated $[C_4C_1C_1^2im][NTf_2]$ resolve two sub-ensembles of $[SCN]^-$ anions with very different dynamics. One resembles $[SCN]^-$ in the dry environment, with very similar population relaxation and spectral diffusion rate. The other one has broader homogeneous and inhomogeneous width, and has a much faster population relaxation rate, and we assign this sub-ensemble to $[SCN]^-$ ions with a water molecule in their first solvation shell.

4.5.2 Counter-Ion

30 mM of of KSCN dissolved in $[C_4C_1C_1^2im][NTf_2]$ is compared with 30 mM of $[C_4C_1im][SCN]$ dissolved in $[C_4C_1C_1^2im][NTf_2]$. FTIR spectrum of the C≡N stretch shows very minor shift of central frequency of less than 1 cm^{-1}.

The KSCN system, at early population times, shows good agreement with the $[C_4C_1im]$ [SCN]. The inhomogeneous and homogeneous width each equal to 16.8 ± 0.2 ps and $6.6 \pm$

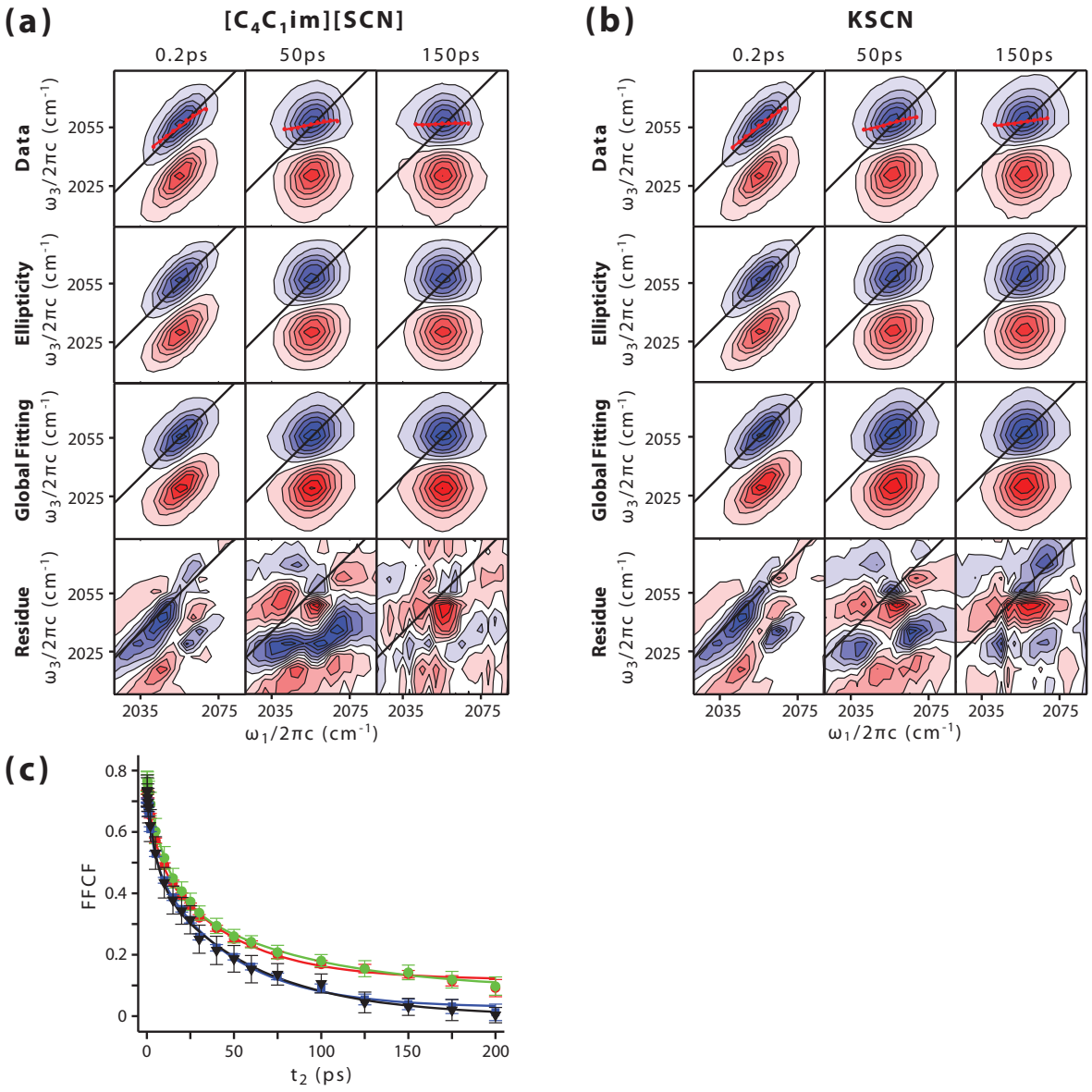

Figure 13: 2D-IR spectroscopy of a) 30 mM $[C_4C_1im][SCN]$ in $[C_4C_1C_1^2im][NTf_2]$, the first row shows the experimental data and CLS fitting result; the second row shows the fitted two-dimensional Gaussian for ellipticity method; the third row is the calculated spectra from Kubo lineshape theory; the last row shows the difference between the third and first row. b) 30 mM KSCN in $[C_4C_1C_1^2im][NTf_2]$. c) The change in ellipticity and CLS as a function of time shows long-time motion exists in KSCN system (red and green) but not in $[C_4C_1im][SCN]$ system (blue and black).

0.1 ps, and the anharmonicity is 26.5 ± 0.2 cm^{-1}. As the system evolves, However, a small but clear tilt remains even at 100 ps. By fitting the ellipticities, such tilt gives a significant offset of 0.12 ± 0.02. The FFCF fitting with bi-exponential functions gives two timescales, one is 11 ± 2 ps, and the the other is 130 ± 30 ps. The timescales come with errorbars that are significantly larger than previous experiments, and the curve of the bi-exponential fails to catch the static component of the ellipticity. To fix this problem, a bi-exponential with a constant is employed to fit this outcome.

$$c_2(t) = A \exp\left(-\frac{t}{\tau_1}\right) + B \exp\left(-\frac{t}{\tau_2}\right) + C, \tag{4.9}$$

The component, C, is, of course, not truly static but rather corresponds to dynamical processes happening on a longer than $\sim$ 200 ps timescale, which we cannot fully resolve. The fitting resolves a constant of $C = 0.1$, with the second timescale almost unchanged compared to [C_4C_1im][SCN] (Table 1). The shorter timescale of the KSCN is slightly longer than that of the [C_4C_1im][SCN]. The amplitude of the longer timescale in the KSCN case is smaller than that in [C_4C_1im][SCN] case, and the difference is compensated by the offset.

To ensure that the correlation function extracted by the ellipticity is not dominated by a systematic error, we also performed an analysis of the center-line-slope (CLS) (Figure 13, top row). The values of the FFCF based on CLS (Figure 13, c green and black) agree with the ellipticity (red and blue) within the esimated error for all data points. Fitting the CLS to Eq. 4.9 gives similar results (the confidence intervals overlap) though the best fit does slightly longer A and B time-constants for KSCN than [C_4C_1im][SCN]. The largest deviations are the second time-scale, $\tau_2 = 80 \pm 20$ ps and the amplitude of the static component $C = 0.08 \pm 0.02$.

This level of disagreement is perhaps surprising given the excellent agreement in the data points (Figure 13). We attribute the difference to the sensitivity of the fit to differences in the statistical weights of each of the points, which are quite different in the ellipticity and CLS methods. Weighting the points differently biases the fits to better reproduce different regions and causes the observed variation. As such, we take the variation between methods to be a more reliable estimator of the true range than the statistical 95% confidence intervals.

Table 1: Time constants as a function of counter-cation

	Ellipticity	CLS	Global Fitting
$[C_4C_1im][SCN]$			
τ_1(ps)	4.0 ± 1.2	5.2 ± 2.0	4.9 ± 2.0
τ_2(ps)	45 ± 8	58 ± 13	60 ± 7
A	0.19 ± 0.02	0.28 ± 0.06	0.18 ± 0.05
B	0.49 ± 0.02	0.46 ± 0.05	0.82 ± 0.05
KSCN			
τ_1(ps)	5.5 ± 1.5	11 ± 3	6.1 ± 3.5
τ_2(ps)	45 ± 8	77 ± 21	62 ± 24
A	0.21 ± 0.05	0.34 ± 0.05	0.20 ± 0.10
B	0.41 ± 0.03	0.34 ± 0.04	0.68 ± 0.07
C	0.12 ± 0.02	0.09 ± 0.03	0.13 ± 0.06

Nevertheless, the picture that the K^+ counter-ion induces some much slower dynamical process is robustly reproduced in the CLS analysis.

As a final consistency check, the experimental spectra are globally fit to simulated spectra based on Kubo lineshape theory (Section 4.3) and the correlation function parameters are optimized to minimize the square error between experiment and calculation (Figure 13 a,b lower). A bootstrap analysis (Supplemental Information) clearly shows that the amplitudes and time-constants of the second exponential and the static component are highly correlated, but nevertheless, a dynamical process of > 200 ps is needed to reproduce the shape of the long time spectra.

The small residual tilt of the $t_2 = 200$ ps 2D spectrum of KSCN indicates a long-lived correlation between the initial and the final frequencies of the chromophore, which is affected by the immediate surroundings of the probe molecule. A new equilibrium that can form a distribution in frequencies is required, and the rate for the interchange between species in the equilibrium needs to be low.

The KSCN sample and the $[C_4C_1im][SCN]$ sample only differ in the choice of cation. Therefore, it is reasonable to hypothesize that the long-lived correlation comes from the interaction between the potassium and $[SCN]^-$. Wipff et al.[165] have shown that sodium chloride prefers to form ion pairs or clusters in $[C_4C_1im][NTf_2]$, and KSCN behave similarly in $[C_4C_1C_1^2im][NTf_2]$. Since the timescales are nearly unchanged, it is not likely that the KSCN forms clusters, because that would greatly change the dynamics of the $[SCN]^-$ ion. Therefore, the long-lived correlation suggests ion pair formation between potassium and thiocyanate. One possibility for this equilibrium is between the KSCN ion pair and the free $[SCN]^-$ ion. Another possibility is that the equilibrium exists between different configurations of ion pairs, which would most likely be the K^+ is on either side of the SCN anion, namely KSCN and KNCS. With our current data, however, it is not possible to distinguish conclusively whether the slow equilibrium we observe is between free and ion-paired or two configurations of the KSCN. Given the low concentrations involved and the intermediate polarity of the ionic liquid solvent, we find the equilibrium between free and bound to be the most likely.

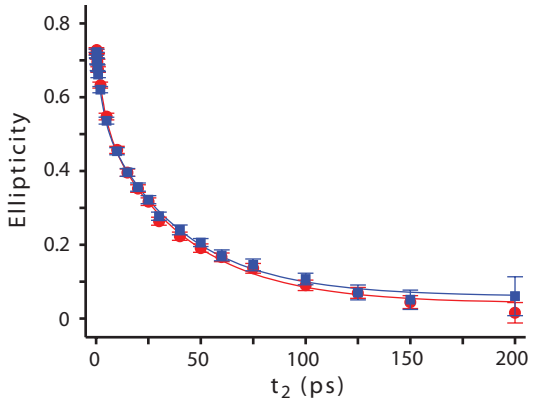

Figure 14: The ellipticity changes similarly over time for both systems of 10 mM SCN^- (red) and 60 mM SCN^-.

No matter which of the two hypotheses is correct, the rate of ion pair reorganization must be slower than ~ 200 ps.

The alternative hypothesis is that the 30 mM K^+ changes the viscosity uniformly which in turn slows down the dynamics. The ratio of timescales would require a viscosity change by a factor of > 3, which is not observed.

4.5.3 Solute Concentration

To establish SCN^- as a good local probe, it is also important to rule out the clustering of SCN^- ions in solution.

The structures and the dynamics around $[SCN]^-$ (as reported by the CN stretch) are concentration independent over the range of 15 mM and 60 mM. The two different solute concentrations were prepared in $[C_4C_1C_1^2im][NTf_2]$. The peak position and shape in FTIR spectra do not change appreciably over this range (data not shown), which is consistent with ideal mixing in which the $[SCN]^-$ local environment is dictated by the majority ionic liquid and not by other $[SCN]^-$ solutes. Furthermore, 2D-IR experiments also show identical

spectral diffusion (Figure 14), which indicates a negligible change in the dynamics upon changing the solute concentration.

This result is non-trivial. Computational studies have revealed structural changes for the mixture of $[C_4C_1im][Cl]$ and $[C_4C_1im][SCN]$ compared to neat $[C_4C_1im][SCN]$[121]. The anions coordinate to the most acidic hydrogen atoms available in the system correlates with its size and basicity. This results in that the chloride ion is capable of displacing the $[SCN]^-$ ion from its preferred coordination sites around the $[C_4C_1im]$ cation, which would cast a non-ideal influence on the dynamics of $[SCN]^-$ ion. In our system, $[NTf_2]$ is the only anion that may potentially affect the dynamics of the $[SCN]^-$, and no such result has been observed. The result is reasonable because $[NTf_2]$ anion, unlike chloride, is less basic and bigger than $[SCN]^-$, therefore it is not likely to out compete $[SCN]^-$ and affect its dynamics.

In summary, the solution can be considered as ideal mixing within the concentration range, and the distribution of $[SCN]^-$ around cations is not affected by the solvent anion. Our data on the dynamics of the solute is more likely reflecting the properties of the pure ionic liquids.

4.6 DISCUSSION

4.6.1 SCN^- is a good local probe of ionic liquid dynamics

These results, taken together, indicate that vibrational spectroscopy of the C≡N stretch of $[SCN]^-$ is sensitive to the structure and dynamics in the ionic liquid over about one solvation shell. Several pieces of evidence point us to this conclusion.

First, in the water-saturated samples, the water concentration is estimated to be ∼0.3 mol/L from FTIR data by assuming a extinction coefficient of 100 $M^{-1}cm^{-1}$. This is a significant amount compared to the neat $[C_4C_1C_1^2im][NTf_2]$ concentration ∼3 mol/L. Since most water molecules are isolated in the ionic liquid, the probability for a $[SCN]^-$ anion

to have water molecule in its first couple of solvation shells is significant. We observe two dynamically different sub-ensembles, which we interpret as $[SCN]^-$ with or without a water molecule in the first solvation shell. If, on the other hand, $[SCN]^-$ were sensitive to more than one solvation shell, the 2D-IR should have a more continuous distribution of spectral diffusion rates based on the number of nearby water molecules, rather than the distinctly bimodal dynamics that we observe.

Second, in the KSCN experiment, merely changing the counter-ion leads to a significant change in the rate of spectral diffusion. The addition of the K^+ ion causes a frequency correlation which lasts hundred of picoseconds. If $[SCN]^-$ anion were sensitive to a large volume, it would give out a more averaged response. If that was the case, an addition of potassium ion in its surronding would not change the spectral diffusion much, since the fraction of response originating from potassium ion would be averaged out by other ions. In our experiment, however, the opposite is observed, indicating $[SCN]^-$ is sensitive to very few ions nearby, and an extra potassium is able to change the spectral diffusion signifantly.

Third, it is important to show that the local details of the solvent dynamics are not overwhelmed by ion clustering inherent to the $[SCN]^-$. $[SCN]^-$ ions in water and other solvents have shown this tendency[4,6]. For ionic liquids, this kind of non-ideal mixing of two or more ionic liquids has lead them to be dubbed "double salt ionic liquids", for example[164].

To rule out the possibility that the clustering of $[SCN]^-$ dominates our observations, we confirmed that the dynamics reported by the $[SCN]^-$ are independent of concentration over the 10–60 mM range. This rules out both the direct clustering of $[SCN]^-$ as well as indirect interactions such as perturbing the dynamics of the nearby ionic liquid.

Based on these arguments, we conclude that the vibrational frequency of the C≡N stretch in $[SCN]^-$ is a very local probe of dynamics in the ionic liquids and is sensitive to the species in its immediate solvation shell. This fact is important to establish because it allows us to construct local, molecular explanations of the dynamics that we observe as we use vibrational probes such as $[SCN]^-$ to interrogate other properties of these ionic liquids.

4.6.2 Water induced dynamical heterogeneity

Structural heterogeneity is another signature of complexity in ionic liquids. Numerous experimental[112,140,181,182] and theoretical[104,183,184] works have demonstrated that ionic liquids tend to separate into polar domains dominated by the charged cations and anions and non-polar domains dominated by the fatty alkyl chains. From early on, the potential of molecular cosolvents to affect the structure and dynamics in ionic liquids was recognized.

Our experiment provides a new experimental route to extract how molecular cosolvents can change the dynamics of an ionic liquid by probing the spectral diffusion of the anion. This point of view is complimentary to probing the effect of the ionic liquid on the molecular solvent, for example, water[173,174]. Together, the two approaches can provide a vivid picture of how the molecular cosolvents and ionic liquids affect each other. The specific molecular observables these experiments provide will be valuable for bench-marking molecular models such as molecular dynamics simulations[117,162,174,185].

A rigorously dry ionic liquid is consistent with a homogeneous fluid from the point of view of the $[SCN]^-$ dynamics. In the presence of water, however, we observe two distinct environments for the $[SCN]^-$, characterized by different homogeneous linewidths, inhomogeneous linewidths, and population relaxation rates. The dry sub-ensemble is identical to the the neat ionic liquid, whereas the $[SCN]^-$ in the wet sub-ensemble is more strongly coupled to its local environment. The size of the frequency fluctuations that we observe is larger and the rate of popluation relaxation is higher.

From our results, we can set a $\sim$ 100 ps lower limit on the exchange rate between the two environments. This estimate is based on the fact that the spectral diffusion rate and the population relaxation rate are identical to the ones that we measured in the dry environment. If the wet and dry subensembles exchanged on a time comparable to our experimentally accessible time window, both the population decay and the spectral diffusion of the dry ensemble would be distorted by this new relaxation channel.

In fact, such dynamic heterogeneity that we observe is very similar to the so-called

"red edge effect" (REE) in ionic liquids reported by Samanta and coworkers[186,187]. In their work of using time-dependent fluorescence of 2-amino-7-nitrofluorene in $[C_4C_1im][PF_6]$, the fluorescence spectrum of the chromophore is excitation-wavelength dependent. This phenomenon happens if the solvent relaxation time is longer than its fluorescence lifetime: In most molecular liquids, where the solvent molecules adjust to the change in dipole moment of the probe much faster than the fluorescence timescale of the probe, the emission is from a locally relaxed state and no REE is observed; on the other hand, if the solvent molecules reorganize themselves slowly, and fluorescence happens before the solvent molecules completely reorganize, then the emission is from a locally excited state and REE occurs. From a molecular dynamics study, Margulis *et al.* found that the solute-solvent electrostatic energy is trajectory dependent but almost time-independent, indicating a property of slow dynamics of solvents, and the probes are trapped in local environments[144]. In this sense what we have seen in our experiment is highly similar to REE effect, where $[SCN]^-$ are trapped inside quasistatic solvent cages, and a sub-ensemble of them has a water molecule in the first solvation shell. The two sub-ensembles of $[SCN]^-$ can move freely in local environment (spectral diffusion), but the change between different sub-ensemble cannot occur within experimental time window.

Though our 2D results strongly indicate dynamical heterogeneity, an even more rigorous test would be three-dimensional infrared spectroscopy (3D-IR)[33,188,189]. Fifth-order experiments such as 3D-IR and multiple population time spectroscopy (MUPPETS)[113,190], are able to fully explore the higher order frequency and population correlation functions which indisputably indicate heterogeneous dynamics. 3D-IR has detected heterogeneity in liquid water on the ~ 0.5 ps timescale[33] and non-Markovian chemical exchange[189]. Both of these experiments required detailed analysis of subtle changes in the 3D lineshape. Wet ionic liquids may be an ideal system for even clearer demonstrations of the spectroscopy because of the longer population relaxation rates of $[SCN]^-$, the 100 ps timescale on which the heterogeneity seems to persist, and the large variation of the population relaxation rate and lineshape between the two sub-ensembles.

Nevertheless, this is a rich area to explore with 2D-IR spectroscopy. Three potential areas

for future exploration of the effect of water are viscosity, phase behavior, and ionic liquid function. Viscosity we have related to the ion-cage lifetime of the ionic liquid, and water changes the ion-cage lifetime. Future studies may help to understand more comprehensively how this molecular change dictates the bulk viscosity by varying the water content and correlating it to the change in viscosity. The phase behavior of some hydrophilic ionic liquids as a function of water content is particularly dramatic, but the molecular origins are as of yet unclear. For example, the self-diffusion coefficient of ions in $[C_4C_1im][CH_3COO]$ is constant until about 70% water concentration, at which point a sharp change occurs[191]. Other ionic liquids show lower critical solution temperatures, in which an increase in temperature causes demixing of the ionic liquid and water[192]. Our experiment could provide a direct way to probe how water affects the local structure and dynamics of these ionic liquid as a function of composition. Finally, water can impact the functional behavior of task-specific ionic liquids for CO_2 capture[193,194] as well as bio-mass processing[195,196].

4.6.3 Solute Ion-pair formation

The concept of ionicity is an important one in the understanding of bulk transport phenomena. The two experimental markers of ionicity come from the interpretation of the Walden plot[197,198] and the comparison of NMR and conductivity derived self-diffusion coefficients[126]. The mobilities extracted from the NMR measurments are higher than the mobilities extracted from conductivity measurements, suggesting a simple picture in which oppositely charged ions sometimes diffuse together. The experiments are robust, but the molecular interpretation is debated. At one extreme, some experiments suggest that ion-pairs compose more than 99%[127] of the species in solution, whereas numerous theoretical studies and molecular simulations posit that no long-lived pairing at all is needed to explain the anomalous transport properties[103,128,143,149,199,200].

The fundamental difficulty is that "an ion pair" is poorly defined in neat ionic liquids, since the ions are always surrounded by several counter ions. As pointed out by Kirchner *et al.*[40], though weakly defined in pure ILs, an ion pair of a salt dissolved in an ionic liquid is a

cleanly defined concept since the cation and anions of the solute can be distinguished from the solvent. By probing the ion pairing as a function of the solute ions, one might be able to extrapolate to the ionic liquid itself. Some work in this direction exists.

On the one hand, the S_N2 reaction of trifluoromethanesulfonate and bis(trifluoromethanesulfonyl)imide salts of dimethyl-4-nitrophenylsulfonium shows no signs of ion pairing[201,202]. On the other hand, many salts take ion pairing to the extreme (*ie* a bulk ionic solid) and are completely insoluble[81].

Our experiment provides a direct comparison with Kosower's salt experiment done by Lui *et al.*[203]. Kosower's salt forms no ion-pairs in six different ionic liquids, including $[C_4C_1C_1^2im][NTf_2]$, which seems contradictory to what we observed here. But as they mentioned in their work, their results are based upon mixtures of salts composed of ions with similar properties such as the relative size, and mixtures of dissimilar salts may deviate from the ideal behavior. What we see is more likely to be the second case since KSCN is much smaller in size and much stronger in Coulmbic interaction compared with the ionic liquid solvent.

Charge density of the ions is an obviously important parameter. Smaller, more charged metal ions tend to be sparingly soluble whereas larger, softer ions are more soluble[81]. Kirchner *et al.*[40] investigated the effect of charge density on ions in ionic liquids with molecular dynamics simulations and found that varying the charge on the solute ions tuned the ion pairing behavior across the full range from no ion pairing to weak ion pairing to strong ion pairing.

We have now measured moderate and weak ion pairing. Our previous experiments with $[C_4C_1im][SCN]^-$ ion dissolved in $[C_4C_1im][NTf_2]$ and $[C_4C_1C_1^2im][NTf_2]$ represents the weak pairing limit. The ellipticities of the 2D-IR spectra went to 0 within 200 ps[129], inconsistent with long-lived ion pairs in this system. Our current work shows moderate ion pairing between the K^+ and $[SCN]^-$ ions. The ions seem to cluster in solution but not all $[SCN]^-$ are bound to a K^+. Based on the physical picture developed in this paper, future studies will be able to assess a wider range of counter-cations and provide a quantitative picture of

ion pairing in these ionic liquids.

4.7 CONCLUSION

In summary, we used thiocyanate ion dissolved in $[C_4C_1C_1^2im][NTf_2]$ as an sample system to prove that the C≡N of thiocyanate ion is a local probe for 2D-IR to determine the ultrafast structure and dynamics in the ionic liquid. By varying three different parameters of the system, which are water concentration, solute concentration and the choice of cation, different forms of heterogeneity have been detected. The experiment of $[SCN]^-$ in water-saturated ionic liquid resolves two sub-ensembles, one of which is dynamically identical to the dry condtion, while the other has broader inhomogenenous and homogeneous linewidth, as well as a very fast population decay. This result indicates that different $[SCN]^-$ anions are experiencing different local conditions, and we hypothesize that the latter is the case that $[SCN]^-$ has a water molecule in its first solvation shell. By changing the solute from $[C_4C_1im][SCN]$, which is a ionic liquid, to KSCN, which is an ordinary inorganic salt, we see a distribution of microstructures that cannot interchange with each other within a timescale of 100 ps, and is probably from the ion-pairs formed between thiocyanate ion and potassium ion. The spectral diffusion is invariant to changes in the solute concentration, which proves that the $[SCN]^-$ anions do not interact with each other and do not change the local dynamics of the ionic liquid.

5.0 THE STABILITY OF ION-PAIRS AND THE MICROSCOPIC STRUCTURE OF DIVALENT INORGANIC SALTS IN IONIC LIQUIDS

It has been shown in the previous chapter that the inorganic salt KSCN forms ion-pairs in the ionic liquids. This is counter-intuitive if we consider the "like dissolves like" rule. This observation therefore raises questions about the properties of those ion-pairs.

In this chapter, we will try to answer two questions about the solute ion-pair formation in ionic-liquids. The first question is the stability of the ion-pair. The second question is the how divalent inorganic salts are dissociated.

5.1 INTRODUCTION

Ion-pairing has long been an interesting idea in different realms of chemistry, and has been observed in a variety of different systems.[204–206]. The concept "ion-pair" is typically understood as a cation and anion pair that is held together by a strong coulombic force. Experimentally, ion-pairs behave differently from free ions in electrochemistry, kinetics, and thermodynamics[207]. The typical ion-pair lifetime is above 100 ps, and is believed to equilibrate with the free ions via dissociation[204,208].

Ion-pairing has been observed by a variety of different experiments. In the conductivity measurement that was first conducted by Fuoss and Krauss[209], the electrical conductivity of tetra-iso-amylammonium nitrate is smaller than expected. This is because macroscopically,

the ion-pair is charge-neutral, and therefore does not conduct electricity[210,211]. Ultrasonic / dielectric relaxation has also been used to study ion-pair formation[212,213]. Recently, there are also reports using X-ray wide-angle and small-angle scattering techniques to acquire detailed information about the radial distribution of ions[214]. Spectroscopic methods have proved useful in determining and characterizing the formation of ion-pairs. There were reports of ion-pair formation with UV-Vis spectroscopy[215,216], FTIR[217] and Raman spectroscopy[218,219]. Typically, the vibrational probe shifts its frequency upon forming ion-pair, which shows up on the spectrum as a new peak; the relative intensity could tell the relative amount of the ion-pair and the free ion if their individual oscillator strength are known. 2D-IR spectroscopy and pump-probe IR spectroscopy have also been applied to study the kinetics and reorientation dynamics of ion-pair systems[6,35–37].

Bjerrum was the first to mathematically define this concept[220]. An ion experiences two different effects in the solution: it is attracted by the Coulombic force to get closer to the counter-ion; the entropic effect favors random distribution in the solution and tend to separate the two ions. The summation of the two effects yields a minimum in radial probability distribution of the ion with respect to its counter-ion, and that minimum distance is defined as the maximum distance for a ion-pair

$$R = \frac{z_+ z_-}{2\epsilon k_B T}, \tag{5.1}$$

where z_+ and z_- each represent the charge of the cation and anion, respectively. ϵ is the dielectric constant of the solvent, and k_B is the Boltzmann constant, and T is the temperature of the system.

The ion pair concept then further developed with the finding of different types of ion-pairs[204,212,221]. Depending on the distance of the two counter-ions, the ion-pairs are generally categorized as three types: contact ion-pairs (CIP) are ion-pairs where the counter ions are in direct contact; solvent-shared ion-pairs are ion-pairs where the ions being separated by one water molecule; solvent-separated ion-pairs (2SIP) are ion-pairs that the ions being separated by two or more layers of water molecules. In water, all three types have been

observed by experimental methods, and in certain cases, the three types could co-exist in the same solution.

The concept "ion-pair" is not limited to mono-valent ions, but can also apply to all the ions of different charges. For di- or tri-valent salts, such as $CaCl_2$ or $FeCl_3$, the existence of ion-pairs could be complicated due to the fact that the salts could partially dissociate in solution[222–224]. Indeed, in the recent report on aqueous $LaCl_3$ solution, one Cl^- is found near the cation at 2.8 Å, while another Cl^- ion is present in the second solvation shell of $\sim$ 5 Å. Far-infrared studies of $FeCl_3$ and $FeCl_2$[225] show a non-linear concentration dependence of the absorption, indicating a progressive formation of contact ion-pair complexes between the iron and the chloride.

In the previous chapter, we have seen that KSCN does not fully dissociate in an ionic liquid, and the formation of solute ion-pairs has also been reported independently by Fayer and co-workers[226]. Naively, this finding is counter-intuitive because the ionic liquids are molten-salts, and their microscopic environment should be highly similar to the inorganic salts. The strong coulombic force provided by the local ion network should be able to stabilize the free ions, and the dissociation is then favored due to the net increase in entropy. Apparently, the presence of ion-pair in ionic liquids indicates that the microscopic environment of ionic liquids is significantly different from inorganic salts. This finding opens up a variety of new questions that related to the unique type of solvent.

In this chapter, we try to answer two fundamentally interesting questions about ion-pairs in ionic liquids:

The stability of the ion-pair: Kirchner *et al.* has predicted that the Gibbs free energy of ion-pair of NaCl in ionic liquid could be as high as 30kJ/mol[40,165]. The observation of ion-pairs of KSCN at a concentration of 30 mM qualitatively agrees with the estimation. It still needs a quantitative measure for the stability of the ion-pair in ionic liquids.

The two effects that determines the ion-pair in Bjerrum's definition represents the the interplay of enthalpy and entropy in ion-pair formation and dissociation[220]. The Coulombic attraction between the cation and the anion contributes to ion-pair via enthalpy; while at the

same time, the tendency of random distribution is the entropic contribution. The amount of thermal energy affects the dissociation process, and the thermal energy can be varied by changing the temperature. The relative partition, or the equilibrium constant of the two species as a function of temperature, can be used to determine the stability of the ion-pair. The logarithm of the equilibrium constant should be linearly proportional to the inverse temperature. The slope and the intercept of the line should each represent the enthalpy and the entropy of the dissociation process, respectively.

The KSCN and $[C_2C_1C_1^2im][NTf_2]$ system, however, is not suitable for the measurement because the KSCN peak is highly overlapping with the free ion peak, making it impossible to independently determine the concentration of each species for the spectra. In this chapter, we will show that a similar system, NaSCN in $[C_2C_1im][NTf_2]$ have different frequencies for the free ion and the ion-pair. At room-temperature, the ion-pair and free ion co-exist in the solution and can both be detected by FTIR spectroscopy. This system is therefore suitable for the determination of ion-pair stability.

The microscopic structure and dynamics of divalent salts in the ionic liquid. It is interesting to see if the divalent salts form ion-pairs, and if so, what their microscopic structures are. It is also a good comparison of dynamics with the mono-valent salts to see how the choice of salts could affect the stability of the local ion network. In this chapter, we will be testing the ionic forms of two similar divalent salts, the $Ca(SCN)_2$ and the $Ba(SCN)_2$.

5.2 RESULTS

5.2.1 The ion-pair formation of NaSCN in $[C_2C_1im][NTf_2]$

The 2D-IR spectra of 30 mM NaSCN in $[C_2C_1im][NTf_2]$ shows evidence of the coexistence for the ion-pair and free thiocyanate ion in solution (Figure 15). At short waiting times, the blue and the red peaks are elongated along the diagonal axis, and the central frequency is slightly

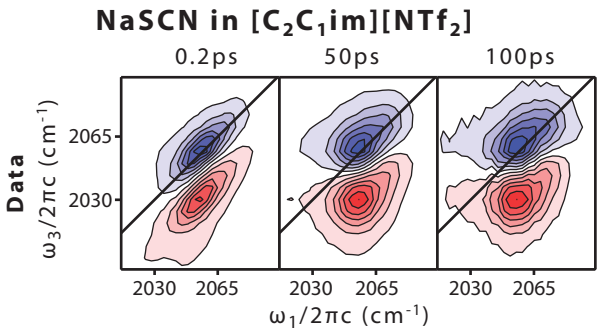

Figure 15: 2D-IR of NaSCN in $[C_2C_1im][NTf_2]$ shows a bean-shaped peak at long waiting times. This indicates that there are two sub-ensembles, one being the ion-pair, the other being the free ion.

shifted from the free SCN in $[C_2C_1im][NTf_2]$. At long waiting time, the peaks have changed their shape, but instead of adopting a smooth Gaussian shape, the peaks are distorted. At the higher wavenumber side, the contours are stretched toward the higher wavenumber, making the peak asymmetric. The biggest curvature of the peak around 2065cm^{-1}, and below that wavenumber, the peak looks like a regular Gaussian peak.

This observation provides the direct evidence of two partially overlapping sub-ensembles. There is one sub-ensemble of lower wavenumber at 2053 cm^{-1}, which is the same central frequency as the free SCN ion in $[C_2C_1im][NTf_2]$; there is another sub-ensemble of higher frequency at 2065 cm^{-1}, which is expected to be the NaSCN ion-pair. The free-ion peak and the ion-pair peak do not completely overlap, and the two species can both be detected independently. NaSCN is therefore capable of quantifying the equilibrium constant of the dissociation process. The temperature dependence of equilibrium constant can be used to calculate the thermodynamic quantities of the ion-pair.

There is no sign of cross-peaks between the two sub-ensembles within our experimental time window. This indicates that the equilibrium happens on a longer timescale than 200 ps, which is qualitatively consistent with the expectations from the ion-pair in water. The ionic liquid has a much higher viscosity than water, and the dynamics of solutes are slower than

in the water. All of these lead to the conclusion that we should not observe the dissociation process.

FTIR experiments at different temperatures could reveal the partitioning between the two sub-ensembles. From the spectra, we can see that as the temperature increases, the peak experiences a minor shift towards the red side. As the temperature increases, the peak of ion-pair, which is on the blue side, decreases in intensity, while the free ion peak increases. This is because the increasing temperature shifts the equilibrium between ion-pair and free ion shifts twoards the entropy-favored side, which is the free ion side.

The temperature-dependent FTIR can be fitted by two Gaussian functions to extract the amplitude of each sub-ensemble (figure 16). The first Gaussian is fixed at 2053 cm^{-1}, representing the free SCN ion sub-ensemble; the other Gaussian has central wavenumber of 2065 cm^{-1}, representing the NaSCN ion-pair sub-ensemble. The amplitude change of the two Gaussians follows the expected trend: as the temperature increases, the ion-pair sub-ensemble decreases while the free ion sub-ensemble increases. The two amplitudes are used to calculate the equilibrium constants of different temperatures. According to the Van't Hoff equation, the negative logarithm of equilibrium constant should be linearly proportional to the inversed temperature, with which the slope represents the enthalpy and the offset represents the entropy.

By plotting the resolved negative logarithm of equilibrium constant versus inverse temperature, we found that our experiment shows good linearity. By fitting the equation with linear function plus a constant, we found that the enthalpy of the dissociation process is $\Delta H = 9$ kJ/mol, while the entropy is $\Delta S = 6$J /mol·K, and the total Gibbs free energy is $\Delta G = 8$ kJ/mol.

5.2.2 The infrared spectra of divalent salt dissolved in $[C_2C_1im][NTf_2]$

We choose two different SCN-based divalent salts, namely $Ca(SCN)_2$ and $Ba(SCN)_2$ as our systems of study. The $[C_4C_1im][SCN]$ is used as the source of free SCN ion for comparison.

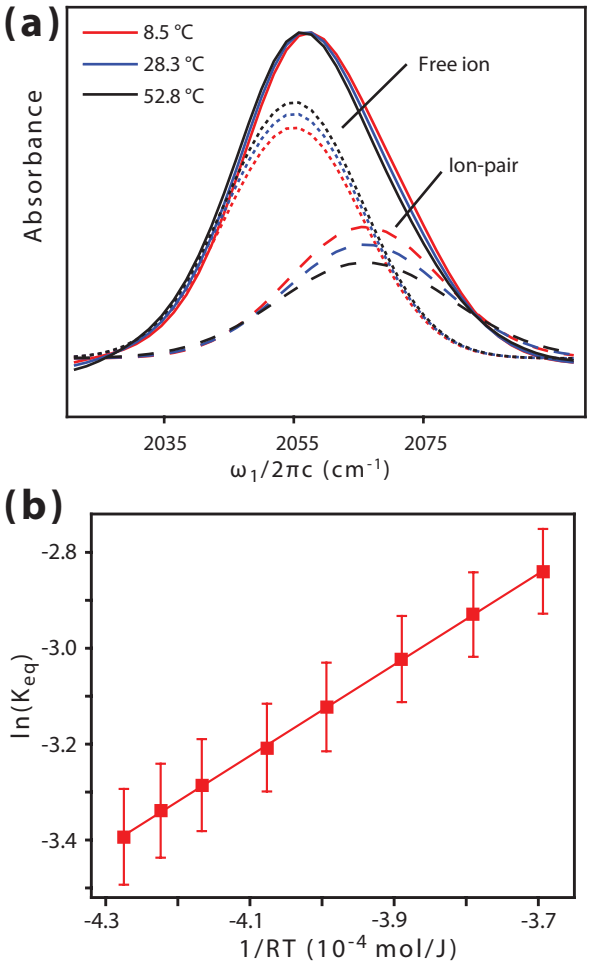

Figure 16: (a) The temperature-dependent FTIR data of the thiocyanate peak of NaSCN in $[C_2C_1im][NTf_2]$ can be fitted by two Gaussian functions. (b) The Van't Hoff plot shows linearity and indicates a Gibbs free energy of 8 kJ/mol.

For each divalent salt sample, 15 mM of the salt is added to the ionic liquids. For the free ion sample, 30 mM of the $[C_4C_1im][SCN]$ is added to the solution. All the samples are stirred overnight and filtered with 0.2 μm syringe filter before measurement. 15 mM of $Ca(SCN)_2$ can be fully dissolved in the ionic liquids, which is confirmed by the peak height of the SCN peak. The $Ba(SCN)_2$ is only slightly soluble with a estimated solubility of ~5 mM from the acquired FTIR spectra.

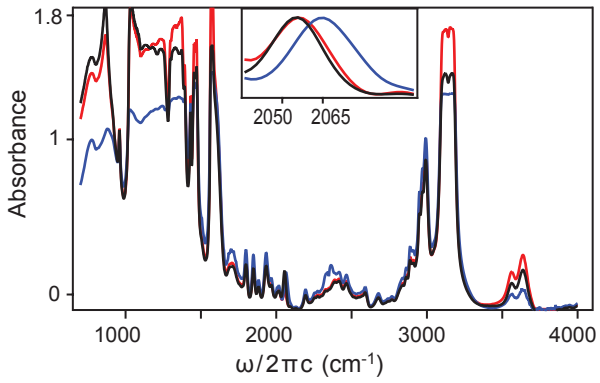

Figure 17: The FTIR spectra of SCN^- (black) $Ca(SCN)_2$ (blue) and $Ba(SCN)_2$ (red) in $[C_2C_1im][NTf_2]$, and the zoomed-in SCN peaks (inset).

The FTIR spectra of the divalent SCN salts show a complicated dependence on the cation. The free SCN peak shows up at $\sim$ 2053 cm^{-1}, which is consistent with previous experiments. The $Ca(SCN)_2$ peak is blue shifted to around 2065 cm^{-1}, and exists as a single peak. The $Ba(SCN)_2$ peak has a very similar position as the free ion peak, and is very slightly shifted to the blue side.

The peak position, in certain aspects, shows an unexpected consistency with the monovalent salts. For the alkali metal SCN salts, we have seen that the NaSCN ion-pair is blue shifted to 2065 cm^{-1} while the KSCN stays at 2053 cm^{-1} and the peak is almost undistinguishable from the free SCN ion. Changing from a lighter cation to a heavier cation, the central frequency is red shifted for both cases. The central frequency of the SCN-based salts can be grouped into two groups: the Na- and Ca-based salts both show up at ~2065 cm^{-1}, while the K- and Ba-based salts show up at ~2053 cm^{-1}.

The $Ca(SCN)_2$ shows no sign of a second peak at 2053 cm^{-1}. This indicates that there is no detectable thiocyanate free ion in solution, and the $Ca(SCN)_2$ does not dissociate. The molecular structure for $Ba(SCN)_2$ is impossible to tell from the FTIR, and a 2D-IR experiment is needed.

To understand the dynamics of the two divalent salts in ionic liquid, 2D-IR experiment is conducted (figure 18). For all three systems, the 2D-IR spectra are elongated along the diagonal axis in the early waiting time (0.2 ps). As the waiting time increases (30 ps), the spectra gradually lose the correlation in all three systems, and the $Ca(SCN)_2$ and $Ba(SCN)_2$ systems lose less than the free ion system. When the waiting time is sufficiently long (100 ps), the free SCN completely loses its initial correlation, and the spectrum becomes round in shape; the $Ca(SCN)_2$ and $Ba(SCN)_2$ still preserve a significant amount of correlation. By fitting the spectra with ellipticity, the frequency fluctuation correlation functions can be obtained. The free ion completely loses its correlation in the experimental timescale, while the $Ca(SCN)_2$ and $Ba(SCN)_2$ systems have much slower dynamics that do not fully resolve within 200 ps time window.

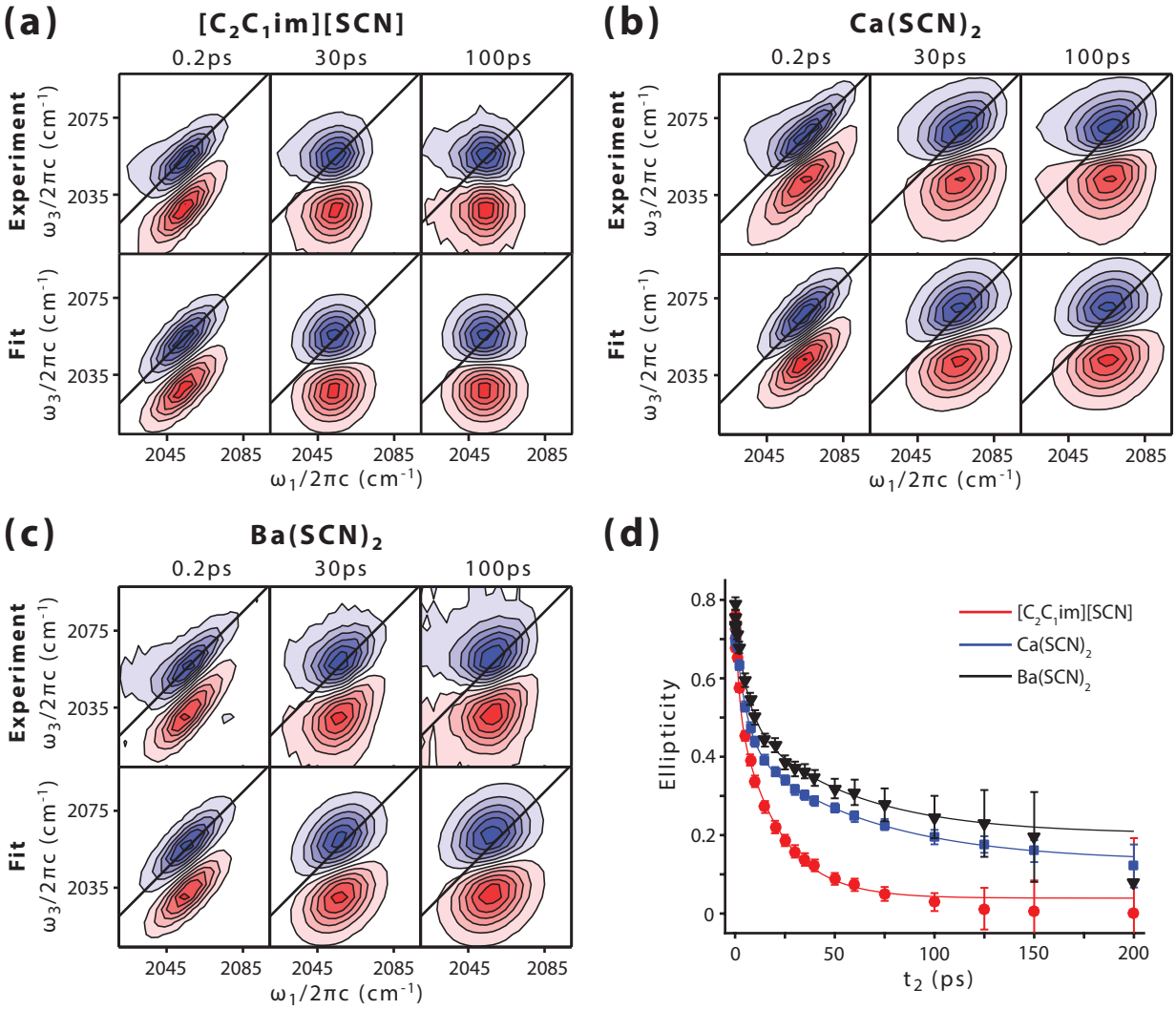

Figure 18: (a) The experiment (top) and fit (bottom) 2D-IR spectra of free SCN ion in $[C_2C_1im][NTf_2]$. (b) the experimental and fit 2D-IR spectra of $Ca(SCN)_2$ in $[C_2C_1im][NTf_2]$. (c) the experimental and fit 2D-IR spectra of $Ba(SCN)_2$ in $[C_2C_1im][NTf_2]$. (d) the frequency fluctuation correlation function of free SCN ion (red), $Ca(SCN)_2$ (blue) and $Ba(SCN)_2$ (black).

Given that the FTIR imply that $Ca(SCN)_2$ does not dissociate at all in the ionic liquid solution, the measured dynamics is therefore the dynamics of the triple ion (here, we borrow the term from Marcus[204] to emphasize that it is composed of three ions, though the term originally indicates a charged cluster rather than a neutral one). It can be seen that the

dynamics of the triple ion are significantly slower than the free thiocyanate ion, with a residue correlation of $\sim$ 0.2 even at 200 ps. It is unclear whether $Ba(SCN)_2$ is dissociated in the FTIR, but with the aid of 2D-IR it is clear that it is forming triple ions in the solution, since the dynamics are highly similar to that of $Ca(SCN)_2$. The dynamics of $Ba(SCN)_2$ are even slower than the $Ca(SCN)_2$. The $Ba(SCN)_2$ dynamics are only measured up to 150 ps, which is because the low solubility limits the signal intensity at long waiting times.

By fitting the experimental data with a biexponential plus a constant, the three systems can be quantitatively compared (table 2). The dynamics of the SCN ion is in agreement with other experiments. The free SCN ion dynamics have two timescales: one is in the order of $\sim$2 ps and has a smaller impact on the total correlation; the other timescale is at $\sim$20 ps and has the major impact on the total correlation lose; the static offset is very small or negligible, meaning the dynamics are fully resolved within our waiting time window. The dynamics for the triple ions are different from the free ion. Both $Ca(SCN)_2$ and $Ba(SCN)_2$ have a first timescale with similar amplitude as the free ion, but are much slower ($\sim$6 ps). The second timescale is also significantly slower than the free ion ($\sim$60 ps), and the amplitude is reduced to the similar order of the first timescale. There is a static offset of $\sim$0.15 for both triple ions, which is another major difference from the free ion.

Table 2: Experimentally resolved timescales of dynamics of free SCN ion, $Ca(SCN)_2$ and $Ba(SCN)_2$ in $[C_2C_1im][NTf_2]$

	free SCN	$Ca(SCN)_2$	$Ba(SCN)_2$
C_1	0.24 $\pm$ 0.04	0.30 $\pm$ 0.05	0.26 $\pm$ 0.11
C_2	0.49 $\pm$ 0.03	0.30 $\pm$ 0.04	0.30 $\pm$ 0.10
t_1 (ps)	1.8 $\pm$ 0.5	5.6 $\pm$ 0.8	5.9 $\pm$ 1.0
t_2 (ps)	21 $\pm$ 3	63 $\pm$ 20	53 $\pm$ 20
C_3	0.04 $\pm$ 0.02	0.13 $\pm$ 0.04	0.20 $\pm$ 0.12

The big uncertainty of the second timescale and the static offset may come from the coupling between the two components. When the dynamics are not fully resolved, the remaining correlation could be coming from a static component, or from the fact that the exponential decay of the longer timescale is not fully resolved. Due to the experimental noise, these two components are hard to be determined unambiguously since the difference between their behavior is minor. Therefore, the big uncertainty comes from difficulty of accurately determining the source of the residue correlation. None the less, when considering the two components together, it is clear that the dynamics are slowed down for both triple ion systems.

The deceleration in dynamics can be understood as the fact that the microscopic motion changes from a single ion to the triple ion. In chapter 3, we referred to the faster timescale as the rattling motion of the ion or triple ion in the ion cage, and the second timescale as the breakage and reformation of the ion cage. For the triple ion case, these motions could refer to the motion of the entire triple ion, and the ion cage could be the ion network that surrounds the entire $Ca(SCN)_2$ or $Ba(SCN)_2$. It is reasonable to assume that the increasing size of the entity lead to a slower dynamics for both rattling motion and the breakage and reformation of the microscopic environment.

It is also interesting to note that both timescales for the triple ions are approximately three times slower than the free ion dynamics. Naively one could correlate this with the fact that there are three ions for the triple ion, while only one ion for the free ion case. It is possible that the occupied volume is tripled and caused the dynamics to be slowed approximately three times. This analysis could be unsubstantiated since the correlation may not be real due to high uncertainty of the long timescales, but the current result strongly indicates that there are direct correlation between the resolved timescales and the microscopic structure.

5.3 DISCUSSION

5.3.1 The ion-pair energy is in good agreement with the computational calculation

The experimentally-determined ion-pair Gibbs free energy is approximately 8 kJ/mol lower more stable than the separated ions, which is in good agreement with the prediction from Kirchner[40,165]. The stability of ion-pair is dependent on the choice of salts and the choice of ionic liquid. The ion-pair stability should first be dependent on the lattice energy of the ionic crystal. In this case, NaCl is expected to have higher ion-pair energy since the lattice energy of NaCl is higher. Second, the ionic liquid that we chose has a shorter chain length on the cation, and therefore is smaller. $[C_2C_1im][NTf_2]$ is expected to be better at solvating the NaSCN since the smaller ions could potentially get closer to the solute ion. With these two factors considered, we believe that our experimentally determined ion-pair energy is in good agreement with the theoretical prediction.

The formation of ion-pair in ionic liquids may be seemingly surprising. Naively, the ionic liquid should have a more similar microscopic environment with the inorganic salts than the water, since the coulombic force is the dominating force in the solvent. In the water system, alkali metals do not form ion-pairs with the thiocyanate until the salt concentration is raised to $\sim$ 1 M, where the clustering behavior is observed[227]. For divalent thiocyanate salts, the ion-pairs are not evident until the concentration of the aqueous solution is on a order of 0.3 M, and the free ions are still the dominating species even at a concentration of 3 M[4,5,228]. For ionic liquids, however, ion-pairing is observed at a much lower concentration of 30 mM, and for $Ca(SCN)_2$, the presence of the free ion is under the detection limit.

In fact, this phenomenon can be readily explained and is consistent with the water system. Utilizing equation 5.1, the Bjerrum distance of mono-valent ion-pair in $[C_2C_1im][NTf_2]$ is $\sim$2.2 nm (given that the dielectric constant is 12.3[229]). This distance is much bigger than both ions of the solute, so ion-pair formation is expected for this ionic liquid. On the other hand, however, with a much higher dielectric constant, water has an Bjerrum distance of

only ∼0.3 nm, which is similar to the size of the ions, and therefore the ion-pair formation is not expected. Moreover, if we compare the number density of the system, the difference is much smaller than the concentration by volume: 30mM NaSCN in $[C_2C_1im][NTf_2]$ has a number density of 2.5%, while 3M of NaSCN in water has a number density of 5%, which is of the same order of magnitude.

5.3.2 The microscopic structure of divalent salts

The 2D-IR and FTIR spectra of $Ca(SCN)_2$ in $[C_2C_1im][NTf_2]$ shows that these salts do not dissociate in ionic liquids. The SCN antisymmetric stretch band shows up as one single peak both in the FTIR and 2D-IR, and is blue shifted away from the free ion peak. This means that there is only one type of SCN in the ionic liquid, and it is not the SCN free ion. This is a strong indication that the $Ca(SCN)_2$ does not dissociate at all in the ionic liquid. The $Ca(SCN)_2$ exists as an triple ion[204]. For $Ba(SCN)_2$, the SCN peak position and shape are similar to the free ion, but the 2D-IR reveals similar dynamics as $Ca(SCN)_2$. Therefore, the microsopic structure of $Ba(SCN)_2$ is very likely to be also triple ions.

Moreover, the single peak indicates that the two thiocyanates associating with the calcium ion are identical to each other. For certain divalent salts, the counter ions, though form ion-pairs, could form different types of ion-pairs. For example, the $LaCl_3$ ion in water can form two types of ion-pairs[224]: the first type is a contact ion-pair located ∼2.8 Å away from the lanthanum ion; the second type is a solvent-shared ion-pair that locates ∼2.8 Å away. If that was the case, we would expect that our FTIR spectra to have two peaks of different frequencies, and in the 2D-IR spectra to have distorted peak shapes. We did not observe the sign of another ensemble, which suggests that thiocyanate only adopt one type of ion-pair in the ionic liquid with the calcium cation.

5.3.3 The source of static offset for the ion-pairs

For KSCN, $Ca(SCN)_2$ and $Ba(SCN)_2$, the observations all indicate a static offset that could not be resolved within a 200 ps timescale. In chapter 6, the AOT - $[C_4C_1im][SCN]$ colloidal dispersion system also has a significant static offset. It is therefore interesting to discuss the source of this correlation.

The information content of 2D-IR in the inhomogeneous limit is the two-point frequency fluctuation correlation function. In order to have a frequency correlation, a distribution of frequencies is required. Typically in an ionic liquid, the microscopic environment can affect the instantaneous frequencies of ions, and results in an ensemble of frequencies from different microscopic environments. The second source is the orientation of the molecule. If an ion is placed in a local electric field, the frequency of one vibrational mode can be affected by the relative orientation between the electric field and the transition dipole. The spectral diffusion process is then a combination of the two types of motions.

From chapter 7, we have shown that a strong local electric field can introduce a non-isotropic distribution of the molecules, and this non-isotropic distribution gives rise to an incomplete reorientation of the system. When the molecules are near a strong local electric field, the dipole moment will tend to align with the electric field to lower the energy. In this case, the orientation of the molecule or ion is favored in a direction, thus forms a non-isotropic orientation distribution. Assuming that the local electric field does not change over the course of the experimental waiting time, depending on the polarization configuration, there will be positive or negative static offsets. For the case of ion-pairs, the counter ion is directly adjacent to the probe ion. The strong local electric field is very likely exerted from the counter ion to drive the probe away from isotropic distribution.

If the counter ion moves its relative position to the probe ion, the static offset will start to vanish. It has been discussed in the previous paragraph that the requirement for the static offset is that the local electric field is not fully randomized during the experiment waiting time. Since the local electric field is mainly generated by the counter ion, this indicates that the relative position between the cation and anion probe should not completely randomize

during the waiting time. In other words, ion pair or the triple ions structure as whole should not completely reorient within our experimental timescale. When looking from the perspective of the probe, however, the relative motion of the counter ion is attributed to the structural reorientation, meaning that the structural spectral diffusion is the term that ultimately determines the existence of the static offset. This is consistent with the model proposed by Fayer, or the equation 7.3 derived in their original work[226,230,231].

This static offset indicates that there are two different types of reorientation motions for the ion-pair. The ion-pairs can reorient in the solution as a single entity. The individual ions can also reorient themselves in the ion-pair, but the reorientation is incomplete due to a non-isotropic distribution created by the local electricfield. The reorientation time for the ion-pair is much longer than the reorientation time for the individual ions. Such separation of reorientation timescales in ion-pair is consistent with previous optically heterodyned polarization spectroscopy research[232,233].

The static offset from the ion-pair scenario can therefore be taken as a synergistic effect of both incomplete reorientation and incomplete structural reorganization. The strong local electric field generated by the counter ion drives the probe to a non-isotropic distribution, which causes the static offset. The relative structural motion of the counter ion will change the orientation of the ion-pair, and if this process is much slower than the experimental waiting time limit, the generated static offset wil bel preserved. During our experiments, we see constant offsets for all the systems, including the ion-pair, triple ions and clusters systems. These results indicate that the reorientation process of the total ion structure is slow compared with the experimental waiting time limit.

5.4 CONCLUSION

In this chapter, we have further explored two fundamental questions about ion-pairs of inorganic salts in the ionic liquids.

The 2D-IR spectra of NaSCN ion-pair in the ionic liquid $[C_2C_1im][NTf_2]$ shows a twisted shape at long waiting times. This indicates that there are two types of SCN in the solution, and one being the NaSCN ion-pair. The NaSCN ion-pair in the ionic liquid $[C_2C_1im][NTf_2]$ is shifted to higher frequency, and both the free ion and the ion-pair has detectable concentration. The equilibrium constant of the dissociation process is quantified by the FTIR data, and is used to calculate the thermodynamic stability of the ion-pair. We found that the NaSCN ion-pair has an Gibbs free energy of ~ 8 kJ/mol, which is in good quantitative agreement with the theoretical prediction.

The formation of ion-pair for divalent salts are also tested with $Ca(SCN)_2$ and $Ba(SCN)_2$. For the $Ca(SCN)_2$, the SCN peak is blueshifted to higher frequencies, and shows no sign of free SCN peak. In the 2D-IR spectra, the SCN peak exists as a single two dimensional Gaussian for all the waiting times, indicating that there is only one type of thiocyanate in the solution. $Ca(SCN)_2$ is therefore not dissociated at all in the solution, the salt exists as $Ca(SCN)_2$ complex. The dynamics of both the $Ca(SCN)_2$ and the $Ba(SCN)_2$ both have a positive offset at longer waiting times, which is similar as previously reported. The resolved dynamics are slower than the free ion dynamics, which is possibly because that the ion-pair is a bigger entity than the free ions, which diffuses slower in the solution. While the dynamics are not slowed down too much, it is possible that the ion-pair does not have much effect on the ion network.

6.0 ULTRAFAST DYNAMICS OF IONIC LIQUIDS IN COLLOIDAL DISPERSION

The text in this chapter has been adapted from Ren, Z.; Kelly, J.; Gunathilaka, C. P.; Brinzer, T.; Dutta, S.; Johnson, C. A.; Mitra, S.; and Garrett-Roe, S. *Phys. Chem. Chem. Phys.* **2017**. The author's contribution to this work included identifying the knowledge gap, choosing the systems of study, conducting the FTIR and 2D-IR experiments and data analysis, and writing the text of the manuscript.

6.1 CHAPTER SUMMARY

Ionic liquid (IL)- surfactant complexes have significance both in applications and research, but their underlying dynamics have not been well understood. We applied polarization-controlled two-dimensional infrared spectroscopy (2D-IR) to study the dynamics of $[C_4C_1im][SCN]$/ surfactant/ solvent model systems. We examined the effect of the choice of surfactants and solvent, and the IL-to-surfactant ratio (W value), with a detailed analysis of the orientation and structural dynamics of each system. The results showed that different surfactants affect the dynamics of ionic liquids entrapped in a widely different manner, ranging from creating a semi-static micro-environment to creating dynamics that are even faster than common bulk ionic liquid dynamics. The solvent also clearly affected the microscopic dynamics. The anisotropy decay for entrapped ILs completed within 10 ps, which was similar to free thiocyanate ion in water, while a significant reorientation-induced spectral diffusion

(RISD) effect was observed. The results showed that the dynamics of the entrapped ionic liquid are highly dynamic, opposite to what one would expect for the reverse micelles. We hypothesized that instead of an ionic liquid-reverse micelle (IL-RM), the microscopic structure of this system was small colloidal dispersions or pairs of IL and surfactants. A detailed analysis with the polarization-controlled 2D-IR spectra of AOT system reveals a potential ion-exchange mechanism.

6.2 INTRODUCTION

Ionic liquids (IL) are a kind of liquid in which each formula unit is a cation-anion pair; they are room temperature molten salts[96,130]. Due to their special structure, they posses valuable properties such as low vapor pressure, low flammability, excellent chemical and physical stability. Therefore, they are considered a new generation of "green solvents."[95,131,137,234] Many potential applications are under expedited investigation, ranging from the carbon capture[90,132,133], to reaction media[136,137], to electrolytes for electrochemistry purposes[134,135].

Normally ILs are not soluble in most non-polar organic solvents, such as benzene and chlorobenzene; however, with the aid of surfactants, ILs can be dissolved[235–243]. For example, one of the most well-studied ILs, 1-butyl-3-methylimidazolium bis(trifluoromethanesulfonyl)-imide ($[C_4C_1im][NTf_2]$), can dissolve in many common solvents, including cyclohexane[244,245], benzene[240] and chlorobenzene[246], with the addition of benzyldimethylhexadecylammonium chloride (BHDC), docusate sodium (AOT) or Triton X-100 (TX-100). The dissolution process shows characteristic feature of micro-structures, since the solubility of ionic liquids is not determined by the absolute concentration of the surfactant, but the IL-to-surfactant concentration ratio (W value).

The microscopic structure of the IL-surfactant complex is often considered a reverse-micelles. Reverse micelles are thermodynamically stable mixtures two immiscible liquids, which usually are oil and water for molecular liquids, and a surfactant to stabilize. Com-

pared with other microemulsions, reverse micelles are considered round in shape, with the surfactant serving as a "shell" to separate the polar solute from the organic phase. W values are often less than 5 in IL-surfactant systems. From DLS and neutron scattering experiments, the size of the micro-structure varies based on the choice of IL. Some ionic liquids, like $[C_4C_1im][BF_4]$, form large clusters with a typical size of 20nm[236], while some others, like $[C_4C_1im][NTf_2]$, form micro-structures with a size of $\sim$2 nm[240].

The ILs dissolved provide a microscopic ionic environment inside a highly non-polar environment, and such unique structure provides opportunities for the design of "micro-reactors"[83,84,87]. Research points out that some enzymes such as trypsin have higher reactivity when confined within these reverse micelle structures[85]. Some reactions increase their reaction rate constant in IL-RMs. Recently, there is also a increasing focus on synthesizing nano-particles in these systems[86,87].

In spite of the great potential of this system, however, little is known about the microscopic structure and dynamics, which greatly hinders the advancement of the applications. H^1NMR and FTIR study reveals some crucial dynamic information such as ion-exchange between the entrapped IL and BHDC[240,247]. DOSY experiments find that the viscosity of $[C_4C_1im][BF_4]$ is even lower when softly confined than in the bulk[242]. The microscopic dynamics of IL-RMs are crucial to the understanding of many fields including nano-reactors and electrochemistry, but the research is far from conclusive.

Without a proper tool, studying the microscopic structure and dynamics of such systems is difficult. The solvent dynamics of ionic liquids resolve between picoseconds and nanoseconds, which is faster than the time-resolution of spectroscopy methods such as NMR. The small spatial scale of reverse micelles hinders the applications of many other ultrafast spectroscopy methods. For example, fluorescence spectroscopy employs large laser dyes that are approximately the same size of an ionic-liquid cluster[108–114]. Other techniques, such as Kerr-effect-based spectroscopies average over all components of the motions of the liquid, weighted by Raman polarizability[111,115–117].

Two-dimensional infrared spectroscopy (2D-IR) is an ideal tool to study this system[1].

The chromophores of 2D-IR could be vibrational modes of a function-group of the entrapped ionic liquid, providing molecular-level spatial resolution. 2D-IR can trace time correlations of vibrational frequencies at a picosecond scale and therefore provides valuable insights of structures and dynamics of the probe vibrator in the dynamic ionic environment. Moreover, the vibrational spectrum is in general sensitive to both intra- and inter-molecular geometry and therefore can be used as a reporter of the local environment in such IL-surfactant complexes[152–157,248,249].

Previously, 2D-IR has proved useful to understand the microscopic dynamics of molecular liquids under confinement[18,19,22]. By examining the water-based reverse-micelles, two distinct types of water dynamics have been distinguished, which are then related to a core-shell structure of water. The effects of different salts in such systems have also been studied, and resulted in an observation that some salts may either introduce order in reverse micelles (Kosmotropes) or disturb it (Chaotropes). Polarization control provides another approach to understand the system. The anisotropy analysis of confined water shows that they reorient much more slowly compared to the core water[18,250].

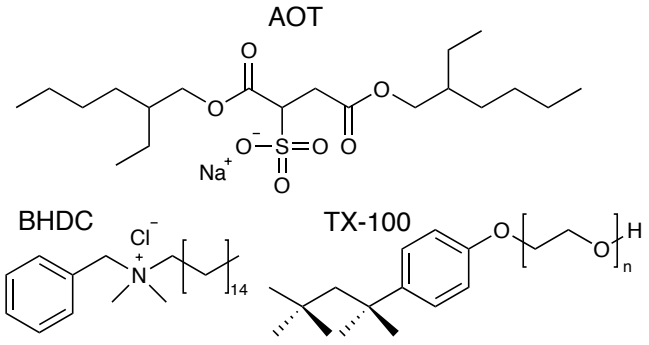

Figure 19: The chemical structures of anionic (AOT), cationic (BHDC) and non-ionic (TX-100) surfactants.

We choose to use $[C_4C_1im][SCN]$ as our model ionic-liquid. Thiocyanate is a widely used vibrational chromophore for 2D-IR with great properties. The C≡N stretch mode has a high extinction coefficient of $\sim 800 M^{-1}cm^{-1}$, and its vibrational lifetime is long enough for solvent dynamics of ionic liquids. We have shown in our previous research that this vibrational mode is sensitive to the local environments and is capable of reporting local

structures such as ion-pairs[129,251]. Moreover, as the anionic component of the ionic liquid, thiocyanate offers a label-free experiment to directly probe the dynamics of ionic liquids under confinement without disturbing the micro-environment. Therefore, it is reasonable to expect that $[C_4C_1im][SCN]$ is capable of resolving the microscopic dynamics of ionic liquids under confinement.

In this paper, we analyze three parameters that could potentially affect the dynamics of ionic liquids in confinement: the type of surfactant, the choice of solvent, and the IL/surfactant concentration ratio (W value). We chose three common surfactants, each representing one distinct type of surfactant: docusate sodium (AOT) as an anionic surfactant, benzyl-n-hexadecyldimethylammonium chloride (BHDC) as a cationic surfactant, and Triton X-100 (TX-100) as a non-ionic surfactant (Fig. 19). Two solvents, chlorobenzene and dichloromethane were chosen for their significant difference in viscosity. For each of the three surfactants, two different W values, W = 0.25 and W = 0.50 were measured. For each experiment, 2D-IR spectroscopy was conducted with two polarizations, namely all parallel (ZZZZ) and perpendicular (ZZXX).

We will show that the choice of surfactants and solvents greatly affect the dynamics of the ionic liquids dissolved. The W value is also responsible for the dynamics of ILs, as a larger W value yields faster dynamics for all types of surfactants. We will also show that the reorientation dynamics of thiocyanate ion is comparable to free thiocyanate in the water. During the experiment, we have found our result is significantly distinct from the water-based reverse micelles result, indicating that $[C_4C_1im][SCN]$ is not forming reverse-micelles in the system. Instead, we hypothesize that the $[C_4C_1im][SCN]$ forms clusters with the surfactants in the organic solvents. We will also show a possible ion-exchange mechanism in the AOT-IL complex, where the sodium cation is exchanged with $[C_4C_1im]$ cation and yields some surprising dynamics.

6.3 EXPERIMENTAL AND DATA-REDUCTION METHODS

The ionic liquid $[C_4C_1im][SCN]$ was purchased from Ioli-tec, and dried under vacuum for 12 hours prior to use. All of the surfactants and organic solvents were purchased from Sigma-Aldrich. The TX-100 sample was dried under vacuum for 12 hours prior to use, while BHDC and AOT were recrystallized three times with dichloromethane to remove water before use. Anhydrous chlorobenzene and dichloromethane were used as received.

To prepare a sample, the surfactants are first weighed and added to the solvent, and stirred until fully dissolved. Then the ionic liquid is added drop by drop from a pipette to the solution. The solution is then stirred at room temperature over night. Prior to use, each sample is filtered with 0.2 μm syringe filter to remove large particles and aggregates.

The DLS instrument is a Malvern ZS90 Zetasizer with 633 nm laser light. The DLS experiments are done with 90 degree angle at room temperature. H^1NMR and DOSY experiments are performed on a Bruker Avance III operating at 600MHz.

Infrared spectroscopic cells consist of 20 μL of sample held between two 2 mm thick calcium fluoride windows which were separated by a 100 μm O-ring Teflon spacer. The sample cell assembly is executed under inert gas atmosphere. FTIR of each sample is taken before and after 2D-IR experiment to ensure the integrity of the solution content.

For the 2D-IR experiment, $\sim$120 fs pulses of 800 nm wavelength were generated by a commercial Ti:Sapphire chirped pulse amplifier of 1 mJ at a repetition rate of 5 kHz. An optical parametric amplifier (OPA)[88] generated $\sim$2 μJ tunable mid-IR pulses of sub 100 fs duration, centered at 2050 cm^{-1}, with a bandwidth of 250 cm^{-1}. For the 2D measurements we use a Fourier transform 2D-IR setup in the pump-probe geometry as described by Helbing *et al*[89] (essentially identical to that report, except the repetition rate is 5 kHz). The data acquisition was performed with a fast-scanning routine without phase ambiguity. To achieve polarization-sensitive 2D-IR, a set of $\lambda/2$ waveplate and wire-grid polarizer is placed in the beam path of infrared-pumps. Each data point is done with both ZZZZ and ZZXX polarization.

The 2D-IR spectra is fitted with two two-dimensional Gaussian functions. The amplitude of the Gaussian function is taken to calculate the anisotropy decay. The change in shape of the 2D-IR spectra over population time is quantified by ellipticity[122,123]. The ellipticity is then fit to extract the dynamics.

6.4 RESULTS

6.4.1 Solvent- and surfactant- dependence of complex-formation

To the best of our knowledge, $[C_4C_1im][SCN]$ has not been studied in these complexes. Therefore it is crucial to check the conditions of IL-surfactant complex-formation with this IL.

Without the aid of surfactants, $[C_4C_1im][SCN]$ could not dissolve in any of the tested solvents (Table 3). With the presence of the surfactants, $[C_4C_1im][SCN]$ shows solvent- and surfactant-dependent solvation. Chlorobenzene is capable of dissolving all of the three IL-surfactant complexes, while benzene and dichloromethane could not dissolve BHDC/IL. Cyclohexane and hexane do not solubilize the complex at all.

Compared with the previous study, the cluster-formation could be highly ionic liquid-specific. There are cases where $[C_4C_1im][SCN]$ could not be dissolved while other ILs could. Literature has been shown $[C_4C_1im][NTf_2]$ and $[C_4C_1im][BF_4]$ are capable of forming reverse micelles in TX-100/cyclohexane[244,245] as well as BHDC/benzene systems, but $[C_4C_1im][SCN]$ could not.

$[C_4C_1im][SCN]$ forms microscopic particles with surfactants. In our experiment, for each data point, we checked not only the solubility, but also the dependence of the solubility as a function of concentration. We found that for all the cases that $[C_4C_1im][SCN]$ dissolved, the solubility is dependent on the concentration ratio between the IL and surfactant, or W value, rather than the absolute concentration of the surfactant. This phenomenon is a strong

Table 3: Solubility of IL-surfactant complex with different solvents and surfactants

surfactant	Chlorobenzene	Benzene	Dichloromethane	Cyclohexane	Hexane
BHDC	✓	✗	✗	✗	✗
AOT	✓	✓	✓	✗	✗
TX-100	✓	✓	✓	✗	✗[a]

[a] Surfactant not soluble

indication that the IL and surfactant form microscopic structures in the organic solvent.

We chose chlorobenzene and dichloromethane as our solvents to conduct our spectroscopy experiments.

6.4.2 Size characterization of IL-surfactant complexes

DLS experimens were conducted to characterize the size of the IL-surfactant complex. Unfortunately the counting rate from the DLS result is too weak to yield interpretable data. A minor feature in the DLS plot could potentially come from the complex, which yields a size of ∼1 nm (Supporting information).

Since DLS results are inconclusive, DOSY experiments are then performed to characterize the size. In $[C_4C_1im][SCN]$/BHDC/Chlorobenzene system, H^1NMR data shows a clear singlet peak at 9.8 ppm, which is considered to be 2-position hydrogen of the imidazolium ring. The chemical shift of this peak in BHDC decreases as the W value increases, which is consistent with previous result[240] with $[C_4C_1im][NTf_2]$/BHDC system. This peak is then chosen to be the probe in the DOSY experiment.

The DOSY experiment yields the diffusion coefficient of the IL-surfactant complex, and the sizes are calculated via the Stokes-Einstein equation. The average size is around 2 nm for all systems, which is consistent with literature DLS data with $[C_4C_1im][NTf_2]$. As the W

value goes up, however, the size decreases. This trend is opposite to the literature. In our case, when W = 0.2, the calculated size of the micro-structure is the biggest while W =1.0 yields the smallest size (table 4).

Table 4: DOSY results of 2-position hydrogen in IL-BHDC complexes

W	Chemical Shift (ppm)	Diffusion Coefficient ($10^{-10}m^2/s$)	Calculated Size (nm)
0.2	9.911	1.721	3.369
0.5	9.696	2.510	2.310
0.8	9.559	2.647	2.190
1.0	9.536	3.146	1.843

6.4.3 The FTIR result of SCN peak within IL-surfactant complexes

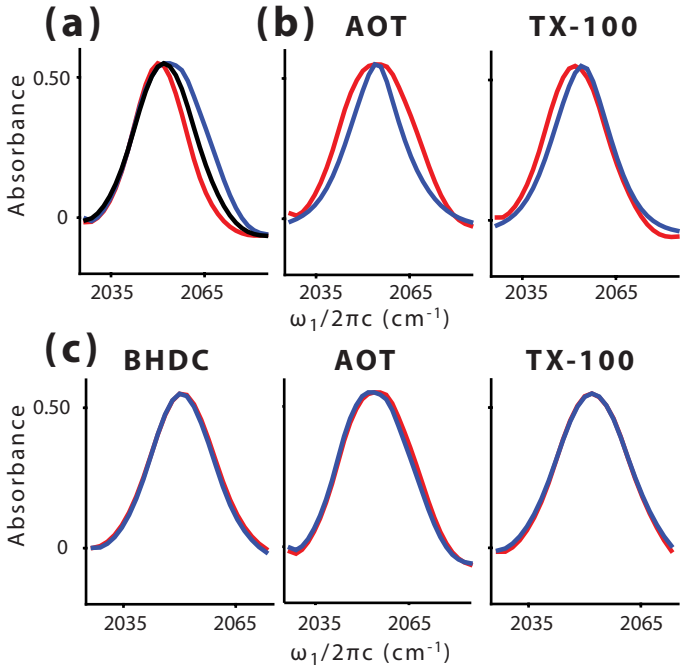

Figure 20: a) FTIR of SCN^- bands with surfactants BHDC (red), AOT (blue) and TX-100 (black) in chlorobenzene indicates different local environments of SCN^-; b) FTIR of the IL-surfactant complex in chlorobenzene (red) and dichloromethane (blue) shows significant effect of the solvent; c) FTIR with W = 0.25 (red) and W = 0.50 (blue) show minor effect on the shape and position of the SCN band.

The FTIR experiment shows the change in lineshape of thiocyanate antisymmetric stretch mode as a function of other parameters. The peak position of the C≡N stretch of SCN^- is not greatly different from system to system, and is mostly centered around 2050 cm^{-1}, with a extinction coefficient of ∼840 $M^{-1}cm^{-1}$. The linewidth of the peak, however, is greatly different from system to system. The AOT sample having the broadest full-width-at-half-maximum (FWHM) of 27.0 cm^{-1}, with the BHDC sample has the most narrow one with a FWHM of 19.6 cm^{-1}, and the TX-100 having an intermediate value, with FWHM of 22.3 cm^{-1}.

The linewidth is also greatly affected by the choice of the solvents. Switching from

chlorobenzene to dichloromethane, the FWHM are decreased both in AOT system and in TX-100 system (Fig. 20).

The peak profile is not sensitive to varying most other parameters. We could see that changing the W value from 0.25 to 0.5 does not yield a significant change in either the peak position or the FWHM.

The above result indicates that the choice of surfactant is the most important factor that determines the local environment of the ionic liquid anion. Though the FTIR provides a hint of micro-environments, the change in line-shape could be either dynamical or structural. In this situation, 2D-IR experiments are needed to distinguish between the two possibilities.

6.4.4 Reorientation dynamics of entrapped ionic liquids

The anisotropy measures the reorientation dynamics of SCN^- in the IL-surfactant micro-structure. The anisotropy decay curves for all three surfactant systems show similar decays (Supporting information). For all the three systems, the initial value of anisotropy is close to 0.3, which is below the theoretical maximum, indicating that the majority of reorientation happens within our time scope. As the waiting time increases, the anisotropy experiences a steep decay, and at around 10 ps, the value decays to 0, which means that the reorientation correlation is completely lost. The similarity of the decay patterns across all tested systems implies the reorientation dynamics are mostly independent of the choice of surfactant.

Table 5: Reorientation time for SCN^- depends mostly on the choice of solent

	Reorientation time (ps)		
	Chlorobenzene		Dichloromethane
surfactant	W=0.25	W=0.5	W=0.5
BHDC	8.6	8.6	/
AOT	7.3	6.3	3.3
TX-100	7.3	6.5	3.0

A single exponential fit captures the main features of the anisotropy decay, and suggests that the reorientation is mostly diffusive. The exponential fit yields similar timescales of roughly 8 ps for all three surfactant systems, indicating the minor effect of surfactant on the reorientation dynamics. It could also seen that the anisotropy is not very sensitive to the W value. In general, as the W value increases, the reorientation time decreases.

Another important feature is the dependence of reorientation timescales on the solvent. Switching from chlorobenzene to dichloromethane, the reorientation timescale is decreased by ∼50 %.

6.4.5 2D-IR SPECTRA

Typical all parallel polarization 2D-IR spectra for all three surfactant systems in chlorobenzene at W = 0.5 are shown in Fig. 21(a). The spectra each have two peaks. The diagonal peak (blue) originates from stimulated emission and ground state bleach ($\nu = 0$ to $\nu = 1$ transition). The off-diagonal peak (red) comes from vibrational excited state absorption ($\nu = 0$ to $\nu = 1$ transition). At 0.2 ps, all of the three samples show strong evidence of inhomogeneous broadening, with peaks stretched along the diagonal axis. Different surfactants affect the position and the shape of the lobes differently. The AOT sample is centered at 2057 cm^{-1} with an anharmonicity of 27 cm^{-1} to separate the two transitions, and the inhomogeneous and homogeneous linewidths are 20 cm^{-1} and 7.3 cm^{-1}, accordingly. The BHDC sample is centered at 2051 cm^{-1} with an anharmonicity of 27 cm^{-1} to separate the two transitions, and the inhomogeneous and homogeneous linewidths are 18 cm^{-1} and 7.2 cm^{-1}, accordingly. The TX-100 sample is centered at 2053 cm^{-1} with an anharmonicity of 27 cm^{-1} to separate the two transitions, and the inhomogeneous and homogeneous linewidths are 20 cm^{-1} and 7.9 cm^{-1}, accordingly. At 30 ps, the spectra become rounder for all three systems, indicating the presence of spectral diffusion. Given more time, the system could completely reorganize itself and lose the correlation entirely. This situation is true for BHDC and TX-100 sample at 100 ps. The two lobes are round and the nodal line between the two lobes are parallel to the horizontal axis. This is not the case, however, for the AOT sample. At 100 ps, the AOT

sample still shows a strong correlation, because the diagonal width is 19 cm^{-1}, which is still significantly greater than the antidiagonal width of 14 cm^{-1}. The correlation could not be fully resolved even at 200 ps.

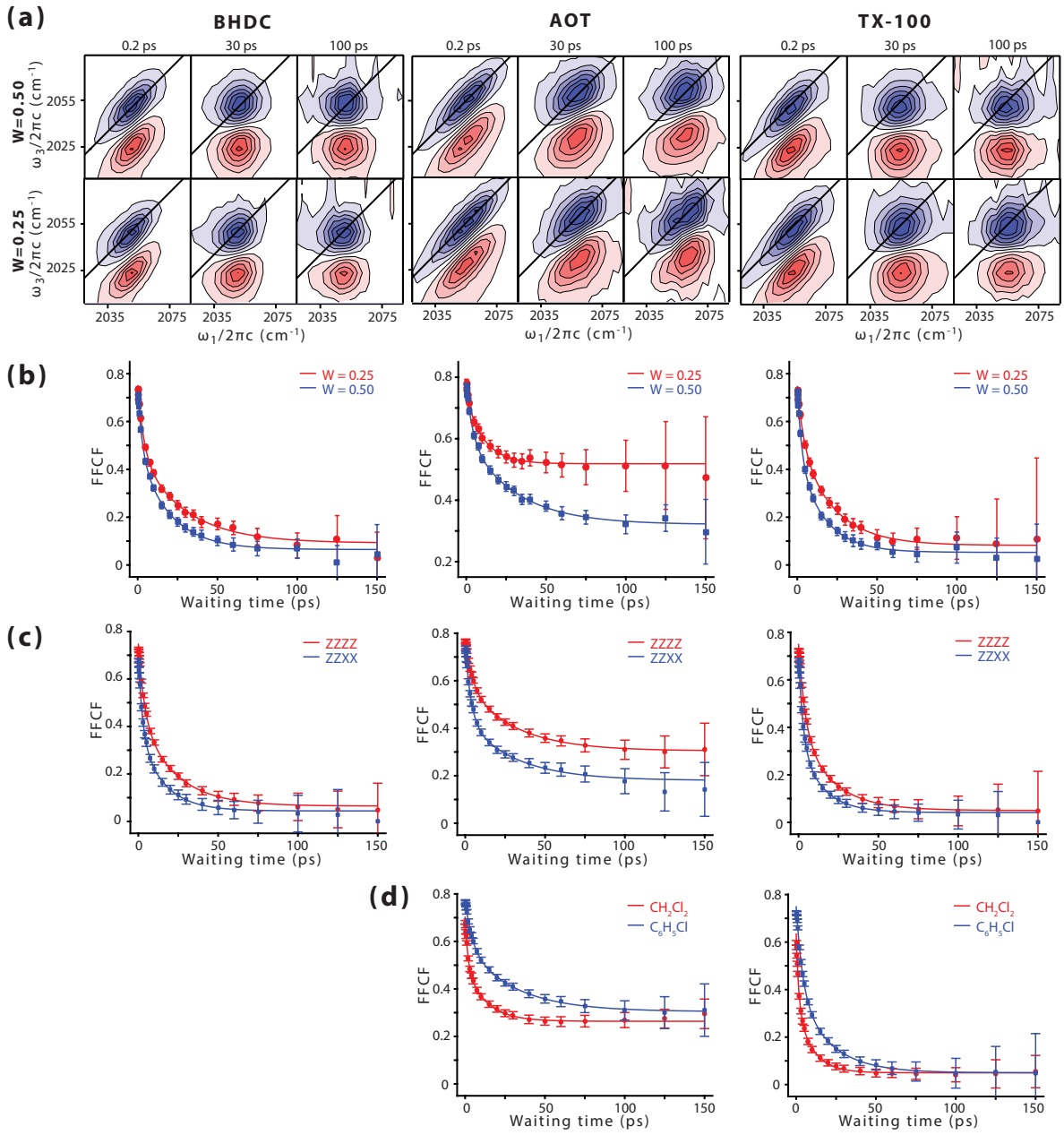

Figure 21: a) Typical 2D-IR spectra at different waiting times for different surfactants with different W values; b) The FFCF in ZZZZ configuration shows that the dynamics are dependent on both surfactants and W value; c) The discrepancy in FFCF of different configurations indicates the RISD effect; d) The solvent plays a important role in determining the dynamics of ionic liquids.

We quantify the dynamics of these systems by fitting them with a frequency fluctuation correlation function (FFCF) that is biexponential plus a constant:

$$c_2(t) = A \exp\left(-\frac{t}{\tau_1}\right) + B \exp\left(-\frac{t}{\tau_2}\right) + C.$$

For BHDC with W = 0.5, the resulting dynamics shows similar features to thiocyanate in ionic liquids[129]: a smaller component of structural relaxation occurs on a few picosecond timescale (τ_1 = 2.9 ps, A = 0.25), and the dominant structural relaxation occurs on a roughly 30 ps timescale (τ_2 = 20 ps, B = 0.41). The correlation is completely lost within our experimental timescale and therefore yields only a negligible constant (C = 0.06). TX-100 follows the similar pattern, with the faster component being 2.7 ps (A = 0.30), and the slower component being 16 ps (B = 0.40), and a static component being very close to zero (C = 0.05). These results also show that thiocyanate dynamics in TX-100 are slightly faster than that in BHDC. AOT, on the other hand, behaves differently from the previous two systems. The two exponentials have similar time constants, but both have weaker impact on the dynamics of the system (3.9 ps and A = 0.18 for faster component, and 30 ps and B = 0.28 for slower component). In contrast to the other two samples, AOT has a dominant static component feature with C = 0.32, which represents slower dynamics that could not be resolved within our 2D-IR experimental timescale.

The W value shows a negative correlation with the observed dynamics. For example, for the BHDC system, changing from W = 0.50 to W = 0.25 increases the faster timescale from 2.9 ps to 3.9 ps, and slower timescale from 20 ps to 29 ps. Both of these changes imply slower local dynamics in W = 0.25 sample. The TX-100 system qualitatively changes similarly. The dynamics of AOT samples slow down in a slightly different way (Table 6): the two resolved timescales lose amplitudes as the W value decreases, and at the same time, the static component becomes bigger.

Changing solvents also affects the observed dynamics. On changing from chlorobenzene to dichloromethane, all systems have a much steeper decay in the ellipticity, indicating the acceleration of dynamics. The fitting values also support the same picture. For example,

Table 6: Time constants as a function of surfactants, solvents, W value and polarization configuration

	BHDC	AOT	TX-100
C_6H_5Cl, W = 0.50,	ZZZZ.		
τ_1(ps)	2.9 ± 0.6	3.9 ± 0.9	2.7 ± 0.5
τ_2(ps)	20 ± 4	30 ± 7	16 ± 3
A	0.25 ± 0.04	0.18 ± 0.04	0.30 ± 0.05
B	0.41 ± 0.03	0.28 ± 0.03	0.40 ± 0.04
C	0.06 ± 0.02	0.32 ± 0.02	0.05 ± 0.01
C_6H_5Cl, W = 0.25,	ZZZZ.		
τ_1(ps)	3.9 ± 0.7	1.5 ± 0.8	4.1 ± 1.4
τ_2(ps)	29 ± 8	11 ± 2	21 ± 6
A	0.28 ± 0.05	0.06 ± 0.03	0.21 ± 0.06
B	0.38 ± 0.04	0.21 ± 0.03	0.44 ± 0.06
C	0.09 ± 0.03	0.52 ± 0.01	0.08 ± 0.03
CH_2Cl_2, W = 0.50,	ZZZZ.		
τ_1(ps)	/	1.7 ± 0.2	1.6 ± 0.2
τ_2(ps)		13 ± 2	10 ± 1
A		0.21 ± 0.02	0.31 ± 0.03
B		0.23 ± 0.02	0.28 ± 0.03
C		0.26 ± 0.01	0.05 ± 0.01
C_6H_5Cl, W = 0.50,	ZZXX.		
τ_1(ps)	2.5 ± 0.3	3.5 ± 0.5	2.6 ± 0.2
τ_2(ps)	15 ± 2	31 ± 9	14 ± 2
A	0.33 ± 0.03	0.32 ± 0.03	0.37 ± 0.03
B	0.33 ± 0.03	0.25 ± 0.02	0.30 ± 0.03
C	0.04 ± 0.01	0.18 ± 0.03	0.04 ± 0.01

the slower timescale for TX-100 sample is accelerated from 16 ps to 10 ps.

6.4.6 Polarization-sensitive 2D-IR results

The reorientation timescales in our system of study are relatively faster than the structural dynamics as measured by the 2D-IR. In this case, reorientation could also be a source

of spectral diffusion. To quantify the the effect of reorientation-induced spectral diffusion (RISD)[230,231,252], we performed another set of 2D-IR experiment with ZZXX (perpendicular) polarization.

The ZZXX data, when compared with ZZZZ data shows faster apparent dynamics. The IL-AOT system has a faster decay and significantly smaller constant offsets. The $[C_4C_1im][SCN]$/ BHDC and $[C_4C_1im][SCN]$/ TX-100 system also show acceleration in the apparent dynamics. The fitting further supports this result (Table 6).

As described above, the discrepancy in dynamics of the different polarization configurations is a sign of reorientation-induced spectral diffusion. If the reorientation of the vibrational probe is relatively faster than complete structural reorganization of the local environment, and the interaction with the vibration has a vectorial component (e.g. a Stark effect), then the relative orientation of the probe to the local environment will contribute to the instantaneous frequency. In our system, the reorientation of thiocyanate molecule is faster than the slower structural dynamics, and is therefore expected to be affected by RISD.

Typically, the ZZXX configuration will have faster apparent dynamics than the ZZZZ configuration. This is because at early times, ZZXX is measuring those molecules that have rotated significantly. If the reorientation causes the frequency to change, then ZZXX more likely samples those molecules that experience bigger frequency change, and thus shows less frequency correlation. ZZZZ, on the other hand, more likely samples molecules that retained their orientation, which then results in more frequency correlation. When the orientation of the dipole is isotropic and reorientation is complete, the ZZZZ and ZZXX signal is expected to be identical, which is the case for TX-100 and BHDC systems. The AOT system, on the other hand, shows a significant discrepancy between the ZZZZ and ZZXX configuration even after the reorientation is complete. This phenomenon is very likely due to a non-isotropic orientation distribution of molecular dipoles in its local electric field.

6.5 DISCUSSION

6.5.1 The dynamics data contradicts the "IL-RM" hypothesis for small diameter cases

Previous literature often refers the ionic liquid-surfactant complex as a reverse micelle. Crucial evidence to determine the reverse-micelle formation is the positive linear relationship between the W value and size. For reverse micelles, as the W value increases, the measured diameter of the particle should increase linearly. DLS measurements on $[C_4C_1im][NTf_2]$ and $[C_4C_1im][BF_4]$ in various systems shown this behavior, and IL-surfactant complexes are therefore considered reverse micelles.

On the other hand, reverse micelles also have other distinct features. In general, when a molecule is placed near a surface, it will adopt a solid-like structure that has significant slow dynamics compared to the bulk. This find has been shown by Fayer and co-workers [18,19,22,253] that when water is entrapped in a small reverse micelle, the reorientation dynamics and the structural dynamics are both greatly slowed. It has also been shown that the solvent has negligible effects on the entrapped liquid molecules. In the case of water, the FTIR peak shape and reorientation timescale are identical after switching the solvent from CCl_4 to isooctane[19].

Our polarization-controlled 2D-IR experiment then adds valuable insight into the actual microscopic structure of the IL-surfactant complexes. We will show that, though in certain aspects, the experiment observations are consistent with the RM hypothesis, the major dynamics are not supporting a reverse-micelle formation scenario in $[C_4C_1im][SCN]$/ surfactant systems.

Our experiment supports the fact that $[C_4C_1im][SCN]$ and surfactants form microscopic structures. To help the ionic liquid to dissolve in the organic solvent, surfactants could potentially play two roles: the first is to change the co-solvent that changes the macroscopic properties of the solvent, which is to act as a co-solvent; the second is to change the micro-

scopic environment of the solute, which is to form complexes with the solute. The difference between the two lies in the fact that for the former case, the solubility of ionic liquids depends on the absolute concentration of the surfactant, while in the latter case depends on the IL-to-surfactant concentration ratio, or the W value. During our sample preparation, we have seen a strong dependence of W value, rather than the surfactant concentration, indicating the surfactant is forming complexes with the IL. This is consistent with previous research.

We consider our $[C_4C_1im][SCN]$ complexes to be of comparable sizes of $[C_4C_1im][NTf_2]$ complexes. Our DLS experiment received very weak signal around 2 nm diameter, and no signal at 20nm. The DOSY experiment, while showing a different trend, reports a size similar to the previous DLS results on $[C_4C_1im][NTf_2]$.

We will show here that our 2D-IR results do not support the hypothesis of reverse-micelles. We hypothesize that the IL-surfactant complex with $[C_4C_1im][SCN]$ is more likely to be a small cluster.

The reorientation motion of SCN^- is diffusive and fast, so should not be in the reverse micelles. The anisotropy decay can be fitted to a single exponential, indicating the thiocyanates diffusively rotating in the complex. When a molecule nears the surfactant shell in reverse micelles, the reorientation dynamics will be greatly hindered. For example, the shell water in water reverse micelles has a reorientation time of 110 ps[253]. Our measurements do not show this behavior. An average timescale of ~8 ps in chlorobenzene is qualitatively different from the reorientation dynamics in pure TX-100, which is more than 50 ps (Supporting information). The reorientation time is even faster than SCN^- in common ionic liquids[119]. The time constants are sensitive to neither W value nor type of surfactants, indicating that the reorientation is very likely to be the reorientation of thiocyanate itself, not the entire cluster. Moreover, the timescale of thiocyanate reorientation in such complexes is similar to the thiocyanate ion reorientation time in water, indicating a relatively free local environment in IL-surfactant complexes[254].

Both reorientation dynamics and structural dynamics of thiocyanate in these systems are

highly solvent-dependent. Switching from chlorobenzene to dichloromethane, the dynamic timescales are almost halved for all the systems. Since the pattern qualitatively matches the viscosity ratio between the two solvents, the evidence of solvent directly affecting the dynamics of thiocyanate is clear. If the thiocyanate ion was completely surrounded by surfactant, we would expect the dynamics to be relatively less affected by the solvent[19], which is contrary to the experimental observation.

The structural dynamics of $[C_4C_1im][SCN]$-TX-100 system are significantly different from the dynamics of $[C_4C_1im][SCN]$ in bulk TX-100 (Supporting information). In pure TX-100, the $[C_4C_1im][SCN]$ dynamics are significantly slower and the reorientation dynamics are an order of magnitude slower than that in the organic solvents. If the IL is completely surrounded by the TX-100, as in reverse-micelles, we would expect more similar dynamics with the bulk TX-100 experiment.

Based on the above analysis, our experimental results do not support the hypothesis of reverse micelle formation for $[C_4C_1im][SCN]$/surfactant/solvent systems.

6.5.2 ILs and surfactants form small clusters

We hypothesize that $[C_4C_1im][SCN]$ forms small clusters with surfactants in the organic solvents. The ionic liquids are moving macroscopically together with the clustered surfactants, and the surfactant may adopt a structure to "exclude" the effects of the solvents and affect the dynamics of the ILs in its own manner. At the same time, however, the ILs are still exposed to the solvent and have enough degrees of freedom to rotate.

The reversed size-dependence, as revealed by DOSY experiments, could possibly be explained by the partition ratio. When the W value is small, such as W = 0.25, for each IL ion-pair, there are four surfactants. If we assume that each cluster contains only one IL formula-unit, then the smallest possible cluster that the system could form contains 4 surfactants. As the W value increases to W = 0.5 for example, the smallest cluster is reduced to contain only 2 surfactants. The size of the cluster is therefore decreasing in size as W

value increases. It is possible that the DOSY experiment is reporting a summation of the dynamics of the cluster and the dynamics of the ionic liquid, and renders the size estimation inaccurate. Even if this is the case and the actual size dependence follows the same trend as the reverse micelles, it could still be explained by clusters with multiple formula-units of ILs.

As mentioned in the previous subsection, the reorientation dynamics could be readily explained by the hypothesis. Since ILs and surfactants are forming clusters rather than reverse micelles, the ILs are not completely surrounded by the surfactants, and is exposed to the solvents surroundings. This structure allows the ionic liquids to reorient diffusively and causes the reorientation dynamics to be greatly affected by the properties of the solvents.

There are two possible sources that cause the dependence of the structural dynamics on the surfactant. The ion-exchange mechanism has been proposed by previous research[240,247] based on the H^1NMR experiments in BHDC. Our NMR results of the BHDC system replicates the feature. If the surfactants are ionic, then the surfactant ions may exchange partners with the ions from the ionic-liquids. For the case of BHDC, it is possible that the chloride moves closer to the $[C_4C_1im]$ cation, and causes the chemical shift. For our AOT experiments, a significant static component is observed. This is possibly another piece of evidence of ion exchange between the sodium cation and $[C_4C_1im]$. There are observations of static components that are caused by the KSCN or KSeCN ion pairs[251,255], which is a similar situation to ion-exchange. Another possibility is that the structure of the surfactant dominates the dynamics of clustered ionic liquids. The three examined surfactants have very different structures; AOT has two aliphatic tails, TX-100 is a poly-ether in nature and and BHDC has an asymmetric structure with both a relatively small phenyl group and a long aliphatic tail. The real scenario could also be a interplay of the two possible sources and therefore requires further study.

It is worth noting that though our hypothesis contradicts the idea of small-sized reversed micelles in $[C_4C_1im][SCN]$, it is possibly IL-specific. The solubility data presented shows that the formation of IL-surfactant clusters are IL-dependent, indicating that the formation

process could be affected by the properties of the cation and anion of the ionic liquid. $[C_4C_1im][BF_4]$, for example, has an ion that is chemically very different from either $[NTf_2]$ or [SCN]. Prior experiments have found that $[C_4C_1im][BF_4]$ forms much bigger complexes than $[C_4C_1im][SCN]$, which strongly indicates that the structure of that complex could be very different from what we observed in our experiments. It is more plausible to consider that the $[C_4C_1im][BF_4]$ forms reverse micelles than small clusters. It is also possible that $[C_4C_1im][NTf_2]$ also adopts a different micro-structure than $[C_4C_1im][SCN]$, which could be supported by the discripancy of size-dependence of the two systems.

Nevertheless, our experiments suggest a different micro-structure that the ionic liquids could form with surfactants in the organic solvents. In this small cluster, ionic liquid dynamics are greatly affected by the choice of surfactants and the solvents. The reorientation is mostly diffusive and the timescale is close to water.

6.5.3 A possible ion-exchange mechanism revealed by polarization-sensitive 2D-IR

The discrepancy between ZZZZ and ZZXX configurations for our polarization-sensitive 2D spectra is apparent for all of the systems tested. This is not surprising for our system because the reorientation time in these systems are shorter than the structural reorganization time. In this scenario, the local electric field relaxes more slowly than the rotational motion of the chromophore. When the molecules reorient with respect to the local electric field, their instantaneous frequency could fluctuate through effects such as the Stark effect, which causes reorientation induced spectral diffusion (RISD).

What is surprising, however, is the discrepancy of the two configurations in AOT samples. At long times, the static components of ZZZZ and ZZXX configurations do not vanish to zero, and are very different from each other. The previous theory of RISD[230,231] predicts that when the reorientation is complete, the RISD of any polarization configuration should vanish to zero. The theory prediction and the AOT results are directly contradiction to each other.

We interpret this long-lived discrepancy as a non-isotropic distribution of thiocyanate in local electric field. As shown in our recent paper, when a strong local electric field is present, the molecule's potential energy will vary as a function of the angle between the dipole moment and the local electric field. The difference in potential energy will then generate a non-isotropic distribution of molecular dipoles. In this case, when we probe our system with ZZZZ polarization, it is more likely probing those molecules that did not shift their frequencies due to reorientation much, indicating a higher frequency-frequency correlation; on the other hand, if probing in the ZZXX configuration, those molecules which drastically changed their frequencies are probed, yielding in total a lower correlation.

If our theory is correct, the existence of the strong electric field indicates a potential ion-exchange mechanism. In order to drive the angular distribution of dipoles away from isotropic, a strong electric field is required. In our system, there are three types of ions other than SCN, namely Na^+, $[C_4C_1im]$ and AOT^-. AOT^- is big and negative in charge, and is then very unlikely to get very close to SCN^-. When comparing $[C_4C_1im]$ with Na^+, though their net charge is the same, Na^+ is much smaller in size. Since SCN^- is a small anion, it is very likely to attract a small cation. Thus, the ion-exchange between Na^+ and $[C_4C_1im]$ increases the local electric field strength.

A simple calculation shows that the energy difference induced by Na^+ could be as big as $16k_BT$, while according to our model, $2k_BT$ is sufficient to reproduce the data. Recently, research shows that K^+ and SCN^- form ion-pairs in $[C_2C_1im][NTf_2]$, and upon the formation, similar long-lived discrepancy is observed in that system[255]. With the evidence added above, it is reasonable to attribute the large local electric field to the ion-exchange mechanism. Moreover, the ion-exchange should not happen in TX-100 and BHDC systems, since they lack small cations. This is consistent with the experimental results.

This is not the first evidence presented of an ion-exchange mechanism. Based on the H^1NMR study of 2-position hydrogen chemical shift in $[C_4C_1im][NTf_2]$/BHDC system, a similar ion-exchange is considered to happen between $[NTf_2]$ and BHDC[240]. We would also expect that, if our probe were a small cation, the phenomenon would be happen in the

BHDC system.

6.6 CONCLUSIONS

In summary, we used $[C_4C_1im][SCN]$ as our vibrational probe to study the structural and reorientation dynamics of ionic liquid-surfactant complexes. We found that the IL dynamics are dependent on several different factors, including the surfactants, the solvent and the IL-to-surfactant ratio. The anisotropy experiment shows accelerated dynamics of ∼8 ps, which is comparable to free thiocyanate ion in water, and is less dependent on the surfactant or the W value but highly dependent on the solvent. The structural dynamics are greatly affected by the choice of surfactants: while the anionic surfactant AOT creates a semi-static microscopic environment the slows down the dynamics, the non-ionic surfactant TX-100 creates a dynamic microscopic environment that accelerates the dynamics, and the cationic surfactant BHDC creates an intermediate environment. The structural dynamics are also affected by the W value, as well as the choice of solvents. A clear RISD effect is observed due to fast reorientation dynamics and slow structural dynamics. The result strongly indicates that $[C_4C_1im][SCN]$ is not forming reverse micelles in the system, but is instead forming small IL-surfactant clusters. In the cluster, the thiocyanate ion is close to the surfactant, but could still have close interaction with the solvent, and has enough degrees of freedom to rotate. The results also show that 2D-IR spectroscopy is a useful tool to understand the dynamics of IL in micro-structures, and opens opportunity to control the reactivity of these IL-surfactant nano-reactors.

7.0 REORIENTATION-INDUCED SPECTRAL DIFFUSION OF NON-ISOTROPIC ORIENTATION DISTRIBUTIONS

The text in this chapter has been adapted from Ren, Z.; and Garrett-Roe, S. *J. Chem. Phys.* **2017**, *147*, 144504. The author's contribution to this work included designing the study, derving the mathimatical equations, conducting calculations and writing the manuscript.

7.1 CHAPTER SUMMARY

When reorientation of a vibrational chromophore is faster than the relaxation of its local environment, the frequency fluctuation correlation function (FFCF) measured by 2D-IR spectroscopy is an interplay of scalar structural spectral diffusion (SSD) and vectorial reorientation-induced spectral diffusion (RISD). Theory has been established to calculate the RISD component of different polarization configurations with the assumption that the molecule orients randomly in a local electric field. We show here that in the $[C_4C_1im][SCN]$/AOT/chlorobenzene system, where the local electric field is strong, this assumption is incapable of reproducing the experimental results. We modify the current theory by assuming a Boltzmann distribution of transition dipoles of the chromophores in a local electric field, and use a Markov chain model to calculate the RISD component of 2D-IR with different polarization configurations. The result reproduces key features of the experiment, and suggests a potential ion-exchange in the $[C_4C_1im][SCN]$/AOT/chlorobenzene system.

7.2 INTRODUCTION

Two dimensional infrared spectroscopy (2D-IR) is a powerful tool to interrogate the structural dynamics of complex condensed phase systems[1,11,123,129,152,248,249,256–258]. The instantaneous vibrational frequency of a probe molecule is sensitive to its local environment. As the local environment changes, the frequency changes accordingly, leading to a random walk in frequency space called spectral diffusion. The rate of this process can be extracted from 2D-IR experiments in terms of the frequency fluctuation correlation function (FFCF)[1,259]

$$c_2(t) = \langle \delta\omega(0)\delta\omega(t) \rangle, \tag{7.1}$$

where $\delta\omega(0)$ and $\delta\omega(t)$ are the instantaneous frequency fluctuation of initial and final state separated by a waiting time. The angled brackets $\langle \cdots \rangle$ mean an average over the ensemble of molecules.

The instantaneous frequency fluctuation,

$$\delta\omega(t) = \omega(t) - \langle \omega \rangle, \tag{7.2}$$

directly reflects the local environment of the chromophore. Normally, there are two sources contributing to this quantity: the scalar component $\omega_s(t)$ and the vectorial component $\omega_p(t)$[230,231]. The former reflects the isotropic structural dynamics such as density fluctuation, the latter comes from the orientation of the probe molecule. The local environment generates a non-zero local electric field, and the vibrational frequency of the probe molecule is modified by it via effects such as the Stark effect.

The measured FFCF is then composed of two components: structural spectral diffusion (SSD), which is the result of the scalar frequency fluctuation, and reorientation-induced spectral diffusion (RISD)[252], which comes from the reorientation of the molecule. Since the RISD is vectorial, its effect on spectra depends on the polarization of the laser pulses in the experiment. Considering the two effects together, the measured FFCF not only reports both SSD and RISD at the same time, but it also changes between different polarizations of the incident laser pulses.

In many systems, the timescales for probe reorientation and structural fluctuation are separated[260–263]; however, in certain systems such as ionic liquids, the timescales are similar[25,226,255,264,265]. To interpret the dynamics in these systems unambiguously, it is necessary to separate the RISD and SSD components.

Fundamental theory to treat this problem has been established by Fayer and co-workers[226,230,231]. By assuming a Stark effect, the theory gives a mathematical formulation of the RISD component under various polarization configurations for either diffusive reorientation or wobbling-in-a-cone. The theory reduces the total FFCF into a product of the RISD and SSD components. The theory shows quantitative agreement with the experimental 2D-IR of ionic liquids.

Recently, however, our 2D-IR spectra of an ionic liquid-surfactant complex system report a situation that cannot be explained by the current model. In our experiment, 1-butyl-3-methylimidazolium thiocyanate ($[C_4C_1im][SCN]$) and docusate sodium (AOT) form colloidal dispersions in chlorobenzene[266]. The thiocyanate anion undergoes a diffusive reorientation that completes within 10 ps. According to the theory, the RISD component should vanish after full randomization of orientation is achieved, and the total FFCF reported by different polarizations configurations should be the same at long waiting times. On the contrary, we observe that the total FFCF has a significant static component even at 150 ps, and the value is significantly different between different polarization configurations.

In this article, we will expand the current theory to explain this intriguing phenomenon. When considering the interaction energy of molecular dipoles in the local electric field, the molecules should not adopt an isotropic orientation distribution as assumed in the original theory. We will show that, when assuming a Boltzmann distribution of molecular orientation in the local electric field, the RISD component will not vanish at long times. It will instead have definite static value that is a function of polarization configuration. This extension of the theory of RISD qualitatively explains the phenomenon that we have encountered.

7.3 THEORY

We begin with a few key steps of the previous derivation. First, the total FFCF observed with 2D-IR can be written as a product of the SSD and RISD, with a possible additive SSD term that does not originate from vectorial interactions

$$c_2(t) = R_p(t) \cdot F(t) + C_s(t). \tag{7.3}$$

Here, $R_p(t)$ stands for the RISD term with polarization configuration p, and $F(t)$ is the SSD term indicating the local electric field fluctuation. $C_s(t)$ is given by the isotropic ensemble average. Considering that both $F(t)$ and $C_s(t)$ originate from the SSD and are independent of polarization configuration, the main focus of this paper is the $R_p(t)$ term.

We adopt polarization-weighted frequency fluctuation correlation function (PW-FFCF) as introduced in the previous theory to calculate the RISD term:

$$R_p(t) = \langle \delta\omega(0)\delta\omega(t) \rangle_p = \sum_i P_i^p(t)\delta\omega_i(0)\delta\omega_i(t) \tag{7.4}$$

with the summation over all molecules. $P_i^p(t)$ is the polarization weight of the i-th molecule under polarization configuration $p = \alpha\alpha\beta\beta$, with each α or β representing the polarization of a laser pulse

$$P_i^{\alpha\alpha\beta\beta}(t) = \frac{(\hat{\epsilon}_\alpha \cdot \hat{\mu}_i(0))^2 (\hat{\epsilon}_\beta \cdot \hat{\mu}_i(t))^2}{\sum_j (\hat{\epsilon}_\alpha \cdot \hat{\mu}_j(0))^2 (\hat{\epsilon}_\beta \cdot \hat{\mu}_j(t))^2}, \tag{7.5}$$

where $\hat{\epsilon}_\alpha$ is the unit vector of electric field with α polarization and $\hat{\mu}_i(t)$ stand for the unit vector of the transition dipole moment of ith molecule at time t. The denominator is the normalization constant.

It is worth noting that PW-FFCF could also be applied to the SSD terms but yields no change. Polarization weight will be factored out from the instantaneous frequency fluctuation term due to orthogonality. It is also worth mentioning that if no structural relaxation exists (SSD terms are constant and equal to one), the $R_p(t)$ will be the exact quantity that a 2D-IR experiment gives.

Similar to the previous treatment, we here assume that the vectorial frequency fluctuation is purely determined by the first-order Stark effect[267],

$$\delta\omega(\Omega_F(t)) = \delta\vec{\mu}(t) \cdot \vec{E} = \lambda E \cos(\theta_F(t)), \tag{7.6}$$

where $\delta\vec{\mu(t)}$ is the difference in the dipole moment between the vibrational excited state and the ground state, $\vec{E}$ is the local electric field, and E is the field magnitude. λ stands for the Stark tuning rate, and $\Omega_F(t) = (\theta_F(t), \phi_F(t))$ represents the angular parameter. $\theta_F(t)$ means the angle between the local electric field and the molecular dipole moment. The subscript F indicates the 'field frame', where the local electric field is aligned along the Z axis of that coordinate system.

If we assume the ensemble of molecules is large enough, the summation in Eq. 7.4 becomes integrals of probability density over all the possible orientations. In this system, there are three orientations, namely the initial and final orientation of the molecule in the field frame ($\Omega_F(0)$ and $\Omega_F(t)$, respectively), and the orientation of the local electric field (Ω'_F). The probability density could be given as $p(\Omega'_F)p(\Omega_F(0)p(\Omega_F(0)|\Omega_F(t), t)$, with $p(\Omega_F(0))$ the equilibrium distribution of dipoles in the field frame, $p(\Omega_F(0)|\Omega_F(t), t)$ the conditional probability of finding the final orientation $\Omega_F(t)$ at t given the initial orientation $\Omega_F(0)$, and $p(\Omega'_F)$ the probability of finding the electric field oriented at Ω'_F in the lab frame.

Given the above information, the PW-FFCF from Eq. 7.4 now is a multiple integral over initial and final orientation of the molecule in the field frame, as well as the orientation of the local electric field. The integrand is a multiplication of the probability of finding the molecule in a certain local electric field orientation with certain initial and final orientation, the polarization weight (Eq. 7.5) and the initial and final instantaneous frequency fluctuation (Eq. 7.6):

$$R_{\alpha\alpha\beta\beta}(t) = \frac{C_A}{I_{\alpha\alpha\beta\beta}(t)} \int d\Omega'_F \int d\Omega_F(t) \int d\Omega_F(0) p(\Omega'_F)(\hat{\epsilon}_\alpha(\Omega'_F) \cdot \hat{\mu}_i(\Omega_F(t)))^2 p(\Omega_F(0)) \\ \times p(\Omega_F(0)|\Omega_F(t), t)(\hat{\epsilon}_\beta(\Omega'_F) \cdot \hat{\mu}_i(\Omega_F(t)))^2 \delta\omega(\Omega_F(t))\delta\omega(\Omega_F(0)). \tag{7.7}$$

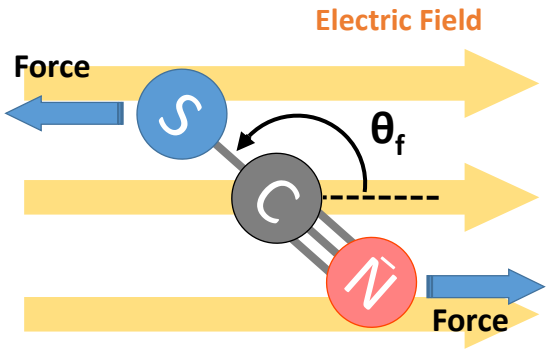

Figure 22: The presence of an external local electric field makes the molecule favors certain orientations over others.

C_A is the multiplication of prefactors of the integrals. $I_{\alpha\alpha\beta\beta}(t)$ is the intensity observable that serves as a normalization constant here,

$$I_{\alpha\alpha\beta\beta}(t) = C_A \int d\Omega'_F \int d\Omega_F(t) \int d\Omega_F(0) p(\Omega'_F)(\hat{\epsilon}_\alpha(\Omega'_F) \cdot \hat{\mu}_i(\Omega_F(t)))^2 \times p(\Omega_F(0)) p(\Omega_F(0)|\Omega_F(t), t)(\hat{\epsilon}_\beta(\Omega'_F) \cdot \hat{\mu}_i(\Omega_F(t)))^2. \quad (7.8)$$

If the distribution of dipole moments in the field frame is considered isotropic, the following analytical expression for pure diffusive reorientation can be obtained[230]:

$$\begin{aligned} R_{ZZZZ}(t) &= \frac{3}{25}\left[\frac{11C_1(t) + 4C_3(t)}{1 + 0.8C_2(t)}\right], \\ R_{ZZXX}(t) &= \frac{3}{25}\left[\frac{7C_1(t) - 2C_3(t)}{1 - 0.4C_2(t)}\right], \end{aligned} \quad (7.9)$$

with $C_l(t) = \exp(-l(l+1)Dt)$, where D is the orientation diffusion coefficient. In this scenario, reorientation causes the RISD term to decrease monotonically. When the time is sufficiently long, both ZZZZ and ZZXX terms vanish at 0.

The presence of a local electric field drives the orientation distribution of the molecules in the field frame away from isotropic, since the interaction between the electric field and

the dipole of the molecule favors certain orientations over others (Figure 22). The energy of interaction is given by

$$U = \vec{E} \cdot \vec{\mu} = E\mu \cos(\theta_F). \tag{7.10}$$

where μ is the magnitude of the dipole moment. At equilibrium, the dipoles in the field frame adopt a Boltzmann distribution

$$p(\Omega_f) = \frac{e^{-\beta \cos(\theta_F)}}{G_A}. \tag{7.11}$$

Here $\beta = E\mu/k_BT$ is a measure of the strength of the electric field-dipole interaction, with k_B representing the Boltzmann constant, and G_A is the normalization constant. Similarly, the rate of transitions along the θ_F-axis is also biased due to the energy difference, which modifies $p(\Omega_F(0)|\Omega_F(t), t)$ in Eq. (7.7) to maintain detailed balance.

Here we apply a simple Markov chain model to numerically calculate $R_p(t)$ with the non-isotropic distribution of orientations. We split the two angular coordinates describing the orientation of the dipole moment in the laboratory frame ($\theta \in [0, \pi], \phi \in [0, 2\pi]$) each into 16 discrete sections (Figure 23). When combined together, 256 discrete microscopic orientation states exist. The spherical coordinates of each state are represented by the central point of the state. Each state is denoted as $\Omega(\Theta, \Phi)$, with $\Theta \in [1, 16]$ being the section number on θ degree of freedom, and $\Phi \in [1, 16]$ being the section number on ϕ degree of freedom.

The one-step transition matrix $\mathbf{T^1}$ contains the full information to describe the probabilistic evolution of orientation distribution, once the time is discretized. This matrix is a $N \times N$ matrix, where N is the total number of microstates. Each element $T^1_{ij} = p^1(\Omega_i|\Omega_j)$ of the matrix is the conditional probability of diffusing from state Ω_i to state Ω_j in one time step (the superscript). The summation of all the elements of each column is 1 to conserve probability. In our model, $\mathbf{T^1}$ describes the orientation diffusion process of the chromophore as a function of time, which is the information needed to calculate the PW-FFCF as well as the anisotropy.

The diffusive reorientation process obeys the detailed balance condition, which means that at equilibrium, the probability exchange between each two states should be equal to

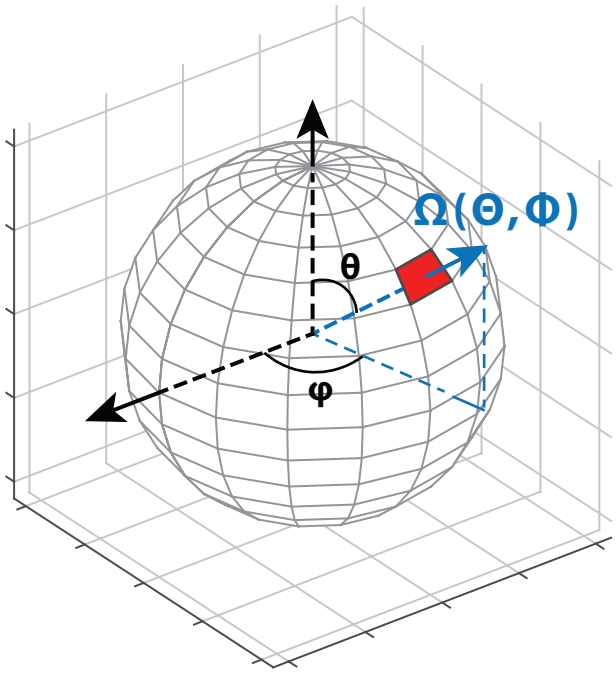

Figure 23: The sphere is discretized into 256 microscopic states, each is represented by $\Omega(\Theta, \Phi)$. The coordinate of each state is given by the central point.

each other

$$p(\Omega_i)p^1(\Omega_i|\Omega_j) = p(\Omega_j)p^1(\Omega_j|\Omega_i). \tag{7.12}$$

Moreover, since the equilibrium distribution of each state is determined by the Boltzmann distribution, it leads to

$$\frac{p^1(\Omega_i|\Omega_j)}{p^1(\Omega_j|\Omega_i)} = \frac{p(\Omega_j)}{p(\Omega_i)} = \frac{e^{-\beta\cos(\theta_F(\Omega_j))}}{e^{-\beta\cos(\theta_F(\Omega_i))}}. \tag{7.13}$$

The above equation shows that the off-diagonal elements of the one-step transition matrix are just Boltzmann distribution times a constant. The diagonal element is calculated by 1 minus all off-diagonal elements of the same column.

The transition matrix must accommodate two physical processes, diffusion and drift. Approximate propagators for unbiased diffusion on a sphere have been derived[268,269]. We use the heat kernel expansion, which gives the probability of diffusing an angle θ in time τ as

$$p^{\mathrm{HKE}}(\theta,\tau) = \frac{1}{\tau}\left(1 + \frac{\theta^2}{12} + \cdots\right)\exp(-\theta^2/2\tau). \tag{7.14}$$

Here the time, τ, is a reduced time, $\tau = 2Dt$, where D is the orientational diffusion coefficient. The drift term is determined by the detailed balance condition (Eq. 7.12). The one step transition matrix then becomes

$$T_{ij} = p^{HKE}(\mathcal{D}(\Omega_j,\Omega_i),\tau)\exp(-\beta\Delta E_{ij}/2) \tag{7.15}$$

for a step time τ, where $\mathcal{D}(\Omega_j,\Omega_i)$ is the absolute difference in polar angles of microstates Ω_f and Ω_i, the energy difference $\Delta E_{ij} = \cos(\mathcal{D}(\Omega_j,\Omega_F)) - \cos(\mathcal{D}(\Omega_i,\Omega_F))$, and Ω_F is the coordinates of the instantaneous electric field.

Once the $\mathbf{T^1}$ is determined, the information about the reorientation process is complete. For example, the N-step transition matrix could be constructed by multiplying $\mathbf{T^1}$ N times,

$$\mathbf{T^N} = \mathbf{T^1}^N. \tag{7.16}$$

This new transition matrix could be used to determine the orientation distribution after N time steps given an arbitrary initial distribution,

$$\vec{\Pi}(N) = \mathbf{T^N} \cdot \vec{\Pi}(0). \tag{7.17}$$

The eigenvector of $\mathbf{T^1}$ is the equilibrium distribution of the reorientation,

$$\vec{\Pi}_{eq} = \mathbf{T^1} \cdot \vec{\Pi}_{eq}, \tag{7.18}$$

and in our case, should be the same to the distribution that is given by the Boltzmann distribution.

$$R_{\alpha\alpha\beta\beta}(N) = \frac{C_A}{I_{\alpha\alpha\beta\beta}(N)} \sum_{\Omega(0),\Omega(N),\Omega'} p(\Omega')(\hat{\epsilon}_\alpha(\Omega') \cdot \hat{\mu}_i(\Omega(N)))^2 \delta\omega(\Omega(N)) p(\Omega(0)) \\ p^N(\Omega(0)|\Omega(N))(\hat{\epsilon}_\beta(\Omega') \cdot \hat{\mu}_i(\Omega(0)))^2 \delta\omega(\Omega(0)). \tag{7.19}$$

It is then possible to rewrite Eq.7.7 with respect to the developed Markov model (Eq. 7.19). The time dependence becomes the time step dependence. Integrals become summation over all the possible states of the electric field (Ω'), initial orientation ($\Omega(0)$) and final orientation ($\Omega(t)$). The denominator is the time-dependent intensity normalization factor. Now we will derive each term from the Markov model.

With isotropic media, the local electric field is also isotropic with respect to the lab frame

$$p(\Omega') = \frac{A(\Omega')}{4\pi^2}, \tag{7.20}$$

where $A(\Omega')$ is the area of the microstate on a unit sphere.

Since the RISD component is now written in the lab-frame, the polarization weight is therefore merely a function of the microscopic state, and is given by

$$\begin{aligned} (\hat{\epsilon}_Z(\Omega') \cdot \hat{\mu}_i(\Omega(N)))^2 &= \cos^2\theta, \\ (\hat{\epsilon}_X(\Omega') \cdot \hat{\mu}_i(\Omega(N)))^2 &= \sin^2\theta\cos^2\phi, \end{aligned} \tag{7.21}$$

where θ and ϕ are the spherical coordinates of a microscopic state.

$p(\Omega(0))$ is the equilibrium probability for a molecule to orient at $\Omega(0)$ with the local electric field orienting at Ω', which is the corresponding element of the Boltzmann distribution.

$p^N(\Omega(0)|\Omega(N))$ stands for the conditional probability that the molecule orients at $\Omega(0)$ at time 0 and $\Omega(N)$ after N time steps given local electric field orienting at Ω'. It is given by the corresponding element of the N-step transition matrix.

The $I_{\alpha\alpha\beta\beta}(N)$ is the intensity observable

$$\begin{aligned} I_{\alpha\alpha\beta\beta}(N) = \sum_{\Omega(0),\Omega(N),\Omega'} & p(\Omega')(\hat{\epsilon}_\alpha(\Omega') \cdot \hat{\mu}_i(\Omega(N)))^2 \\ & \times p(\Omega(0))p^N(\Omega(0)|\Omega(N))(\hat{\epsilon}_\beta(\Omega') \cdot \hat{\mu}_i(\Omega(0)))^2. \end{aligned} \tag{7.22}$$

In addition to the normalization factor, $I_{\alpha\alpha\beta\beta}(N)$ also gives the anisotropy

$$A(N) = \frac{I_{ZZZZ}(N) - I_{ZZXX}(N)}{I_{ZZZZ}(N) + 2I_{ZZXX}(N)}. \tag{7.23}$$

7.4 RESULTS AND DISCUSSION

The orientation diffusion of a single molecule can be probabilistically determined with our model (Figure 24). To illustrate the time-evolution in our model, we let a molecule orient near the top of the sphere near the lab-frame z-axis. At very short time, the molecule can only diffuse to states that are near the pole ($N = 1$). Given more time, the probability distribution gradually diffuses toward the entire sphere but still retains some memory of the initial orientation ($N = 20$). Given sufficiently long time, the molecule completely reorients itself, loses all the information of the initial orientation, and the probability distribution becomes the Boltzmann distribution ($N = 200$, Boltzmann). With a non-zero external electric field intensity, the final distribution is also different. Without the field, the final distribution is isotropic; with the electric field, the molecule is more likely to orient toward the direction of the field. The above features are expected by the physical interpretation of reorientation, which validates our model.

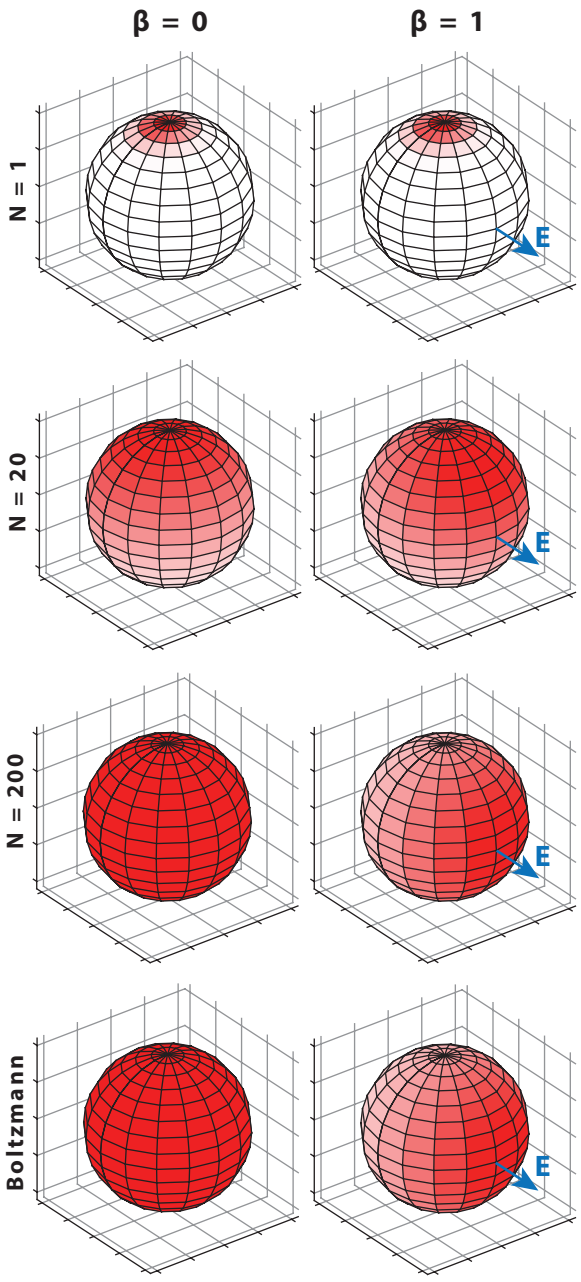

Figure 24: The propagation of probability distribution with (right) and without (left) external local electric field. The initial distribution is very close to the top of the sphere ($N = 1$) and gradually diffuses toward the equilibrium distribution ($N = 20$). With sufficiently many time steps ($N = 200$), the final distribution becomes the Boltzmann distribution. Each time step is $\tau = 0.05$ in reduced units.

When β value is set to zero, indicating that the ratio of the interaction energy, $\vec{E} \cdot \vec{\mu}$, to the thermal energy, $k_B T$, is very small, the system reduces to the previous model[231], and our treatment of the anisotropy and response functions shows quantitative agreement with it (Figure 25). For both approaches, the normalized anisotropy starting at 1 and gradually decays to 0. The $R_{ZZXX}(N)$ starts at 1, indicating a complete correlation, and gradually decays to 0, but at a slower rate compared to the anisotropy decay. The $R_{ZZZZ}(N)$ has the slowest correlation decay because it is weighted towards molecules which do not reorient. Conversely, the $R_{ZZXX}(N)$ has the fastest correlation decay, because it is weighted towards molecules which reorient and, hence, change their vibrational frequency. The isotropic signal is, essentially, the weighted sum of both ZZZZ and ZZXX configuration, and is therefore in the middle. In spite of the difference in decay rate, all the three response functions decay to 0 eventually.

When we introduce a non-zero electric field to the system, $\beta = 1$, the observed trend changes. As the distribution is no longer isotropic, the ZZZZ and ZZXX no longer reach to 0 at long times, they instead have static offsets. The offset for ZZZZ configuration is positive, and is higher than the offset for ZZXX configuration, which is negative. The isotropic response vanishes at long times. On the other hand, the anisotropy no longer decays to zero but remains a small but positive value.

When the local electric field becomes even stronger, the RISD for both configurations have bigger static components, and the discrepancy between the two configurations also increases. As $\beta = 2$, the the ZZZZ configuration is mostly static, with only a small amount of RISD decay happening at early times; while the ZZXX decays to a more negative value, yielding a bigger discrepancy between the two configurations at long waiting time. The isotropic RISD still decays to 0. The anisotropy now has significant portion of static offset, preventing it from vanishing to 0.

From the result, we clearly see that the non-isotropic distribution of molecular dipoles causes a long static component in the FFCF.

The model qualitatively agrees with the experimental data (Figure 26). According to

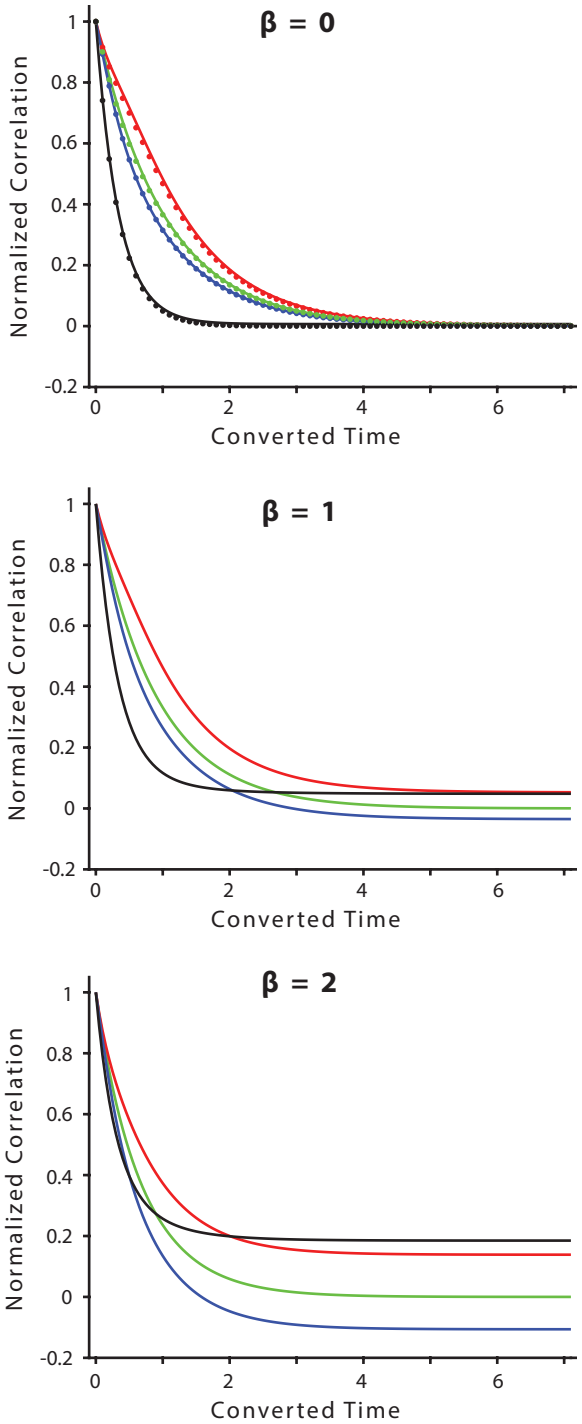

Figure 25: Normalized FFCFs of ZZZZ (red), ZZXX (blue), isotropic (green) as well as the normalized anisotropy (black) are plotted as a function of converted time. When $\beta = 0$, the curves show good agreement with the Fayer's model (dots). As β increases, the FFCFs are no longer merge into each other at long times, and do not vanish to zero.

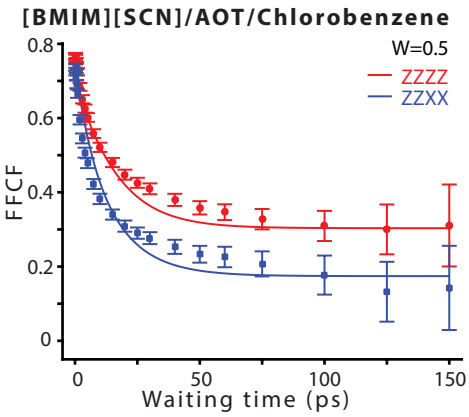

Figure 26: The polarization-controlled experimental data (squares and circles) and model fit (lines) of $[C_4C_1im][SCN]$/AOT/Chlorobenzene system at W = 0.5. With $C_s(t) = 0.23$ and $F(t) = 0.50$, the model agrees qualitatively with the experimental data at long waiting times. Experimental data reproduced from ref.[266] with permission from the PCCP Owner Societies.

Eq. 7.3, we assume that the SSD is static and letting $C_s(t) = 0.23$ and $F(t) = 0.50$. The rotational reorientation time is set to be ~ 8 ps, which is the experimentally determined value. The fitting curve and the experimental curve agrees qualitatively, especially at long waiting times. At short waiting time, the discrepancy is very likely coming from the SSD effect. In the real system, the SSD should not be entirely static, but with some decays as well.

With the model provided above, it is possible to understand the striking discrepancy of FFCF between different polarization configurations in $[C_4C_1im][SCN]$ / AOT / chlorobenzene system. The $[C_4C_1im][SCN]$ and AOT form microscopic emulsions in the organic solvents. When they are both trapped inside the small particle, they can exchange ions with each other. Thiocyanate in $[C_4C_1im][SCN]$ is a small ion, and it will attract Na^+ cation in AOT, which is also a small ion, to achieve stronger Coulombic interactions[251,255]. The consequence of this ion-exchange is a much stronger local electric field near the thiocyanate. The SCN^- then adopts a Boltzmann distribution of orientations under this electric field.

The thiocyanate is an anionic probe that attracts small cationic counter-ions, therefore only the anionic surfactant AOT shows a clear static offset. Other types of surfactants, either BHDC or TX-100, do not have this effect since they do not have small cations. If the probe were a small cation, we expect that the cationic surfactant BHDC system would have similar properties as $[C_4C_1im][SCN]$ / AOT system.

Though the dipole of an ion is not uniquely defined, the contribution from reorientation is independent of the choice of coordinate system. For a ion, the dipole moment is not uniquely defined, and is dependent on the choice of the origin of the coordinate system. Depending on the origin, the potential in Eq. 7.10 could be drastically different: for example, the potential is much higher if we set the origin of the dipole on the sulfer atom of SCN ion, than on the carbon atom. We argue that the potential can be isolated into a translational component and a reorientation component, and in the analysis, we focus on the latter, which is independent of the origin of choice.

Note that it is not necessary that the origin of the frequency shift be a true Stark effect. Strong arguments have been made that the frequency shifts of thiocyanate C≡N vibrations depend on charge transfer[8,270–272] and are not a Stark effect. Nevertheless, the thiocyanate C≡N vibrational frequency correlates with the electric field at the carbon[272]. We require only that the frequency shifts be correlated to the orientation of the molecule relative to the local field, even if the frequency shift is mediated by other physical mechanisms.

The calculated RISD component of the total PW-FFCF is the estimated upper limit for the discrepancy of different polarization configurations. According to Eq. 7.3, the full FFCF is the product of the RISD component and the SSD component, indicating that the apparent magnitude of the RISD is directly affected by the rate of the SSD. In principle, the SSD component will not stay perfectly correlated and will decay over time. In addition, the decay of SSD component could potentially cause the electric strength and direction to fluctuate, which will also reduce the magnitude of the RISD component. When the SSD component has spectrally diffused completely, the observed PW-FFCF will also vanish. On the other hand, if the SSD component contains some slowly evolving component that prevents it from

vanishing, at least on the timescale of the experiment, the RISD part will also be preserved and the total FFCF will differ between the two polarization configurations.

In our calculation, the ZZXX configuration yields a negative value at long times when there is a external electric field. This result is surprising at first glance but can be explained by the properties of isotropic signal. The isotropic signal evaluates the RISD with no polarization bias. We assumed that our system is macroscopically isotropic, and therefore the isotropic signal should decay to 0 when the reorientation is complete. In this case, one of the ZZZZ and ZZXX configurations should be negative and the other is positive. Interestingly, this anticorrelation of the ZZXX configuration also shows up in second-order Stark effect [226].

There are other effects contributing to this interesting observation in $[C_4C_1im][SCN]$ / AOT / chlorobenzene systems, but are small compared to the effect of non-isotropic distribution. Restricted reorientation such as 'wobbling-in-a-cone' model describes a situation where the molecule's reorientation is limited by steric effect to certain angular space (the cone) [273,274]. Since the reorientation is incomplete, the anisotropy does not decay to zero, and RISD of different polarization configurations should not merge into each other. In our experiment, similar systems (replacing AOT with TX-100 or BHDC) show complete diffusive reorientation, indicating the steric effect is minor. Second-order Stark effect also generates static offsets in the FFCF. Thiocyanate has a large static dipole moment, so effects like a first-order Stark effect are expected be the dominant contribution.

It is worth noting that, in this model, the probe molecule is considered asymmetric cylindrical in shape ($C_{\infty v}$), which is consistent with the chromophore of the experiment. It simplifies the treatment to only one orientation degree of freedom. In the real situations, the chromophore could be more complicated and could have additional orientation degrees of freedom. In this situation, it is still possible to apply our treatment by splitting the additional rotation axes into segments. Moreover, in our treatment, the two 'dipole moments', namely the permanent dipole moment of the molecule, the transition dipole moment of the vibrational mode, are parallel with each other. This simplifies the calculation since the angle θ in both polarization weight and instantaneous frequency fluctuation is the same. For

more complicated chromophores, these two dipole moments may be different. In such case, the transition dipole moment should be used to calculate the polarization weight, while the static dipole moment should be used to calculate the frequency fluctuation.

Though the focus of this paper is on the diffusive reorientation, the Markov chain model we developed is a general approach to any reorientation scenario in which momentum is not important. The only requirement is a Markovian reorientation process, that is, the future orientation is independent of the past, given the present orientation. With this requirement met, it is always possible to construct a one-step transition matrix that reproduces the features of different types of reorientation. For example, the large-angle-jump mechanism observed in water reorientation process[180], could potentially be modeled by introducing non-zero terms between microstates that are far away from each other. Once the transition matrix is found, the behavior of the RISD component could be numerically obtained by the method given above. Inertial processes can be accommodated by expanding the state space to include momenta, *i.e.* phase-space.

7.5 CONCLUSION

In summary, we expanded the theory of the reorientation-induced spectral diffusion in 2D-IR spectroscopy. Previously, the theory assumed an isotropic distribution of molecular dipoles with respect to a local electric field. In consequence, the theory predicts no long-time discrepancy between ZZZZ and ZZXX polarization configurations after the full orientation randomization is achieved. However, in a recent experiment, we have shown that the 2D spectra of $[C_4C_1im][SCN]$ / AOT / chlorobenzene have a static component at long waiting times and discrepancy between different polarization configurations. This phenomenon could not be explained by the current theory. We then expanded the theory by taking the interaction between the local electric field and the molecular dipole into consideration, which yields a Boltzmann distribution of dipoles. We adopted a Markov chain model to calculate this modification, and we found that with this non-isotropic distribution, the RISD term

for different polarization configurations do not vanish to 0 at long waiting time, and could have different static offsets. Moreover, the anisotropy does not decay to zero when the local electric field exists. Its static offset is positively correlated with the field intensity. These observed features reproduce the qualitative feature of the experimental observation, and indicates a potential ion-exchange mechanism in the experimental system. This approach is likely to be useful in the modeling of vibrational chromophores in surface sensitive linear and 2D spectroscopies.

8.0 CONCLUSIONS

In this thesis, I have investigated the ultrafast structure and dynamics of ionic liquids with 2D-IR spectroscopy.

I have examined the microscopic solvent dynamics and their relation to viscosity of ionic liquid. The linear correlation between the ion-cage lifetime and the macroscopic viscosity indicates that the macroscopic deformation is gated by the microscopic ion network. When KSCN is dissolved in ionic liquid, it does not dissociate into free ions, but instead forms ion-pairs. The ion-pair has lifetime longer than 200 ps and has a Gibbs free energy of $\sim$8 kJ/mol, measured with NaSCN. Water does not distribute randomly in ionic liquids, in the presence of thiocyanate ion, but instead they accumulate around the SCN, introducing heterogeneity to observed thiocyanate dynamics. The ionic liquid under confinement has properties such as fast reorientation dynamics and strong solvent dependence, which indicate that the observed microscopic structure is not reverse micelles but random clusters. From the reorientation analysis, a possible ion-exchange mechanism is also revealed in the colloidal dispersions.

A Markov chain model for reorientation-induced spectral diffusion is developed to understand the reorientation of molecules under strong local electric field. This model provides an unambiguous explanation to the observed static offset in FFCF in various ion-pairing and clustering phenomena. A strong local electric field near the vibrational probe will not only modify the vibrational frequency of the chromophore, but also alter the orientation of the molecule. To achieve a lower energy, the probe tends to reorient its dipole moment toward the electric field, which generates a non-isotropic orientation distribution, which serves as a residual correlation in the FFCF. On the other hand, the reorientation process of the

ion-pair or cluster changes the direction of the local electric field, which causes the offset to gradually vanish. Therefore, the observed static offset is a combination of a relative static local electric field generated by the counter ion and the non-isotropic orientation distribution of the vibrational chromophore.

The developed model will be an excellent tool to analyze the reorientation and structural spectral diffusion in ionic liquids. In the model, we assume no assumption about the reorientation motion, and therefore can calculate different types of reorientation motions that could be happening in the solution system. It has been shown that in various ionic liquid systems, the reorientation process plays an important role in the frequency correlation loss, and therefore the developed model could be a numerical tool to isolate the structural spectral diffusion, providing an unambiguous picture of dynamics in ionic liquids.

For ion-pairs, four types of dynamics are in general interesting: the structural dynamics of the ion-pairs, the reorientation of each ion, the reorientation of the ion-pair, and the ion-pair equilibrium. Previously, on the first type is characterized. To characterize the reorientation time of the ions, polarization-sensitive 2D-IR and the developed Markov chain model can be applied. The reorientation of the entire ion-pair causes the FFCF to eventually decay to zero; the chemical equilibrium between the free ion and the ion-pair shows up on 2D-IR spectra as cross peaks. Due to the limited vibrational lifetime of SCN^-, these two types of dynamics cannot be directly resolved. To tackle this question, we will employ $SeCN^-$ ion, which has a much longer population relaxation time than the SCN^-.

The solute-clustering phenomenon observed with thiocyanate ion and water could have broader impacts on understanding the catalytic behavior of ionic-liquids. If different types organic reactants have chromophores on each of them, the clustering behavior is then directly observable in 2D-IR by checking the presense of cross peaks. It has been found that ionic-liquid media could accelerate a variety of chemical reactions such as click-chemistry of azides. If certain types of solute molecules tend to cluster in the ionic-liquids, the chances for two reactatns to meet in the ionic liquids are then much higher than typical organic solvents. This clustering behavior gives a potential explanation to the catalyitc property of ionic liquids,

and also could be taken advantage of for designing reaction routes.

APPENDIX A

MOLECULAR ORIGIN OF VISCOSITY SUPPORTING INFORMATION

A.1 WATER CONTENT

The water content in all samples was similarly low for all 2D-IR and viscosity measurements. Water content was measured before and after the laser experiments by FTIR spectroscopy. The peak absorbance of the H2O OH stretching-band was used as a vibrational marker of water contamination. In all experiments for all samples the water concentration was determined to be no greater than 150 ppm.

The OH-stretching band was fit by nonlinear least squares to OH-stretch of a $\sim$1 wt % water loaded sample to determine the peak absorption consistent with the presence of water. The peak OD was converted to concentration using the molar extinction of water 100 $M^{-1}cm^{-1}$ (Venyaminov and Prendergast *Analytical Biochemistry* **248**, 234 (1997)). For the $[C_4C_1C_1^2im][NTf_2]$, the peak absorption was 12 mOD, and that gives a total weight of water per liter = 0.20 g/L. This number is then divided by the density of the IL, which is 1.44 kg/L (assuming it to be the same density as $[C_4C_1im][NTf_2]$ as no literature value was found), and gives a weight fraction of $1.4 \times 10^{-4} = 140$ ppm.

For the $[C_4C_1im][NTf_2]$, the peak absorption was 7 mOD, and that gives a total weight of water per liter of 0.13 g/L. This number is then divided by the density of the IL, which

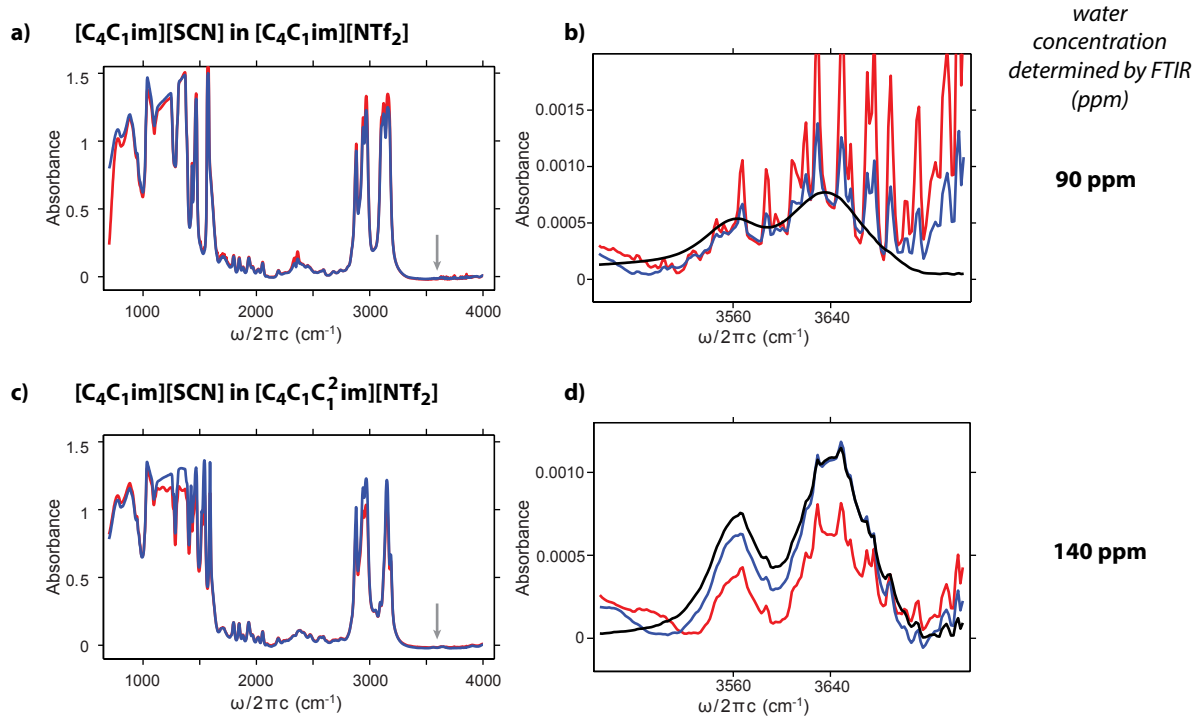

Figure 27: **Determination of water content in the 2D-IR experiments by FTIR spectroscopy. a)** FTIR of $[C_4C_1im][NTf_2]$ shows a nearly flat region in the range of the OH stretch (arrow). **b)** The OH stretch intensity $[C_4C_1im][NTf_2]$ before (red) and after (blue) the 2D-IR experiments was fit by nonlinear least squares to determine the maximum absorbance consistent with H_2O. The 7 mOD absorption corresponds to 90 ppm H_2O. **c)** FTIR of $[C_4C_1C_1^2im][NTf_2]$ also shows a nearly flat region in the range of the OH stretch (arrow). **d)** The OH stretch intensity $[C_4C_1im][NTf_2]$ before (red) and after (blue) the 2D-IR experiments was used to determine the maximum absorbance consistent with the presence of H_2O. The 12 mOD absorption corresponds to 140 ppm H_2O.

Table 7: Water content in samples as determined by Karl Fischer titration. Multiple runs of the same sample on the same instrument show variation on the 50 ppm level. Nevertheless all measurements were in the range of 100 – 300 ppm.

Sample	Run	Water (ppm)
$[C_4C_1im][NTf_2]$	1	207
	2	157
+ 30 mM SCN	1	287
	2	256
$[C_4C_1C_1^2im][NTf_2]$	1	143
	2	173
+ 30 mM $[C_4C_1im][SCN]$	1	227
	2	181

is 1.44 kg/L, which and gives weight fraction of $9 \times 10^{-5} = 90$ ppm.

Water content was also determined by Karl Fischer titration before the viscosity measurements. We determined the water content to be in the range of 140 to 230 ppm for the [C4C1C1^{2}im][NTf2] samples and in the range of 160 to 280 ppm for $[C_4C_1C1^2im][NTf_2]$. On the available instrument, replicate measurements give variation in water content as large as 50 ppm. Even with the error bar associated with the measurement, this determination agrees with the FTIR spectroscopy in magnitude and the trend (slightly higher water in the $[C_4C_1C_1^2im][NTf_2]$).

Water content in the few hundred ppm range is reasonable for our determination of viscosity and dynamics. First, the viscosities that we measure compare very well with literature values (considering the spread in the literature). Second, the viscosity of $[C_4C_1im][NTf_2]$ changes slowly with water content (considering the trace amounts we are discussing). For example, one can estimate that the viscosity should change by only 0.5% at 200 ppm water

content ($x_{\mathrm{H2O}} = 0.0045$) by linear interpolation within the data of Canongia Lopes et al *J Phys Chem B,* **115**, 6088 (2011).

A.2 VISCOSITY

The viscosities of the ILs are unaffected by the 30 mM concentration of the thiocyanate. The viscosity of neat $[C_4C_1C_1^2\mathrm{im}][NTf_2]$ is 99.7 ± 0.1 cP and the mixture is 99.3 ± 0.1 cP; similarly the viscosity of $[C_4C_1\mathrm{im}][NTf_2]$ is 50.1 ± 0.1 cP and the mixture is 50.2 ± 0.1 cP. These viscosity measurements are within the range of viscosities reported in the literature (see Hunt JPCB 2007 for a summary); our measurement for $[C_4C_1\mathrm{im}][NTf_2]$ agree exactly with the report from Canongia Lopes et al *J Phys Chem B,* **115**, 6088 (2011).

A.3 LONG TIME SPECTRA

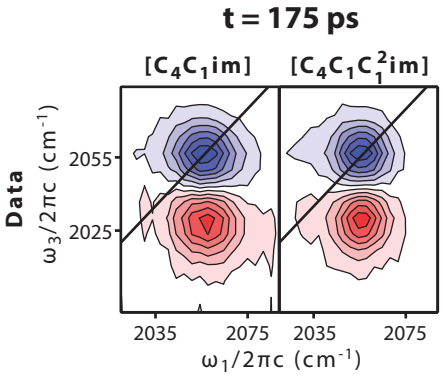

Figure 28: **Decay of correlation** Spectra at 175 ps show the decay of frequency correlation to 0 within error for both ionic liquids.

APPENDIX B

ION-PAIR FORMATION AND WATER-INDUCED HETEROGENEITY SUPPORTING INFORMATION

B.1 COMPARISON OF DIFFERENT DATA ANALYSIS METHODS

Three different fitting methods, namely ellipticity, center-line slope and global fitting are applied to each individual data set, and similar results are obtained.

The ellipticity fitting method is manipulated by fitting the 2D spectra with two two-dimensional Gaussians with opposite signs. The two Gaussians are set restricted to have same amplitude and full width at half maximum (FWHM). The obtained diagonal (σ_d) and anti-diagonal (σ_a) width are then calculated to obtain the ellipticity data:

$$Ellipticity = \frac{\sigma_d^2 - \sigma_a^2}{\sigma_d^2 + \sigma_a^2} \tag{B.1}$$

Error bars are estimated by propagation of error in the fits of the two-dimensional Gaussians' parameters.

For the center-line slope method, we plot the signal size as a function of final frequency (ω_3) for each initial frequency (ω_1) data point, and fit with two Gaussians with opposite signs. The resolved position of the Gaussians are used for determining the center point. The

determined center point is then fitted linearly as a function of ω_1 to extract the center-line slope. Estimated errors are propagated accordingly.

The global fitting method is based on Kubo lineshape theory. Simulated spectra are generated and compared with the experimental result, and the error bars are estimated by a bootstrap method.

A typical set of data with three different analysis methods is shown in figure 1. The fitted spectra from ellipticity measurement could catch the inhomogeneous feature of the spectra, while the center points determined by the center-line slope method are very linear and through the center of the 0 to 1 transition peak. When plotted as a function of t_2 time, ellipticity and center-line slope give consistent trends on spectral diffusion, and a slight systematic error can be observed with ellipticity is systematically lower than center-line slope by ~ 0.02. The global fitting method is also capable of catching the main feature of spectral diffusion.

The timescales that resolved from three different fitting methods are consistent with each other, indicating 2D-IR experiment is capable of catching the major feature of spectral diffusion, and is independent of the data analysis method.

One way to determine correlation between multiple variables is through the use of a scatterplot matrix. Figure 31 shows a scatterplot matrix for the fitting parameters resulting from the bootstrapping of the global fit for KSCN in $[C_4C_1im][NTf_2]$, which was chosen to be analyzed because large confidence intervals resulting from bootstrapping of the global fit likely indicate covariance between multiple of the fitting parameters. Each subplot of the scatterplot matrix shows the correlation between two fitting parameters, which may be determined by seeing which label corresponds to each axis of the subplot. As expected, the plot shows multiple correlations between the different fitting parameters. Of particular note is the strong correlation between the longer spectral diffusion time (τ_2) and the frequency deviation for the static component of the correlation function (Δ_3). This correlation helps to explain the large standard deviation in τ_2 seen from bootstrapping. As the linewidth of Δ_3 decreases, the fit increases τ_2 to continue to obtain the residual ellipticity seen in the spectra

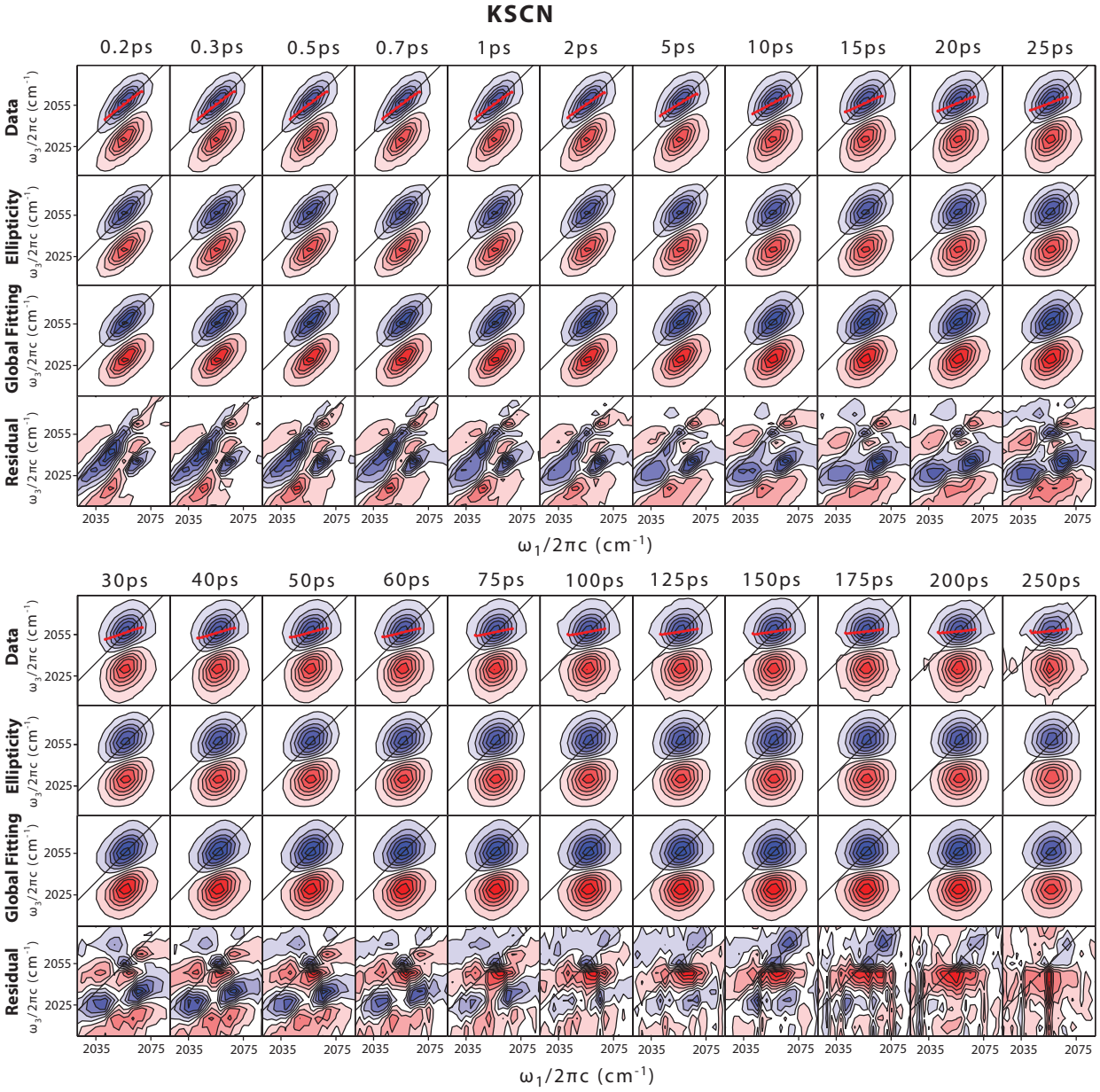

Figure 29: 30 mM KSCN in $[C_4C_1C_1^2im][NTf_2]$, the first row shows the experimental data and CLS fitting result; the second row shows the fitted two-dimensional Gaussian for the ellipticity method; the third row is the calculated spectra from Kubo lineshape theory; the last row shows the difference between the third and first row.

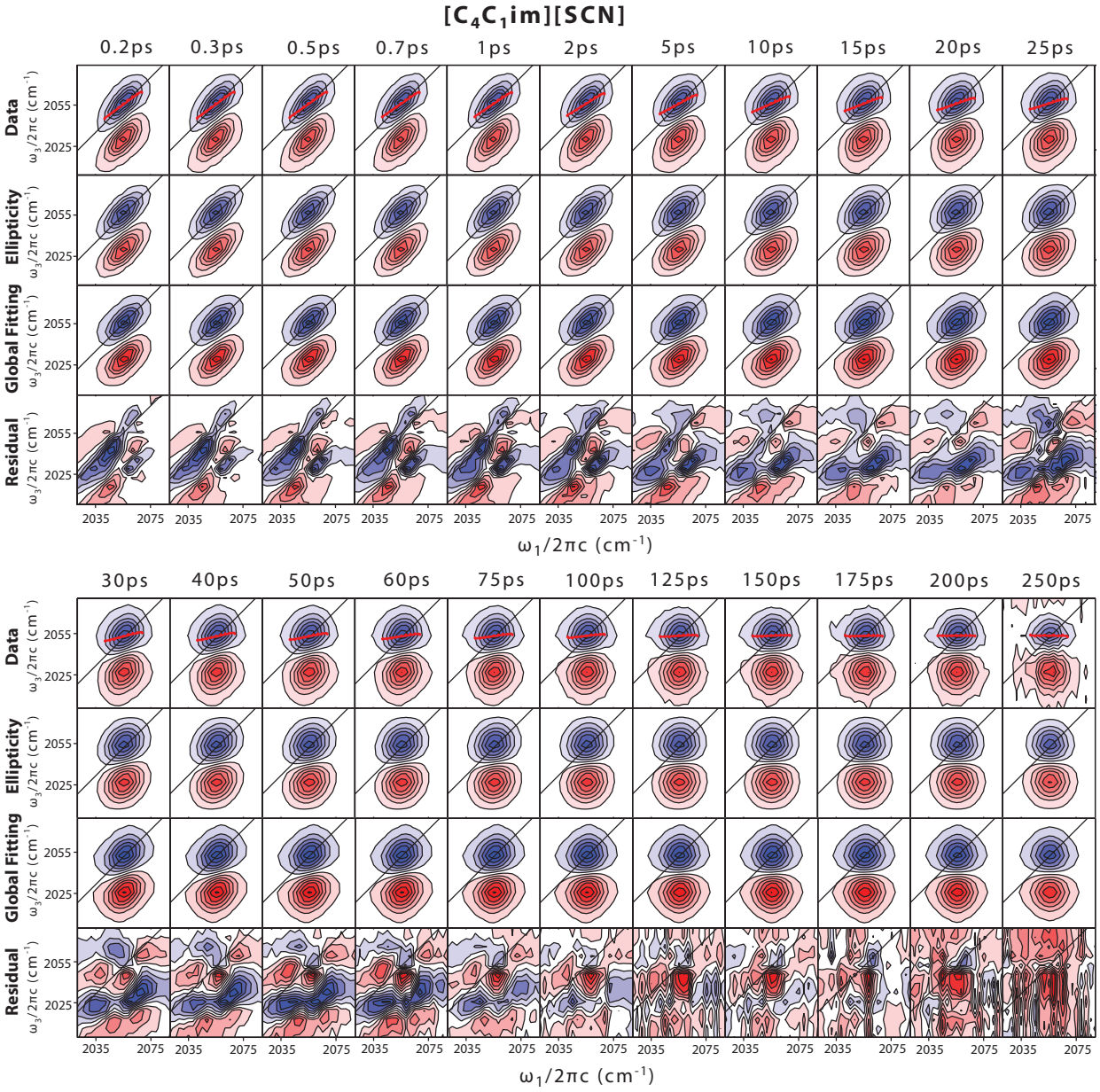

Figure 30: 30 mM $[C_4C_1im][SCN]$ in $[C_4C_1C_1^2im][NTf_2]$, the first row shows the experimental data and CLS fitting result; the second row shows the fitted two-dimensional Gaussian for the ellipticity method; the third row is the calculated spectra from Kubo lineshape theory; the last row shows the difference between the third and first row.

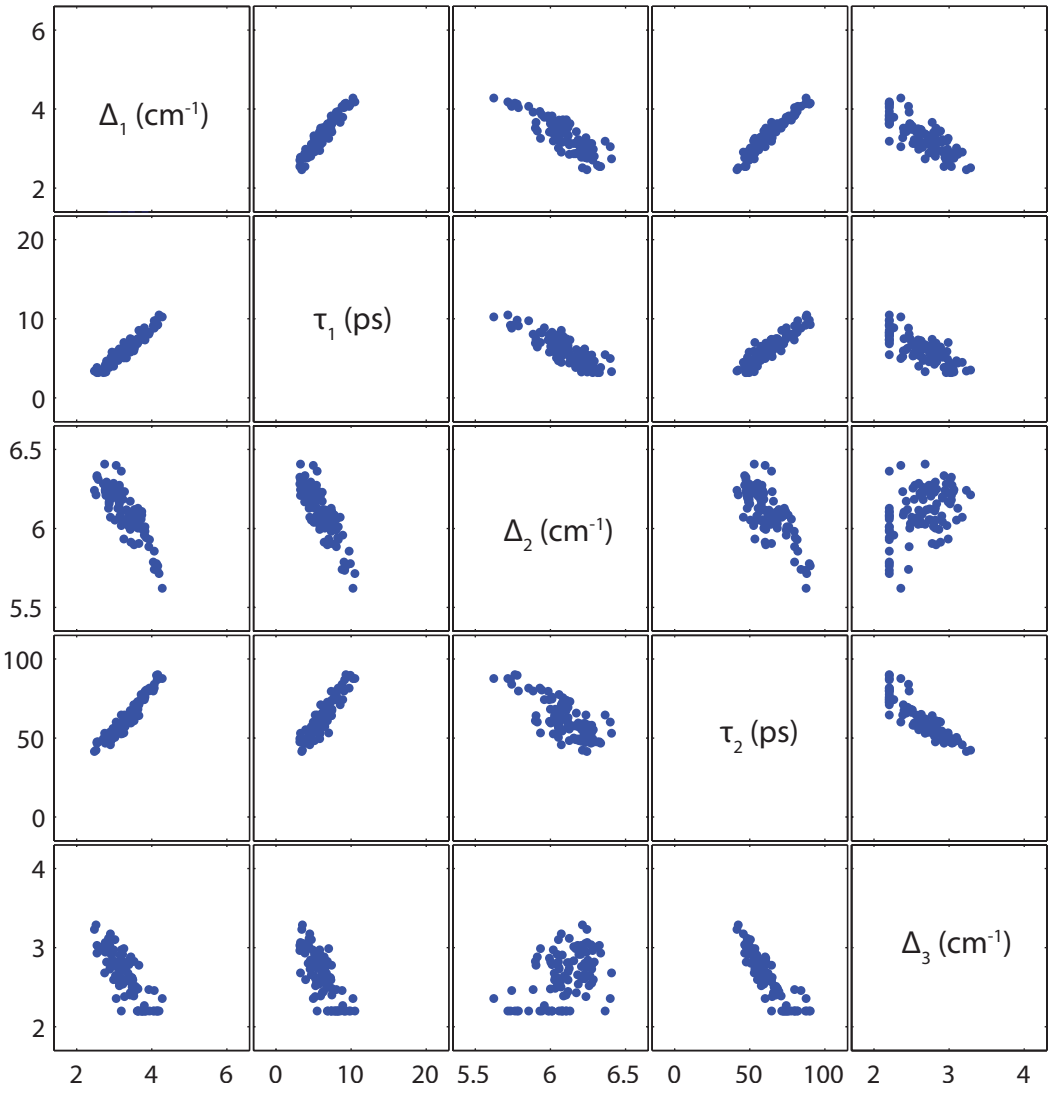

Figure 31: Scatteplot matrix for the fitting parameters resulting from the bootstrapping of the global fit for KSCN in $[C_4C_1im][Tf_2N]$ shows multiple correlations between the different fitting parameters.

at the longest population times. Due to the static component seen on spectral fitting using both ellipticity and the CLS method, Δ_3 was already constrained to be at least 2.2 cm^{-1}. While it might be possible to further reduce the variability seen in τ_2 by further constraining Δ_3, it is likely impossible to completely remove the ambiguity seen in the fitting of this number of parameters, many of which influence spectral lineshape in similar ways.

B.2 SUBTRACTED 2D SPECTRA

The 2D-IR experiment of 30 mM of $[C_4C_1im][SCN]$ dissolved in water saturated $[C_4C_1C_1^2im][NTf_2]$ resolves two sub-ensembles, which we refer to "dry" and "wet" ensembles. Two extract the dynamics from the "wet" ensemble, we subtract the water saturated data from dry data to eliminate the contribution from "dry" ensemble. The subtracted has a total time window of 20 ps before the signal is too weak to resolve a reasonable lineshape. The subtracted data is in the inhomogeneous limit because the peaks are highly elliptical. The peaks are changing over time within 20 ps, indicating structural relaxation is taking place.The subtracted data is analysed by ellipticity. Fitted data catches major features of spectral diffusion.

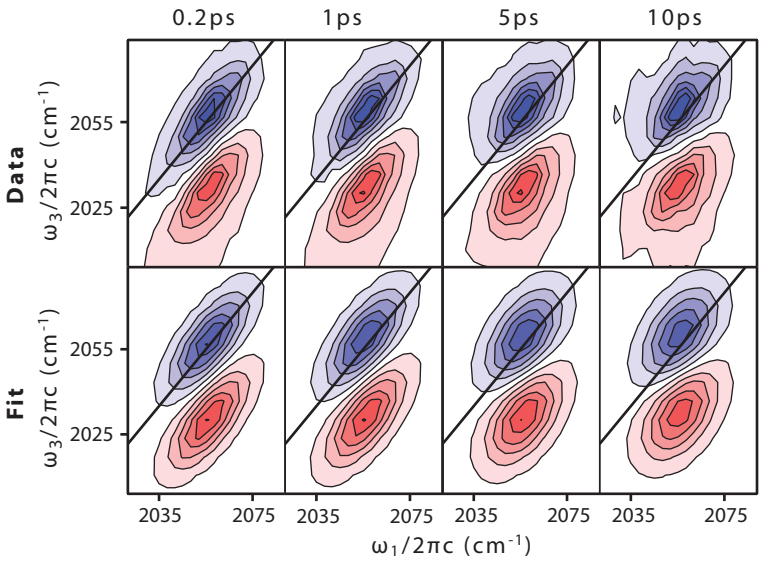

Figure 32: Subtracted 2D spectra of 30 mM of $[C_4C_1im][SCN]$ dissolved in water saturated $[C_4C_1C_1^2im][NTf_2]$ (top) and the fitted spectra.

APPENDIX C

IONIC LIQUIDS IN COLLOIDAL DISPERSIONS SUPPORTING INFORMATION

C.1 DYNAMIC LIGHT SCATTERING DATA

The dynamic light scattering (DLS) experiments have been conducted on two different instruments. One is a commercial Malvern ZS90 Zetasizer; the other one is a home-built Brookhaven DLS instrument. Both DLS instruments operate at 633 nm.

Through out the DLS experiments, the angle between the incident light and the detector is kept at 90 degrees, and the temperature is stabilized at room temperature. The data acquisition time is 300 seconds.

We have tried with different surfactant concentrations. For concentrations lower than 100 mM, no readable signal is presence for both instruments. When the concentration is above 100 mM, there are minor reproducible features, but the signal is still too weak to yield unambiguous size information.

It is possible to fit the feature from the Brookhaven instrument to get an estimation of the size. The diameter is estimated to be $\sim$1 nm, which is similar than the estimation given by DOSY experiments, but is systematically smaller. The fitting is highly dependent on the acquisition time range and the fitting model.

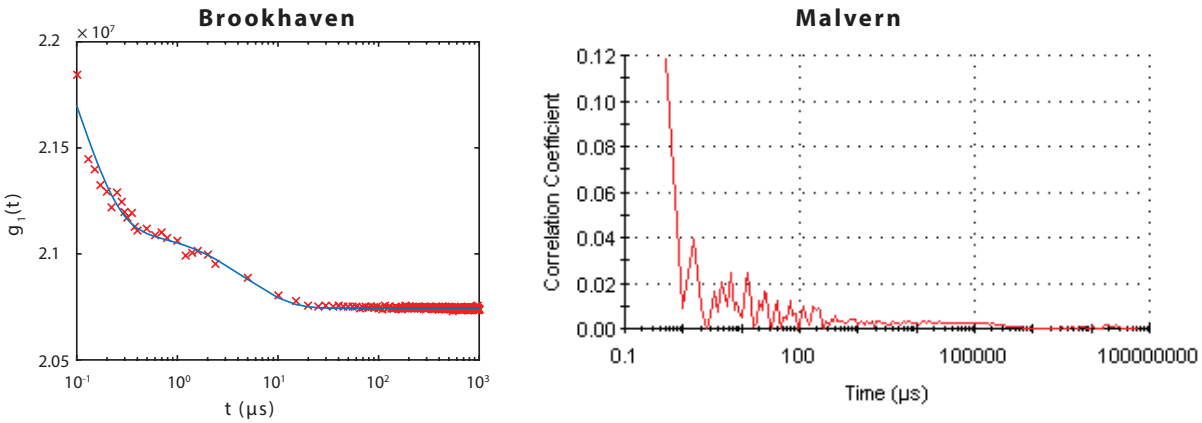

Figure 33: The correlation plot with Brookhaven and Malvern instruments. The sample is $[C_4C_1im][SCN]$ with AOT in chlorobenzene, with W = 0.5 and the surfactant concentration is 400mM.

Previous literature has utilized DLS with 488 nm laser source to characterize the size of $[C_4C_1im][NTf_2]$/surfactant systems. Since the probability for scattering event to happen is proportional to the wavelength to the fourth power, it is reasonable to suspect that our 633 nm laser is too long to characterize clusters of one nanometer. In the future, we could try DLS instruments with shorter wavelengths.

C.2 ANISOTROPY DECAY IN IONIC LIQUID-SURFACTANT COMPLEXES

The anisotropy for each time point is obtained from the 2D-IR spectra. The resolved 2D-IR spectra are fitted with two two-dimensional Gaussians with opposite signs. The shape parameter (diagonal and antidiagonal width) are used to calculate the ellipticity, and the intensity parameter (amplitude of the peak, I) is used to calculate the anisotropy.

Representative anisotropy decay curves show that the anisotropy experiences a fast decay

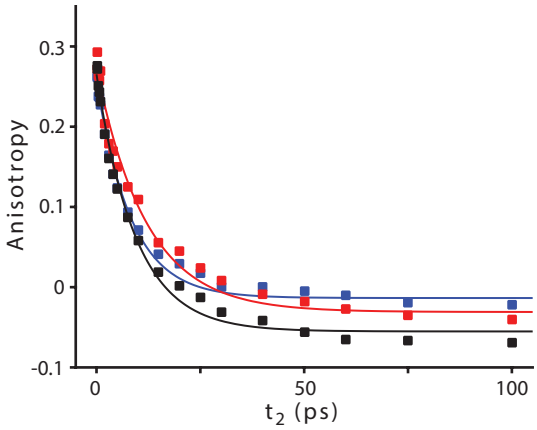

Figure 34: The anisotropy decay of thiocyanate in BHDC (red), AOT (blue) and TX-100 (black) systems. The solvent is chlorobenzene, and W = 0.5.

for all three IL/surfactant systems. By ∼20 ps, the anisotropy decays to near zero and stays constant for the rest of the waiting time. The fitting with single exponential plus a constant has good agreement with the overall trend, which suggests diffusive reorientation.

It is worth noting that the anisotropy decays to negative for some systems. This is possibly because the pump intensities are not perfectly equal for the two polarization configurations in our experiments. It is possible that there is a constant offset for anisotropy, due to the non-isotropic orientation distribution. Based on the quality of our data, however, it is not possible to distinguish the offset.

C.3 REORIENTATION AND STRUCTURAL DYNAMICS OF [C_4C_1IM][SCN] IN PURE TX-100

The TX-100 is liquid at room temperature, and therefore it is possible to obtain the dynamics of [C_4C_1im][SCN] in pure TX-100. This system provides us an important data point to compare with the IL-surfactant complex systems. When the W value is very small, one

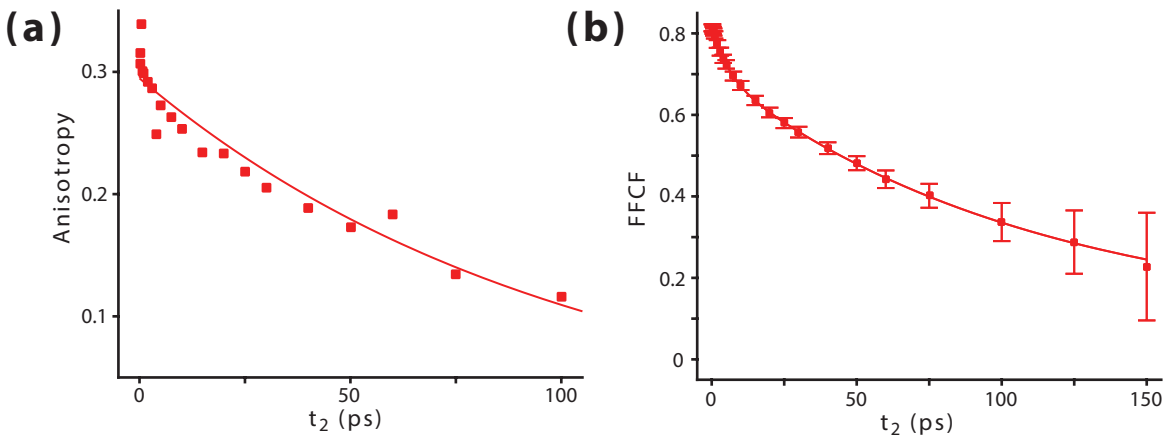

Figure 35: The anisotropy decay (a) and the FFCF in ZZZZ configuration (b) of $[C_4C_1im][SCN]$ in pure TX-100.

could think that each particle is constructed with only one $[C_4C_1im][SCN]$ ion-pair, and many TX-100 molecules. If the ionic liquid was surrounded by TX-100, then one would expect the dynamics observed should be similar to the dynamics in the bulk TX-100. If the ionic liquid is not very well surrounded, then the overall dynamics should be significantly different.

The dynamics, regardless of reorientation or structural, are much slower for pure TX-100 compared to the IL-surfactant complex.

The anisotropy of thiocyanate decays gradually within the waiting time, but it is not fully resolved within our experimental waiting time, indicating a much longer reorientation time. Indeed, the single exponential fit is capable of capturing major features, and the resolved timescale is $\sim$100 ps (Table 8). The reorientation time is almost an order of magnitude slower than that in the complex system.

The structural dynamics of thiocyanate in pure TX-100 is also significantly slower than the bulk dynamics. From the FFCF curve, one could see that for almost all the data points, the pure TX-100 system yields a higher correlation, indicating slower dynamics. Since the

FFCF is not fully resolved within our experimental time, the fitting gives a relatively big offset. Nonetheless, the resolved timescales are still slower than the IL-surfactant complex systems.

Table 8: Fitting result for pure TX-100 systems

Parameter	Value
τ_1(ps)	5.4 ± 0.6
τ_2(ps)	109 ± 17
A	0.11 ± 0.01
B	0.62 ± 0.05
C	0.09 ± 0.06
τ_{or}	105

BIBLIOGRAPHY

[1] Hamm, P.; Zanni, M. T. *Concepts and Methods of 2D Infrared Spectroscopy*; Cambridge University Press, 2011.

[2] Fecko, C. J.; Eaves, J. D.; Loparo, J. J.; Tokmakoff, A.; Geissler, P. L. *Science* **2003**, *301*, 1698–1702.

[3] de Boeij, W. P.; Pshenichnikov, M. S.; Wiersma, D. A. *Annu. Rev. Phys. Chem.* **1998**, *49*, 99–123.

[4] Sun, Z.; Zhang, W.; Ji, M.; Hartsock, R.; Gaffney, K. J. *J. Phys. Chem. B* **2013**, *117*, 15306–15312.

[5] Sun, Z.; Zhang, W.; Ji, M.; Hartsock, R.; Gaffney, K. J. *J. Phys. Chem. B* **2013**, *117*, 12268–12275.

[6] Ji, M.; Park, S.; Gaffney, K. J. *J. Phys. Chem. Lett.* **2010**, *1*, 1771–1775.

[7] Chung, H. S.; Ganim, Z.; Jones, K. C.; Tokmakoff, A. *Proc. Natl. Acad. Sci. U. S. A.* **2007**, *104*, 14237–14242.

[8] Lindquist, B. A.; Furse, K. E.; Corcelli, S. A. *Phys. Chem. Chem. Phys.* **2009**, *11*, 8119–8132.

[9] Ghosh, A.; Tucker, M. J.; Hochstrasser, R. M. *J. Phys. Chem. A* **2011**, *115*, 9731–9738.

[10] Ma, J.; Pazos, I. M.; Zhang, W.; Culik, R. M.; Gai, F. *Annu. Rev. Phys. Chem.* **2015**, *66*, 357–377.

[11] Zheng, J. R.; Kwak, K.; Asbury, J.; Chen, X.; Piletic, I. R.; Fayer, M. D. *Science* **2005**, *309*, 1338–1343.

[12] Bloem, R.; Koziol, K.; Waldauer, S. A.; Buchli, B.; Walser, R.; Samatanga, B.; Jelesarov, I.; Hamm, P. *J. Phys. Chem. B* **2012**, *116*, 13705–13712.

[13] Sokolowsky, K. P.; Fayer, M. D. *J. Phys. Chem. B* **2013**, *117*, 15060–15071.

[14] Nicodemus, R. A.; Ramasesha, K.; Roberts, S. T.; Tokmakoff, A. *J. Phys. Chem. Lett.* **2010**, *1*, 1068–1072.

[15] Perakis, F.; Hamm, P. *J. Phys. Chem. B* **2011**, *115*, 5289–5293.

[16] Ramasesha, K.; Roberts, S. T.; Nicodemus, R. A.; Mandal, A.; Tokmakoff, A. *J. Chem. Phys.* **2011**, *135*, 54509.

[17] Fenn, E. E.; Fayer, M. D. *J. Chem. Phys.* **2011**, *135*, 074502.

[18] Fenn, E. E.; Wong, D. B.; Giammanco, C. H.; Fayer, M. D. *J. Phys. Chem. B* **2011**, *115*, 11658–11670.

[19] Fenn, E. E.; Wong, D. B.; Fayer, M. D. *J. Chem. Phys.* **2011**, *134*, 1–11.

[20] Kim, Y. S.; Hochstrasser, R. M. *J. Phys. Chem. B* **2007**, *111*, 9697–9701.

[21] Kim, Y. S.; Liu, L.; Axelsen, P. H.; Hochstrasser, R. M. *Proc. Natl. Acad. Sci. USA* **2008**, *105*, 7720–7725.

[22] Bakulin, A. A.; Cringus, D.; Pieniazek, P. A.; Skinner, J. L.; Jansen, T. l. C.; Pshenichnikov, M. S. *J. Phys. Chem. B* **2013**, *117*, 15545–58.

[23] Middleton, C. T.; Marek, P.; Cao, P.; Chiu, C.-c.; Singh, S.; Woys, A. M.; de Pablo, J. J.; Raleigh, D. P.; Zanni, M. T. *Nat. Chem.* **2012**, *4*, 355–360.

[24] Pless, S. A.; Ahern, C. A. *Annu. Rev. Pharmacol. Toxicol.* **2013**, *53*, 211–229.

[25] Yamada, S. A.; Bailey, H. E.; Tamimi, A.; Li, C.; Fayer, M. D. *J. Am. Chem. Soc.* **2017**, *139*, 2408–2420.

[26] Cowan, M. L.; Bruner, B. D.; Huse, N.; Dwyer, J. R.; Chugh, B.; Nibbering, E. T. J.; Elsaesser, T.; Miller, R. J. D. *Nature* **2005**, *434*, 199–202.

[27] Jansen, T. L.; Auer, B. M.; Yang, M.; Skinner, J. L. *J. Chem. Phys.* **2010**, *132*.

[28] Asbury, J. B.; Steinel, T.; Fayer, M. D. *J. Phys. Chem. B* **2004**, *108*, 6544–6554.

[29] Auer, B.; Schmidt, J. R.; Skinner, J. L. *Proc. Natl. Acad. Sci. USA* **2007**, *104*, 14215–14220.

[30] Yeremenko, S.; Pschenichnikov, M. S.; Wiersma, D. A. *Chem. Phys. Lett.* **2003**, *369*, 107–113.

[31] Fecko, C. J.; Loparo, J. J.; Roberts, S. T.; Tokmakoff, A. *J. Chem. Phys.* **2005**, *122*, 54506.

[32] Schwarzer, D.; Lindner, J.; Vöhringer, P. *J. Phys. Chem. A* **2006**, *110*, 2858–2867.

[33] Garrett-Roe, S.; Perakis, F.; Rao, F.; Hamm, P. *J. Phys. Chem. B* **2011**, *115*, 6976–6984.

[34] Sun, Z.; Zhang, W.; Ji, M.; Hartsock, R.; Ga, K. J. *J. Phys. Chem. B* **2013**, *117*, 12668–12275.

[35] Lee, K.-K.; Park, K.-H.; Kwon, D.; Choi, J.-H.; Son, H.; Park, S.; Cho, M. *J. Chem. Phys.* **2011**, *134*, 064506.

[36] Kwon, Y.; Park, S. *Phys. Chem. Chem. Phys.* **2015**, *17*, 24193–24200.

[37] Kwon, Y.; Lee, J.; Park, S. *Phys. Chem. Chem. Phys.* **2017**, *19*, 10889–10897.

[38] Lee, C.; Son, H.; Park, S. *Phys. Chem. Chem. Phys.* **2015**, *17*, 17557–17561.

[39] Kirchner, B.; Malberg, F.; Firaha, D. S.; Hollóczki, O. *J. Phys. Condens. Matter* **2015**, *27*.

[40] Hollóczki, O.; Malberg, F.; Welton, T.; Kirchner, B. *Phys. Chem. Chem. Phys.* **2014**, *16*, 16880–90.

[41] Biswas, R.; Furtado, J.; Bagchi, B. *J. Chem. Phys.* **2013**, *139*, 144906.

[42] Lei, Z.; Chen, B.; Koo, Y. M.; Macfarlane, D. R. *Chem. Rev.* **2017**, *117*, 6633–6635.

[43] Bara, J. E.; Carlisle, T. K.; Gabriel, C. J.; Camper, D.; Finotello, A.; Gin, D. L.; Noble, R. D. *Ind. Eng. Chem. Res.* **2009**, *48*, 2739–2751.

[44] Gurkan, B. E.; de la Fuente, J. C.; Mindrup, E. M.; Ficke, L. E.; Goodrich, B. F.; Price, E. A.; Schneider, W. F.; Brennecke, J. F. *J. Am. Chem. Soc.* **2010**, *132*, 2116–2117.

[45] Ramdin, M.; de Loos, T. W.; Vlugt, T. J. H. *Ind. Eng. Chem. Res.* **2012**, *51*, 8149–8177.

[46] Firaha, D. S.; Hollóczki, O.; Kirchner, B. *Angew. Chemie Int. Ed.* **2015**, *54*, 7805–7809.

[47] Mai, N. L.; Koo, Y. M. *ACS Sustain. Chem. Eng.* **2016**, *4*, 541–547.

[48] Ventura, S. P. M.; e Silva, F. A.; Quental, M. V.; Mondal, D.; Freire, M. G.; Coutinho, J. A. P. *Chem. Rev.* **2017**, *117*, 6984–7052.

[49] Zhang, Q.; Zhang, S.; Deng, Y. *Green Chem.* **2011**, *13*, 2619.

[50] Vekariya, R. L. *J. Mol. Liq.* **2017**, *227*, 40.

[51] Toledo Hijo, A. A.; Maximo, G. J.; Costa, M. C.; Batista, E. A.; Meirelles, A. J. *ACS Sustain. Chem. Eng.* **2016**, *4*, 5347–5369.

[52] Dong, K.; Liu, X.; Dong, H.; Zhang, X.; Zhang, S. Multiscale Studies on Ionic Liquids. 2017; http://pubs.acs.org/doi/10.1021/acs.chemrev.6b00776.

[53] Nunes, V. M.; Lourenço, M. J.; Santos, F. J.; Nieto De Castro, C. A. *J. Chem. Eng. Data* **2003**, *48*, 446–450.

[54] Hendriks, E.; Kontogeorgis, G. M.; Dhorn, R.; de Hemptinne, J. C.; Economou, I. G.; Fele Zilnik, L.; Vesovic, V. *Ind. Eng. Chem. Res.* **2010**, *49*, 11131–11141.

[55] Paduszyński, K.; Domańska, U. *J. Chem. Inf. Model.* **2014**, *54*, 1311–1324.

[56] Koller, T.; Rausch, M. H.; Schulz, P. S.; Berger, M.; Wasserscheid, P.; Economou, I. G.; Leipertz, A.; Fröba, A. P. *J. Chem. Eng. Data* **2012**, *57*, 828–835.

[57] Alcalde, R.; García, G.; Atilhan, M.; Aparicio, S. *Ind. Eng. Chem. Res.* **2015**, *54*, 10918–10924.

[58] Okoturo, O.; VanderNoot, T. *J. Electroanal. Chem.* **2004**, *568*, 167–181.

[59] Tao, D. J.; Hu, W. J.; Chen, F. F.; Chen, X. S.; Zhang, X. L.; Zhou, Y. *J. Chem. Eng. Data* **2014**, *59*, 4031–4038.

[60] Chaban, V. V. *Phys. Chem. Chem. Phys.* **2015**, *17*, 31839–31849.

[61] Otani, A.; Zhang, Y.; Matsuki, T.; Kamio, E.; Matsuyama, H.; Maginn, E. J. *Ind. Eng. Chem. Res.* **2016**, *55*, 2821–2830.

[62] Martin, S.; Pratt, H. D.; Anderson, T. M. *Mol. Inform.* **2017**, *36*, 1600125.

[63] Bier, M.; Dietrich, S. *Mol. Phys.* **2010**, *108*, 211–214.

[64] Fox, D. M.; Gilman, J. W.; Morgan, A. B.; Shields, J. R.; Maupin, P. H.; Lyon, R. E.; De Long, H. C.; Trulove, P. C. *Ind. Eng. Chem. Res.* **2008**, *47*, 6327–6332.

[65] Brandt, A.; Ray, M. J.; To, T. Q.; Leak, D. J.; Murphy, R. J.; Welton, T. *Green Chem.* **2011**, *13*, 2489.

[66] Brandt, A.; Gräsvik, J.; Hallett, J. P.; Welton, T. *Green Chem.* **2013**, *15*, 550–583.

[67] Chiappe, C.; Pieraccini, D.; Saullo, P. *J. Org. Chem.* **2003**, *68*, 6710–6715.

[68] Kim, D. W.; Song, C. E.; Chi, D. Y. **2003**, 4281–4285.

[69] Crowhurst, L.; Lancaster, N. L.; Arlandis, J. M. P.; Welton, T. *J. Am. Chem. Soc.* **2004**, *126*, 11549–11555.

[70] Pousse, G.; Cavelier, F. L.; Humphreys, L.; Rouden, J.; Blanchet, J. *Org. Lett.* **2010**, *12*, 3582–3585.

[71] Dong, F.; Jian, C.; Kai, G.; Qunrong, S.; Zuliang, L. *Catal. Letters* **2008**, *121*, 255–259.

[72] Chaskar, A. C.; Bhandari, S. R.; Patil, A. B.; Sharma, O. P.; Mayeker, S. *Synth. Commun.* **2009**, *39*, 366–370.

[73] Ranu, B. C.; Banerjee, S. *Org. Lett.* **2005**, *7*, 3049–3052.

[74] Xu, J. M.; Liu, B. K.; Wu, W. B.; Qian, C.; Wu, Q.; Lin, X. F. *J. Org. Chem.* **2006**, *71*, 3991–3993.

[75] Fujita, K.; MacFarlane, D. R.; Forsyth, M. *Chem. Commun.* **2005**, *70*, 4804.

[76] Weingärtner, H.; Cabrele, C.; Herrmann, C. *Phys. Chem. Chem. Phys.* **2012**, *14*, 415–426.

[77] Huang, Z. L.; Yang, T. X.; Huang, J. Z.; Yang, Z. *Bioenergy Res.* **2014**, *7*, 1519–1528.

[78] van Rantwijk, F.; Sheldon, R. A. *Chem. Rev.* **2007**, *107*, 2757–2785.

[79] Deive, F. J.; Ruivo, D.; Rodrigues, J. V.; Gomes, C. M.; Sanromán, M. Á.; Rebelo, L. P. N.; Esperança, J. M. S. S.; Rodríguez, A. *RSC Adv.* **2015**, *5*, 3386–3389.

[80] Brogan, A. P.; Hallett, J. P. *J. Am. Chem. Soc.* **2016**, *138*, 4494–4501.

[81] Pereiro, A. B.; Araújo, J. M. M.; Oliveira, F. S.; Esperança, J. M. S. S.; Canongia Lopes, J. N.; Marrucho, I. M.; Rebelo, L. P. N. *J. Chem. Thermodyn.* **2012**, *55*, 29–36.

[82] Kohno, Y.; Ohno, H. *Chem. Commun.* **2012**, *48*, 7119.

[83] Blach, D.; Pessêgo, M.; Silber, J. J.; Correa, N. M.; García-Río, L.; Falcone, R. D. *Langmuir* **2014**, *30*, 12130–12137.

[84] Gayet, F.; Kalamouni, C. E.; Lavedan, P.; Marty, J. D.; Brûlet, A.; Viguerie, N. L. D. *Langmuir* **2009**, *25*, 9741–9750.

[85] Debnath, S.; Das, D.; Dutta, S.; Das, P. K. *Langmuir* **2010**, *26*, 4080–4086.

[86] Setua, P.; Pramanik, R.; Sarkar, S.; Ghatak, C.; Rao, V. G.; Sarkar, N.; Das, S. K. *J. Mol. Liq.* **2011**, *162*, 33–37.

[87] Li, Y.; Qiang, Q.; Zheng, X.; Wang, Z. *Electrochem. commun.* **2015**, *58*, 41–45.

[88] Hamm, P.; Kaindl, R. A.; Stenger, J. *Opt. Lett.* **2000**, *25*, 1798–1800.

[89] Helbing, J.; Hamm, P. *J. Opt. Soc. Am. B* **2011**, *28*, 171.

[90] Bates, E. D.; Mayton, R. D.; Ntai, I.; Davis, J. H. *J. Am. Chem. Soc.* **2002**, *124*, 926–927.

[91] Frackowiak, E. *Phys. Chem. Chem. Phys.* **2007**, *9*, 1774–1785.

[92] Wang, P.; Zakeeruddin, S. M.; Moser, J.-E.; Humphry-Baker, R.; Grätzel, M. *J. Am. Chem. Soc.* **2004**, *126*, 7164–7165.

[93] Zhou, F.; Liang, Y.; Liu, W. *Chem. Soc. Rev.* **2009**, *38*, 2590–2599.

[94] Bonhôte, P.; Dias, A.-P.; Papageorgiou, N.; Kalyanasundaram, K.; Grätzel, M. *Inorg. Chem.* **1996**, *35*, 1168–1178.

[95] Welton, T. *Chem. Rev.* **1999**, *99*, 2071–2084.

[96] Hallett, J. P.; Welton, T. *Chem. Rev.* **2011**, *111*, 3508–3576.

[97] Zahn, S.; Uhlig, F.; Thar, J.; Spickermann, C.; Kirchner, B. *Angew. Chem. Int. Ed. Engl.* **2008**, *47*, 3639–3641.

[98] Fumino, K.; Wulf, A.; Ludwig, R. *Angew. Chem. Int. Ed. Engl.* **2008**, *47*, 8731–8734.

[99] Thar, J.; Brehm, M.; Seitsonen, A. P.; Kirchner, B. *J. Phys. Chem. B* **2009**, *113*, 15129–15132.

[100] Kohagen, M.; Brehm, M.; Lingscheid, Y.; Giernoth, R.; Sangoro, J.; Kremer, F.; Naumov, S.; Iacob, C.; Kärger, J.; Valiullin, R.; Kirchner, B. *J. Phys. Chem. B* **2011**, *115*, 15280–15288.

[101] Kohagen, M.; Brehm, M.; Thar, J.; Zhao, W.; Müller-Plathe, F.; Kirchner, B. *J. Phys. Chem. B* **2011**, *115*, 693–702.

[102] Canongia Lopes, J. N. *Phys. Chem. Chem. Phys.* **2002**, *4*, 949–954.

[103] Del Pópolo, M. G.; Voth, G. A. *J. Phys. Chem. B* **2004**, *108*, 1744–1752.

[104] Wang, Y.; Voth, G. A. *J. Am. Chem. Soc.* **2005**, *127*, 12192–12193.

[105] Urahata, S. M.; Ribeiro, M. C. C. *J. Phys. Chem. Lett.* **2010**, *1*, 1738–1742.

[106] Hunt, P. A. *J. Phys. Chem. B* **2007**, *111*, 4844–4853.

[107] Izgorodina, E. I.; Maganti, R.; Armel, V.; Dean, P. M.; Pringle, J. M.; Seddon, K. R.; MacFarlane, D. R. *J. Phys. Chem. B* **2011**, *115*, 14688–14697.

[108] Castner, E. W. J.; Wishart, J. F. *J. Chem. Phys.* **2010**, *132*, 120901.

[109] Fruchey, K.; Fayer, M. D. *J. Phys. Chem. B* **2010**, *114*, 2840–2845.

[110] Fruchey, K.; Lawler, C. M.; Fayer, M. D. *J. Phys. Chem. B* **2012**, *116*, 3054–3064.

[111] Castner, E. W. J.; Wishart, J. F.; Shirota, H. *Acc. Chem. Res.* **2007**, *40*, 1217–1227.

[112] Jin, H.; Li, X.; Maroncelli, M. *J. Phys. Chem. B* **2007**, *111*, 13473–13478.

[113] Khurmi, C.; Berg, M. A. *J. Phys. Chem. Lett.* **2010**, *1*, 161–164.

[114] Zhang, X.-X.; Liang, M.; Ernsting, N. P.; Maroncelli, M. *J. Phys. Chem. B* **2013**, *117*, 4291–4304.

[115] Turton, D. A.; Hunger, J.; Stoppa, A.; Hefter, G.; Thoman, A.; Walkther, M.; Buchner, R.; Wynne, K. *J. Am. Chem. Soc.* **2009**, *131*, 11140–11146.

[116] Xiao, D.; Hines, Jr., L. G.; Bartsch, R. A.; Quitevis, E. L. *J. Phys. Chem. B* **2009**, *113*, 4544–4548.

[117] Bardak, F.; Xiao, D.; Hines, Jr., L. G.; Son, P.; Bartsch, R. A.; Quitevis, E. L.; Yang, P.; Voth, G. A. *ChemPhysChem* **2012**, *13*, 1687–1700.

[118] Zhang, S.; Shi, R.; Ma, X.; Lu, L.; He, Y.; Zhang, X.; Wang, Y.; Deng, Y. *Chemistry* **2012**, *18*, 11904–11908.

[119] Dahl, K.; Sando, G. M.; Fox, D. M.; Sutto, T. E.; Owrutsky, J. C. *J. Chem. Phys.* **2005**, *123*, 084504.

[120] Jacquemin, J.; Husson, P.; Padua, A. A. H.; Majer, V. *Green Chem.* **2006**, *8*, 172–180.

[121] Brüssel, M.; Brehm, M.; Voigt, T.; Kirchner, B. *Phys. Chem. Chem. Phys.* **2011**, *13*, 13617–13620.

[122] Lazonder, K.; Pshenichnikov, M. S.; Wiersma, D. A. *Opt. Lett.* **2006**, *31*, 3354–3356.

[123] Roberts, S. T.; Loparo, J. J.; Tokmakoff, A. *J. Chem. Phys.* **2006**, *125*, 84502.

[124] Zhang, Y.; Maginn, E. J. *Phys. Chem. Chem. Phys.* **2012**, *14*, 12157–12164.

[125] Liu, H.; Maginn, E. *J. Chem. Phys.* **2011**, *135*, 124507.

[126] Tokuda, H.; Tsuzuki, S.; Susan, M. A. B. H.; Hayamizu, K.; Watanabe, M. *J. Phys. Chem. B* **2006**, *110*, 19593–19600.

[127] Gebbie, M. A.; Valtiner, M.; Banquy, X.; Fox, E. T.; Henderson, W. A.; Israelachvili, J. N. *Proc. Natl. Acad. Sci. U. S. A.* **2013**, *110*, 9674–9679.

[128] Zhao, W.; Leroy, F.; Heggen, B.; Zahn, S.; Kirchner, B.; Balasubramanian, S.; Müller-Plathe, F.; Muller-Plathe, F. *J. Am. Chem. Soc.* **2009**, *131*, 15825–15833.

[129] Ren, Z.; Ivanova, A. S.; Couchot-Vore, D.; Garrett-Roe, S. *J. Phys. Chem. Lett.* **2014**, *5*, 1541–1546.

[130] Seddon, K. R. *J. Chem. Technol. Biotechnol.* **1997**, *68*, 351–356.

[131] Rogers, R. D.; Seddon, K. R. *Science* **2003**, *302*, 792–3.

[132] Karadas, F.; Atilhan, M.; Aparicio, S. *Energy Fuels* **2010**, *24*, 5817–5828.

[133] Bara, J. E.; Camper, D. E.; Gin, D. L.; Noble, R. D. *Acc. Chem. Res.* **2010**, *43*, 152–159.

[134] Wang, P.; Zakeeruddin, S. M.; Comte, P.; Exnar, I.; Grätzel, M. *J. Am. Chem. Soc.* **2003**, *125*, 1166–1167.

[135] Armand, M.; Endres, F.; MacFarlane, D. R.; Ohno, H.; Scrosati, B. *Nat. Mater.* **2009**, *8*, 621–629.

[136] Dupont, J.; de Souza, R. F.; Suarez, P. A. Z. *Chem. Rev.* **2002**, *102*, 3667–3692.

[137] Wasserscheid, P.; Keim, W. *Angew. Chem. Int. Ed. Engl.* **2000**, *39*, 3772–3789.

[138] Zhao, H.; Holladay, J. E.; Brown, H.; Zhang, Z. C. *Science* **2007**, *316*, 1597–1600.

[139] Lee, S. H.; Doherty, T. V.; Linhardt, R. J.; Dordick, J. S. *Biotechnol. Bioeng.* **2009**, *102*, 1368–76.

[140] Triolo, A.; Russina, O.; Bleif, H.-J.; Di Cola, E. *J. Phys. Chem. B* **2007**, *111*, 4641–4644.

[141] Noda, A.; Hayamizu, K.; Watanabe, M. *J. Phys. Chem. B* **2001**, *105*, 4603–4610.

[142] Tokuda, H.; Hayamizu, K.; Ishii, K.; Susan, M. A. B. H.; Watanabe, M. *J. Phys. Chem. B* **2005**, *109*, 6103–6110.

[143] MacFarlane, D. R.; Forsyth, M.; Izgorodina, E. I.; Abbott, A. P.; Annat, G.; Fraser, K. *Phys. Chem. Chem. Phys.* **2009**, *11*, 4962–4967.

[144] Hu, Z.; Margulis, C. J. *Proc. Natl. Acad. Sci. U. S. A.* **2006**, *103*, 831–836.

[145] Hu, Z.; Margulis, C. J. *Acc. Chem. Res.* **2007**, *40*, 1097–1105.

[146] Habasaki, J.; Ngai, K. L. *J. Chem. Phys.* **2008**, *129*, 194501.

[147] Köddermann, T.; Ludwig, R.; Paschek, D. *ChemPhysChem* **2008**, *9*, 1851–1858.

[148] Miyake, Y.; Hidemori, T.; Akai, N.; Kawai, A.; Shibuya, K.; Koguchi, S.; Kitazume, T. *Chem. Lett.* **2009**, *38*, 124–125.

[149] Harris, K. R. *J. Phys. Chem. B* **2010**, *114*, 9572–9577.

[150] Heintz, A. *J. Chem. Thermodyn.* **2005**, *37*, 525–535.

[151] Roth, C.; Peppel, T.; Fumino, K.; Köckerling, M.; Ludwig, R. *Angew. Chem. Int. Ed. Engl.* **2010**, *49*, 10221–4.

[152] Rey, R.; Hynes, J. T. *J. Chem. Phys.* **1998**, *108*, 142–153.

[153] Møller, K. B.; Rey, R.; Hynes, J. T. *J. Phys. Chem. A* **2004**, *108*, 1275–1289.

[154] Eaves, J. D.; Tokmakoff, A.; Geissler, P. L. *J. Phys. Chem. A* **2005**, *109*, 9424–9436.

[155] Lee, H.; Choi, J.-H.; Cho, M. *Phys. Chem. Chem. Phys.* **2010**, *12*, 12658–12669.

[156] Choi, J.-H.; Oh, K.-I.; Lee, H.; Lee, C.; Cho, M. *J. Chem. Phys.* **2008**, *128*, 134506.

[157] Zhang, S.; Zhang, Y.; Ma, X.; Lu, L.; He, Y.; Deng, Y. *J. Phys. Chem. B* **2013**, *117*, 2764–2772.

[158] Fumino, K.; Wulf, A.; Ludwig, R. *Angew. Chem. Int. Ed. Engl.* **2008**, *47*, 3830–3834.

[159] Fumino, K.; Reimann, S.; Ludwig, R. *Phys. Chem. Chem. Phys.* **2014**, *16*, 21903–29.

[160] Lenchenkov, V.; She, C. X.; Lian, T. Q. *J. Phys. Chem. B* **2006**, *110*, 19990–19997.

[161] Seddon, K. R.; Stark, A.; Torres, M.-J. *Pure Appl. Chem.* **2000**, *72*, 2275–2287.

[162] Canongia Lopes, J. N.; Costa Gomes, M. F.; Husson, P.; Padua, A. A. H.; Rebelo, L. P. N.; Sarraute, S.; Tariq, M. *J. Phys. Chem. B* **2011**, *115*, 6088–6099.

[163] Yaghini, N.; Nordstierna, L.; Martinelli, A. *Phys. Chem. Chem. Phys.* **2014**, *16*, 9266–75.

[164] Chatel, G.; Pereira, J. F. B.; Debbeti, V.; Wang, H.; Rogers, R. D. *Green Chem.* **2014**, 2051–2083.

[165] Sieffert, N.; Wipff, G. *J. Phys. Chem. B* **2007**, *111*, 7253–66.

[166] Hamm, P. *J. Chem. Phys.* **2006**, *124*, 124506.

[167] Khalil, M.; Demirdöven, N.; Tokmakoff, A. *J. Phys. Chem. A* **2003**, *107*, 5258–5279.

[168] Kwak, K.; Park, S.; Finkelstein, I. J.; Fayer, M. D. *J. Chem. Phys.* **2007**, *127*, 124503.

[169] Kwak, K.; Rosenfeld, D. E.; Fayer, M. D. *J. Chem. Phys.* **2008**, *128*, 204505.

[170] Eaves, J. D.; Loparo, J. J.; Fecko, C. J.; Roberts, S. T.; Tokmakoff, A.; Geissler, P. L. *Proc. Natl. Acad. Sci. U. S. A.* **2005**, *102*, 13019–13022.

[171] Press, W. H.; Teukolsky, S. A.; Vetterlin, W. T.; Flannery, B. P. *Numerical Recipes in C*, 2nd ed.; Cambridge University Press: New York, 1992.

[172] Cammarata, L.; Kazarian, S. G.; Salter, P. a.; Welton, T. *Phys. Chem. Chem. Phys.* **2001**, *3*, 5192–5200.

[173] Wong, D. B.; Giammanco, C. H.; Fenn, E. E.; Fayer, M. D. *J. Phys. Chem. B* **2013**, *117*, 623–635.

[174] Terranova, Z. L.; Corcelli, S. A. *J. Phys. Chem. B* **2014**, *118*, 8264–8272.

[175] Skinner, J. L. *Theor. Chem. Acc.* **2010**, *128*, 147–155.

[176] Oxtoby, D. W. *Adv. Chem. Phys.* **1981**, *47*, 487–519.

[177] Oxtoby, D. W. *Annu. Rev. Phys. Chem.* **1981**, *32*, 77–101.

[178] Owrutsky, J. C.; Raftery, D.; Hochstrasser, R. M. *Annu. Rev. Phys. Chem.* **1994**, *45*, 519–55.

[179] Helbing, J.; Nienhaus, K.; Nienhaus, G. U.; Hamm, P. *J. Chem. Phys.* **2005**, *122*, 124505.

[180] Ji, M.; Odelius, M.; Gaffney, K. J. *Science* **2010**, *328*, 1003–5.

[181] Hardacre, C.; Holbrey, J. D.; Mullan, C. L.; Youngs, T. G. A.; Bowron, D. T. *J. Chem. Phys.* **2010**, *133*, 74510.

[182] Russina, O.; Triolo, A.; Gontriani, L.; Caminiti, R. *J. Phys. Chem. B* **2011**, *3*, 27–33.

[183] Canongia Lopes, J. N.; Costa Gomes, M. F.; Pádua, A. A. H. *J. Phys. Chem. B* **2006**, *110*, 16816–16818.

[184] Annapureddy, H. V. R.; Kashyap, H. K.; De Biase, P. M.; Margulis, C. J. *J. Phys. Chem. B* **2010**, *114*, 16838–16846.

[185] Jiang, W.; Wang, Y.; Voth, G. A. *J. Phys. Chem. B* **2007**, *111*, 4812–4818.

[186] Mandal, P. K.; Sarkar, M.; Samanta, A. *J. Phys. Chem. A* **2004**, *108*, 9048–9053.

[187] Paul, A.; Mandal, P. K.; Samanta, A. *J. Phys. Chem. B* **2005**, *109*, 9148–53.

[188] Garrett-Roe, S.; Hamm, P. *Acc. Chem. Res.* **2009**, *42*, 1412–1422.

[189] Borek, J. A.; Perakis, F.; Hamm, P. *Proc. Natl. Acad. Sci. U. S. A.* **2014**, *111*, 10462–7.

[190] Khurmi, C.; Berg, M. A. *J. Chem. Phys.* **2008**, *129*, 64504.

[191] Niazi, A. A.; Rabideau, B. D.; Ismail, A. E. *J. Phys. Chem. B* **2013**, *117*, 1378–88.

[192] Kohno, Y.; Ohno, H. *Phys. Chem. Chem. Phys.* **2012**, *14*, 5063–70.

[193] Goodrich, B. F.; de la Fuente, J. C.; Gurkan, B. E.; Lopez, Z. K.; Price, E. A.; Huang, Y.; Brennecke, J. F. *J. Phys. Chem. B* **2011**, *115*, 9140–9150.

[194] Romanos, G. E.; Zubeir, L. F.; Likodimos, V.; Falaras, P.; Kroon, M. C.; Iliev, B.; Adamova, G.; Schubert, T. J. S. *J. Phys. Chem. B* **2013**, *117*, 12234–12251.

[195] Kamiya, N.; Matsushita, Y.; Hanaki, M.; Nakashima, K.; Narita, M.; Goto, M.; Takahashi, H. *Biotechnol. Lett.* **2008**, *30*, 1037–40.

[196] Zhang, Y.; Du, H.; Qian, X.; Chen, E. Y.-X. *Energy & Fuels* **2010**, *24*, 2410–2417.

[197] Yoshizawa, M.; Xu, W.; Angell, C. A. *J. Am. Chem. Soc.* **2003**, *125*, 15411–9.

[198] Angell, C. A.; Byrne, N.; Belieres, J.-P. *Acc. Chem. Res.* **2007**, *40*, 1228–36.

[199] Kashyap, H. K.; Annapureddy, H. V. R.; Raineri, F. O.; Margulis, C. J. *J. Phys. Chem. B* **2011**, *115*, 13212–13221.

[200] Liu, H.; Maginn, E. *ChemPhysChem* **2012**, *13*, 1701–1707.

[201] Hallett, J. P.; Liotta, C. L.; Ranieri, G.; Welton, T. *J. Org. Chem.* **2009**, *74*, 1864–8.

[202] Bini, R.; Chiappe, C.; Pomelli, C. S.; Parisi, B. *J. Org. Chem.* **2009**, *74*, 8522–30.

[203] Lui, M. Y.; Crowhurst, L.; Hallett, J. P.; Hunt, P. a.; Niedermeyer, H.; Welton, T. *Chem. Sci.* **2011**, *2*, 1491–1496.

[204] Marcus, Y.; Hefter, G. *Chem. Rev.* **2006**, *106*, 4585–4621.

[205] Marcus, Y. *Chem. Rev.* **2009**, *109*, 1346–1370.

[206] Van Der Vegt, N. F. A.; Haldrup, K.; Roke, S.; Zheng, J.; Lund, M.; Bakker, H. J. *Chem. Rev.* **2016**, *116*, 7626–7641.

[207] Reichardt, C.; Welton, T. *Solvents and Solvent Effects in Organic Chemistry*; Wiley-VCH Verlag GmbH Co. KGaA: Weinheim, Germany, 2010.

[208] Buchner, R.; Samani, F.; May, P. M.; Sturm, P.; Hefter, G. *ChemPhysChem* **2003**, *4*, 373–378.

[209] Fuoss, R. M.; Kraus, C. A. *J. Am. Chem. Soc.* **1933**, *55*, 1019–1028.

[210] Fuoss, R. M.; Hsia, K. L. *Proc. Natl. Acad. Sci. U. S. A.* **1967**, *57*, 1550–1557.

[211] Fernandez-Prini, R.; Justice, J.-C. *Pure Appl. Chem.* **1984**, *56*, 541–547.

[212] Buchner, R.; Chen, T.; Hefter, G. *J. Phys. Chem. B* **2004**, *108*, 2365–2375.

[213] Hefter, G. *Pure Appl. Chem.* **2006**, *78*, 1571–1586.

[214] Bowron, D. T.; Diaz Moreno, S. *Coord. Chem. Rev.* **2014**, *277*, 2–14.

[215] Hogen-Esch, T. E.; Smid, J. *J. Am. Chem. Soc.* **1965**, *87*, 669–670.

[216] Hogen-Esch, T. E.; Smid, J. *J. Am. Chem. Soc.* **1966**, *88*, 318–324.

[217] Guha, C.; Chakraborty, J. M.; Karanjai, S.; Das, B. *J. Phys. Chem. B* **2003**, *107*, 12814–12819.

[218] Daly, F. P.; Brown, C. W.; Kester, D. R. *J. Phys. Chem.* **1972**, *76*, 3664–3668.

[219] Moskovits, M.; Michaelian, K. H. *J. Am. Chem. Soc.* **1980**, *102*, 2209–2215.

[220] Bjerrum, N. *Kgl. Danske Vidensk. Selsk. Math.-fys. Medd.* **1926**, *7*, 1.

[221] Buchner, R.; Capewell, S. G.; Hefter, G.; May, P. M. *J. Phys. Chem. B* **1999**, *103*, 1185–1192.

[222] Fulton, J. L.; Heald, S. M.; Badyal, Y. S.; Simonson, J. M. *J. Phys. Chem. A* **2003**, *107*, 4688–4696.

[223] Badyal, Y. S.; Barnes, A. C.; Cuello, G. J.; Simonson, J. M. *J. Phys. Chem. A* **2004**, *108*, 11819–11827.

[224] Díaz-Moreno, S.; Ramos, S.; Bowron, D. T. *J. Phys. Chem. A* **2011**, *115*, 6575–6581.

[225] Böhm, F.; Sharma, V.; Schwaab, G.; Havenith, M. *Phys. Chem. Chem. Phys.* **2015**, *17*, 19582–19591.

[226] Giammanco, C. H.; Kramer, P. L.; Yamada, S. A.; Nishida, J.; Tamimi, A.; Fayer, M. D. *J. Chem. Phys.* **2016**, *144*, 104506.

[227] Bian, H. T.; Wen, X. W.; Li, J. B.; Chen, H. L.; Han, S. Z.; Sun, X. Q.; Song, J. A.; Zhuang, W.; Zheng, J. R. *Proc. Natl. Acad. Sci. USA* **2011**, *108*, 4737–4742.

[228] Park, S.; Ji, M.; Gaffney, K. J. *J. Phys. Chem. B* **2010**, *114*, 6693–6702.

[229] Singh, T.; Kumar, A. *J. Phys. Chem. B* **2008**, *112*, 12968–12972.

[230] Kramer, P. L.; Nishida, J.; Giammanco, C. H.; Tamimi, A.; Fayer, M. D. *J. Chem. Phys.* **2015**, *142*, 184505.

[231] Kramer, P. L.; Nishida, J.; Fayer, M. D. *J. Chem. Phys.* **2015**, *143*, 124505.

[232] Balabai, N.; Waldeck, D. H. *J. Phys. Chem. B* **1997**, *101*, 2339–2347.

[233] Balabai, N.; Kurnikova, M. G.; Coalson, R. D.; Waldeck, D. H. *J. Am. Chem. Soc.* **1998**, *120*, 7944–7951.

[234] Welton, T. *Green Chem.* **2011**, *13*, 225.

[235] Eastoe, J.; Gold, S.; Rogers, S. E.; Paul, A.; Welton, T.; Heenan, R. K.; Grillo, I. *J. Am. Chem. Soc.* **2005**, *127*, 7302–7303.

[236] Falcone, R. D.; Correa, N. M.; Silber, J. J. *Langmuir* **2009**, *25*, 10426–9.

[237] Mondal, T.; Das, A. K.; Sasmal, D. K.; Bhattacharyya, K. *J. Phys. Chem. B* **2010**, *114*, 13136–42.

[238] Rai, R.; Pandey, S.; Baker, S. N.; Vora, S.; Behera, K.; Baker, G. A.; Pandey, S. *Chemistry* **2012**, *18*, 12213–12217.

[239] Sando, G. M.; Dahl, K.; Owrutsky, J. C. *Chem. Phys. Lett.* **2006**, *418*, 402–407.

[240] Ferreyra, D. D.; Correa, N. M.; Silber, J. J.; Falcone, R. D. *Phys. Chem. Chem. Phys.* **2012**, *14*, 3460–70.

[241] Andújar-Matalobos, M.; García-Río, L.; López-García, S.; Rodríguez-Dafonte, P. *J. Colloid Interface Sci.* **2011**, *363*, 261–267.

[242] Shi, W.; Hong, L.; Damodaran, K.; Nulwala, H. B.; Luebke, D. R. *J. Phys. Chem. B* **2014**, *114*, 13870–13881.

[243] Correa, N. M.; Silber, J. J.; Riter, R. E.; Levinger, N. E. *Chem. Rev.* **2012**, *112*, 4569–4602.

[244] Pramanik, R.; Sarkar, S.; Ghatak, C.; Rao, V. G.; Setua, P.; Sarkar, N. *J. Phys. Chem. B* **2010**, *114*, 7579–7586.

[245] Sarkar, S.; Pramanik, R.; Ghatak, C.; Rao, V. G.; Sarkar, N. *J. Chem. Phys.* **2011**, *134*, 074507.

[246] Lepori, C. M. O.; Correa, N. M.; Silber, J. J.; Falcone, R. D. *Soft Matter* **2016**, *12*, 830–844.

[247] Falcone, R. D.; Baruah, B.; Gaidamauskas, E.; Rithner, C. D.; Correa, N. M.; Silber, J. J.; Crans, D. C.; Levinger, N. E. *Chem. - A Eur. J.* **2011**, *17*, 6837–6846.

[248] Brinzer, T.; Berquist, E. J.; Ren, Z.; Dutta, S.; Johnson, C. A.; Krisher, C. S.; Lambrecht, D. S.; Garrett-Roe, S. *J. Chem. Phys.* **2015**, *142*, 212425.

[249] Dutta, S.; Ren, Z.; Brinzer, T.; Garrett-Roe, S. *Phys. Chem. Chem. Phys.* **2015**, *17*, 26575–26579.

[250] van der Loop, T. H.; Panman, M. R.; Lotze, S.; Zhang, J.; Vad, T.; Bakker, H. J.; Sager, W. F. C.; Woutersen, S. *J. Chem. Phys.* **2012**, *137*, 044503.

[251] Ren, Z.; Brinzer, T.; Dutta, S.; Garrett-Roe, S. *J. Phys. Chem. B* **2015**, *119*, 4699–4712.

[252] Rivera, C. A.; Souna, A. J.; Bender, J. S.; Manfred, K.; Fourkas, J. T. *J. Phys. Chem. B* **2013**, *117*, 15875–15885.

[253] Moilanen, D. E.; Fenn, E. E.; Wong, D.; Fayer, M. D. *J. Chem. Phys.* **2009**, *131*, 1–9.

[254] Bian, H.; Chen, H.; Zhang, Q.; Li, J.; Wen, X.; Zhuang, W.; Zheng, J. *J. Phys. Chem. B* **2013**, *117*, 7972–7984.

[255] Tamimi, A.; Fayer, M. D. *J. Phys. Chem. B* **2016**, *120*, 5842–5854.

[256] Hamm, P.; Lim, M.; Hochstrasser, R. M. *J. Phys. Chem. B* **1998**, *102*, 6123–6138.

[257] Zanni, M. T.; Hochstrasser, R. M. *Curr. Opin. Struct. Biol.* **2001**, *11*, 516–522.

[258] Rey, R.; Møller, K. B.; Hynes, J. T. *J. Phys. Chem. A* **2002**, *106*, 11993–11996.

[259] Mukamel, S. *Principles of Nonlinear Optical Spectroscopy*; Oxford University Press: New York, 1995.

[260] Cho, M.; Fleming, G. R.; Mukamel, S. *J. Chem. Phys.* **1993**, *98*, 5314–5326.

[261] Tokmakoff, A.; Fayer, M. D. *J. Chem. Phys.* **1995**, *103*, 2810–2826.

[262] Tokmakoff, A. *J. Chem. Phys.* **1996**, *105*, 1–12.

[263] Tokmakoff, A. *J. Chem. Phys.* **1996**, *105*, 13–21.

[264] Giammanco, C. H.; Yamada, S. A.; Kramer, P. L.; Tamimi, A.; Fayer, M. D. *J. Phys. Chem. B* **2016**, *120*, 6698–6711.

[265] Shin, J. Y.; Yamada, S. A.; Fayer, M. D. *J. Am. Chem. Soc.* **2017**, *139*, 311–323.

[266] Ren, Z.; Kelly, J.; Gunathilaka, C. P.; Brinzer, T.; Dutta, S.; Johnson, C. A.; Mitra, S.; Garrett-Roe, S. *Phys. Chem. Chem. Phys.* **2017**, *19*, 32526–32535.

[267] Bublitz, G. U.; Boxer, S. G. *Annu. Rev. Phys. Chem.* **1997**, *48*, 213–242.

[268] Faraudo, J. *J. Chem. Phys.* **2002**, *116*, 5831–5841.

[269] Ghosh, A.; Samuel, J.; Sinha, S. *Europhys. Lett.* **2012**, *98*, 30003.

[270] Choi, J.-H.; Oh, K.-I.; Lee, H.; Lee, C.; Cho, M. *J. Chem. Phys.* **2008**, *128*, 134506.

[271] Lindquist, B. A.; Corcelli, S. A. *J. Phys. Chem. B* **2008**, *112*, 6301–6303.

[272] Yamada, S. A.; Thompson, W. H.; Fayer, M. D. *J. Chem. Phys.* **2017**, *146*, 234501.

[273] Wang, C. C.; Pecora, R. *J. Chem. Phys.* **1980**, *72*, 5333.

[274] Lipari, G.; Szabo, A. *Biophys. J.* **1980**, *30*, 489–506.